The Dynamic Modelling of a Laboratory-Scale Packed Distillation Column, Used to Separate Mixtures of Tetrafluoroethylene, Hexafluoropropylene and Octafluorocyclobutane at Sub-Zero Temperatures

Johannes Ignatius Espach

The Dynamic Modelling of a Laboratory-Scale Packed Distillation Column, Used to Separate Mixtures of Tetrafluoroethylene, Hexafluoropropylene and Octafluorocyclobutane at Sub-Zero Temperatures

by

Johannes Ignatius Espach

Supervised by

Mr PW Sonnendecker

Co-supervised by

Prof PL Crouse

A dissertation in partial fulfillment
of the requirements for the degree

Master of Engineering (Chemical Engineering)

in the

Department of Chemical Engineering
Faculty of Engineering, the Built Environment and Information Technology

University of Pretoria
Pretoria

December 2019

Synopsis

Dynamic simulation programs were created in the Python programming language, to describe a laboratory scale, sub-zero distillation column, that is used to separate mixtures of tetrafluoroethylene (TFE), hexafluoropropylene (HFP) and octafluorocyclobutane (OFCB). Both the equilibrium and rate-based modelling approaches were taken, to generate a comparison between the efficiency and simulation time of both models.

A physical properties data bank for the three components had to be created, as the main and many of the sub-models require physical or thermodynamic properties for evaluation. The different physical property models, found in literature, were programmed into functions that could easily return the wanted property, given a set of required inputs. The applicable mixing rules for each property type was also programmed into functions, to allow for easy retrieval.

The vapour-liquid equilibrium (VLE) model used, is also one that comes from literature and is based on parameters for the three binary systems. The VLE model consists of the Peng-Robinson equation of state, that utilises the Mathias-Copeman alpha function and the Wong-Sandler mixing rules, to describe the vapour phase. The liquid phase is described by the non-random two liquid (NRTL) activity coefficient model. Furthermore, the γ-Φ VLE formulation was used to put the thermodynamic model together. These models were also written into functions to serve as simulation building blocks.

Mass and energy transfer on packed sections in the rate-based model was described by the Maxwell-Stefan diffusion model. The form of this model that was utilised, is the matrix-based, exact solution of the Maxwell-Stefan equations, under the two-film theory. This model was slightly simplified by assuming that the corrective flux matrix reduces to the identity matrix– an assumption that is regularly made in distillation modelling.

Emphasis was laid in documenting how the models are put together to build the simulations. Dynamic simulation algorithms rarely accompany distillation models reported in literature, or authors make use of commercial software to order the modelling equations for them. One of the objectives of the research presented here was, therefore, to report on the process developed to solve the problem.

Both simulation programs delivered typical responses that can be expected of distillation

systems. The actual change in the magnitude of the values, however, proved to be significantly small. The cause of this, being the large liquid molar hold-up values that were produced by the model initialisation. The feed flow rate, in comparison, is too small to bring about a significant effect when suddenly increased. This could mean that the system is not capable of reaching the steady-state produced by the initialisation (as the feed cylinder may be too small to contain the required amount of feed gas) and that the column may have to be run in a continuous dynamic state. To be sure of this, however, the model will first need to be validated against experimental data. Furthermore, the simulation programs proved to progress very slowly, particularly the simulation built around the rate-based model. A time step-size of 0.5 resulted in an integration time around 1 minute and 20 seconds for the equilibrium model, while the rate model ran for over 19 minutes, both for a timespan of 300 s.

It is recommended that future research focuses on building start-up simulations for the models, to provide better initial results and to give more insight into the operation of the column. Experimental validation of the models is also important, to establish their accuracies. Finally, work has to be done to improve the simulation speeds, especially if it is required that one of the models are integrated into the column's control system.

Acknowledgements

The author would like to express his gratitude and appreciation to:

My Heavenly Father, for gifting me with the ability to complete my studies and providing me with strength when I need it most. All glory to Your Name!

My parents, grandmother and my brothers, for their unwavering love and support and for keeping me in their prayers.

My supervisor, Paul Sonnendecker, for his technical guidance and advice throughout this project and his patient willingness to teach me new things.

My co-supervisor, Prof PL Crouse, for granting me this opportunity and administering financial support.

The Fluorochemical Expansion Initiative, driven by the Department of Science and Technology and the Department of Trade and Industry, for providing financial support.

My friends, Anya, Brenda, Deon and Daniel, for the countless coffee and tea breaks, their support and the occasional office shenanigans.

Contents

List of Figures

List of Tables

Nomenclature

A	Area	m^2
A	Helmholtz free energy	$J{\cdot}kmol^{-1}$
a	Attraction parameter	$J{\cdot}kmol^{-1}$
a	Interfacial area	m^2
a_e	Effective interfacial area of packing	$m^2{\cdot}m^{-3}$
a_p	Total interfacial area of packing	$m^2{\cdot}m^{-3}$
B	Bottoms molar flow rate	$kmol{\cdot}s^{-1}$
b	Van der Waals covolume	$m^3{\cdot}kmol^{-1}$
C_P	Heat capacity	$J{\cdot}kmol^{-1}K^{-1}$
C_p	Capacity parameter	
C_V	Control valve coefficient	
D	Diffusion coefficient	$m^2{\cdot}s^{-1}$
D	Distillate molar flow rate	$kmol{\cdot}s^{-1}$
D, d	Diameter	m
e	Point energy flux	$W{\cdot}m^{-2}$
F	Mixed feed molar flow rate	$kmol{\cdot}s^{-1}$
F	Packing parameter	ft^{-1}
f	Component feed molar flow rate	$kmol{\cdot}s^{-1}$
f'	Friction factor	
G	Gas (vapour) mass flux	$kg{\cdot}m^{-2}s^{-1}$

G	Gibbs free energy	$\mathrm{J{\cdot}kmol^{-1}}$
G	NRTL model coefficient	
g	Gravitational acceleration	$\mathrm{m{\cdot}s^{-2}}$
H	Vapour enthalpy	$\mathrm{J{\cdot}kmol^{-1}}$
h	Heat transfer coefficient	$\mathrm{W{\cdot}m^{-2}K^{-1}}$
h	Height	m
h	Liquid enthalpy	$\mathrm{J{\cdot}kmol^{-1}}$
h	Volumetric hold-up	$\mathrm{m^3{\cdot}m^{-3}}$ of packing
J	Diffusive flux	$\mathrm{kmol{\cdot}s^{-1}}$
K	Equilibrium constant	
k	Mass transfer coefficient	$\mathrm{kmol{\cdot}m^{-2}s^{-1}}$
k	Thermal conductivity	$\mathrm{W{\cdot}m^{-1}K^{-1}}$
L	Length	
L	Liquid mass flux	$\mathrm{kg{\cdot}m^{-2}s^{-1}}$
l	Component liquid molar flow rate	$\mathrm{kmol{\cdot}s^{-1}}$
$L/\overline{L}$	Mixed liquid molar flow rate above/below the feed plate	$\mathrm{kmol{\cdot}s^{-1}}$
l_B	Baffle	m
Le	Lewis number	
M	Molar holdup	kmol
M	Molar mass	$\mathrm{kg{\cdot}kmol^{-1}}$
N	Point molar flux	$\mathrm{kmol{\cdot}m^{-2}s^{-1}}$
Nu	Nusselt number	
P	Pressure	kPa
p	Partial pressure	kPa
p_t	Tube pitch	m

Pr	Prandtl number	
Q	Heat duty	W
q	Conductive heat flux	$W{\cdot}m^{-2}$
q	Stage heat loss/gain to/from the environment	W
R	Universal gas constant	$kJ{\cdot}kmol^{-1}K^{-1}$
r	Side stream to interstage flow ratio	
Re	Reynolds number	
S	Side stream molar flow	$kmol{\cdot}s^{-1}$
T	Temperature	K
t	Time	s
U	Overall heat transfer coefficient	$W{\cdot}m^{-2}K^{-1}$
u	Linear velocity	$m{\cdot}s^{-1}$
v	Component vapour molar flow rate	$kmol{\cdot}s^{-1}$
V, v	Molar volume	$m^3{\cdot}kmol^{-1}$
$V/\overline{V}$	Mixed vapour molar flow rate above/below the feed plate	$kmol{\cdot}s^{-1}$
$x(\overline{x})$	Liquid mole fraction (of the bulk liquid)	
$y(\overline{y})$	Vapour mole fraction (of the bulk vapour)	
Z	Packed section height	m
z	Feed mole fraction	
Z, z	Compressibility factor	

Greek

α	Equation of state parameter	
Δ	Macro change in parameter	
δ	Kronecker delta	
δ	Micro change in parameter	

ϵ	Conductive heat flux correction factor	
Γ	Element of the thermodynamic liquid correction factor matrix	
γ	Activity coefficient	
Γ_v	Verticle tube loading	$kg{\cdot}m^{-1}s^{-1}$
λ	Heat of vapourisation	$J{\cdot}kmol^{-1}$
μ	Dynamic viscosity	$Pa{\cdot}s$
ν	Kinematic viscosity (usually by subtraction)	$m^2{\cdot}s^{-1}$
ω	Acentric factor	
Φ, ϕ	Fugacity coefficients	
ρ	Density	$kg{\cdot}m^{-3}$
σ	Surface tension	$N{\cdot}m^{-1}$
τ	NRTL binary interaction parameter	

Superscripts

$*$	Saturated property
E	Excess property
I	Property at vapour-liquid interface
L	Liquid state
V	Vapour state

Subscripts

∞	Infinite property
B	Origin at bulk phase
B	Property of the bottoms stream
c	Critical property
c	Number of components
cond	Denotes the condenser

CV	Denotes *Control Valve*
D	Property of the distillate stream
d	Denotes *dry*
e	Denotes *equivalent*
EL	Denotes *Elevation*
EP	Denotes *End-point Pressures*
f	Denotes *frictional*
I	Origin at interface
i	Denotes an inner dimension
i, j	Component numbers
KE	Denotes *Kinetic Energy*
L	Liquid property
lm	Denotes a log-mean
m	Mixture property
N	Conservation balance envelope position number
n	Plate number
nb	Denotes *nucleate boiling*
o	Denotes an outer dimension
p	Denotes *particle*
r	Reduced property
reb	Denotes the reboiler
$refl$	Denotes the reflux line
t	Denotes a total value
V	Vapour property
w	Denotes a property at a system wall

Matrix Symbols

$\boldsymbol{\Gamma}$	Thermodynamic liquid correction factor square matrix	
$\boldsymbol{\mathcal{N}}$	Interphase mass transfer rate square matrix	$\mathrm{kmol{\cdot}s^{-1}}$
$\overline{\boldsymbol{x}}$	Bulk liquid phase mole fraction column matrix	
$\overline{\boldsymbol{y}}$	Bulk vapour phase mole fraction column matrix	
$\boldsymbol{\Phi}$	(Square) matrix of rate factors	
$\boldsymbol{\Theta}$	Augmented (square) matrix of rate factors	
$\boldsymbol{\Xi}$	Flux correction factor square matrix	
$\boldsymbol{B}$	Inverse mass transfer coefficient square matrix	$\mathrm{m^2s{\cdot}kmol^{-1}}$
$\boldsymbol{I}$	Identity matrix	
$\boldsymbol{J}$	Diffusive flux column matrix	$\mathrm{kmol{\cdot}s^{-1}}$
$\boldsymbol{k}$	Mass transfer coefficient square matrix	$\mathrm{kmol{\cdot}m^{-2}s^{-1}}$
$\left(\overline{\boldsymbol{y}} - \boldsymbol{y^I}\right)$	Vapour phase mole fraction driving force column matrix	
$\left(\boldsymbol{x^I} - \overline{\boldsymbol{x}}\right)$	Liquid phase mole fraction driving force column matrix	

Other Symbols

$\mathcal{E}$	Interphase energy transfer rate	W
$\mathcal{N}$	Interphase mass transfer rate	$\mathrm{kmol{\cdot}s^{-1}}$

Introduction

The Fluoro-polymer Laboratory at the University of Pretoria (UP) is engaged in an ongoing project that aims to develop a continuous, automated, small-scale pilot laboratory that converts a feedstock of waste polytetrafluoroethylene (PTFE) into virgin PTFE, through vacuum pyrolysis and polymerisation of TFE gas. To do this, the laboratory is divided into three main, interconnected sections that are distinguished by pressure, namely: the low, medium and high-pressure sections. The low-pressure section houses a continuously fed pyrolysis reactor, where PTFE is depolymerised to mainly produce tetrafluoroethylene (TFE), hexafluoropropylene (HFP) and octafluorocyclobutane (OFCB). The medium pressure section revolves around a packed distillation column that separates the TFE-HFP-OFCB ternary mixture at sub-zero temperatures. Finally, the high-pressure section consists of a polymerisation reactor, where TFE is re-polymerised to produce PTFE.

The motivation for this project lies in the fact that PTFE cannot be recycled using the conventional techniques that have been developed for other polymers, due to PTFE's unique properties. These properties include extremely high molten viscosities, high chemical inertness and high resistance to dissolution by virtually all solvents. Consequently, waste PTFE is either landfilled, incinerated or mechanically recycled.

These waste treatment processes are, however, suboptimal. PTFE's chemical inertness will prevent it from degrading in a landfill and it will, therefore, accumulate for an undetermined amount of time, since no data is available on the natural degradation of PTFE. The result is also undesired from an economic point of view, as a large amount of waste is produced from subtractive manufacturing processes such as turning or milling (conventional polymer processing techniques can, again, not be used to process PTFE). Incineration is also undesirable, as it may result in the production of dangerous fluorinated gases, such as hydrogen fluoride (HF) and iso-, 1- and 2-octafluorobutylene. Furthermore, mechanical recycling produces only low-quality products.

Several successful projects on the PTFE chemical recycling subject have already been delivered by postgraduate students at UP's Department of Chemical Engineering, most

notably:

Conradie (2011) produced vapour-liquid equilibrium data for the TFE-OFCB, TFE-HFP and HFP-OFCB binary systems.

Sonnendecker (2015) developed an in-line Fourier-transform infrared (FTIR) spectroscopy sampling system, to facilitate rapid sampling during processing.

Bezuidenhoudt (2016) designed and implemented a hopper-screw feeder system to upgrade the pyrolysis reactor from batch to continuous, to study the continuous depolymerisation reaction kinetics.

The objective of the current project is to derive a dynamic mathematical model and create a simulation program that describes the packed distillation column used in the laboratory, to separate the TFE-HFP-OFCB ternary mixture. This model aims to function as a tool that can give insight to the internal workings of the column, as effective separations have been difficult to achieve in the past. The main cause of this is the nature of the feed to the column: the feed is stored at ambient room temperatures (on average 23 °C) and fed to the column, with its lowest temperature (at the condenser) at around -75 °C, which causes the internal temperatures to drift away from the desired profiles. Condensing the feed is not possible, as TFE's dew point temperature is lower than OFCB's freezing temperature. Neither can the system's pressure be increased to affect a TFE dew point temperature that is higher than OFCB's freezing temperature, as TFE may undergo an autopolymerisation reaction at increased pressures.

The scope of this project, therefore, is to find a column configuration that will produce the required separations, at operating pressures not much higher than 100 kPa (200 kPa is the upper limit). Also included in the scope is the aforementioned dynamic model and simulation program. Focus will also be given to how the model is put together to build the simulation program, as algorithms rarely accompany these types of models in literature. This project is limited to developing the model and simulation program, and will not include experimental validation, due to time constraints.

Literature Review

2.1 Depolymerisation of PTFE

2.1.1 Depolymerisation Technology

A number of different PTFE depolymerisation reactor set-ups can be found in the literature, ranging from simple batch systems (Lewis & Naylor (1947); Wall & Michaelson (1956); Florin, Parker & Wall (1966); Bhadury *et al* (2006)), to intricate continuous systems (Simon & Kaminsky (1998); Meissner, Wróblewska & Milchert (2004); Van der Walt & Bruinsma (2006); Bezuidenhoudt, Sonnendecker & Crouse (2017)). Furthermore, the reactor systems can be distinguished by their process atmospheres and heating sources. Since PTFE pyrolysis is not the focus of this project, the following section will focus on the specific continuous depolymerisation system found in the laboratory, to provide a background for this project.

The depolymerisation process in the laboratory starts with the hopper that is loaded with about 1 kg of waste PTFE powder (shown in Figure 1). The hopper is sealed with a Viton gasket and closed up with a polycarbonate top. Fixed to the polycarbonate top is a motor that drives a stirrer inside the hopper. The stirrer is designed to prevent PTFE from clumping together and sticking to the sides of the hopper. A process flow diagram of the depolymerisation system in the laboratory is presented in Figure 2.

From the hopper, the PTFE flows down into a screw conveyor that feeds the reactor. The screw is driven by a motor (a magnetic coupling is used to ensure a sealed system), that is controlled by a variable frequency drive (VFD). The hopper and screw conveyor are separated from the reactor by a pneumatically actuated ball valve.

The pyrolysis reactor is constructed from a steel pipe and is connected to the ball valve via a flange that is sealed with a Viton gasket. Heat is supplied to the reactor by an electrically heated furnace. Temperature control and monitoring is aided with thermocouples

Figure 1: Annotated photograph of the pyrolysis reactor set-up

located in the furnace, near the bottom of the reactor and 150 mm from the bottom of the reactor.

The reactor outlet is fitted with a pressure transmitter that also displays the reactor's pressure on a digital readout. The pressure transmitter provides the feedback required to control the reactor's pressure, using a motor actuated control valve.

Sampling valves to the right of the reactor are used to sample the product gas for compositional analysis by means of FTIR spectroscopy. The first valve is quickly opened and closed to fill a section of tubing, which is initially under vacuum, with a gas sample. The second valve is then opened to send the sample to the FTIR, after which the sampling volume and FTIR is evacuated in preparation of the next sample.

The pyrolysis products flow through a distribution manifold (Figure 3) before entering a condenser. Cooling is achieved by immersing the condenser in a dewar containing liquid nitrogen. This process is automated by a pneumatically actuated lift.

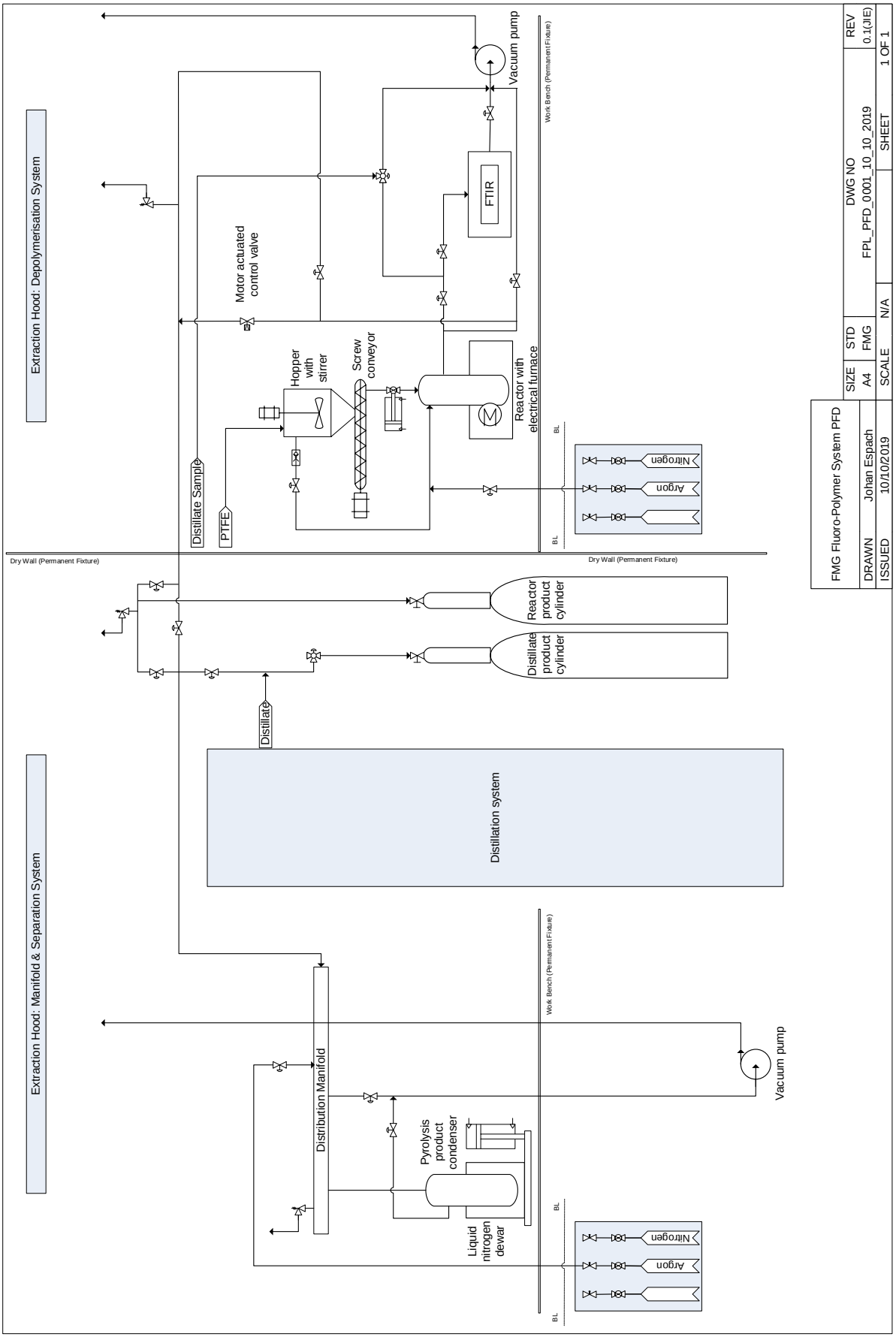

Figure 2: Pyrolysis system process flow diagram

Figure 3: Annotated photograph of the pyrolysis gas condenser system

2.1.2 Pyrolysis Products

The pyrolysis of PTFE can produce a variety of species, depending on the reactor's temperature, pressure and atmosphere. Lewis & Naylor (1947) showed that three main products can be expected during PTFE decomposition, especially under reduced pressures and in the temperature range 600 °C – 700 °C: tetrafluoroethylene (TFE), hexafluoropropylene (HFP) and octafluorocyclobutane (OFCB) (the chemical structures for these compounds are presented in Figure 4). Similar results have subsequently been observed by Simon & Kaminsky (1998) under a steam atmosphere, Meissner *et al* (2004) and Bhadury *et al* (2006) under nitrogen atmospheres and Van der Walt & Bruinsma (2006) and Bezuidenhoudt *et al* (2017), who also studied PTFE depolymerisation under reduced pressures.

Furthermore, an increase in temperature leads to the formation of additional products. Meissner *et al* (2004) reported the formation of 1-, 2- and iso-octafluorobutylenes (1-, 2- and i-OFB) in the 750 °C – 780 °C temperature range. The formation of these products are ill-favoured, as they are highly toxic. A further temperature increase to 800 °C – 900 °C, results in the production of hexafluoroethane (Van der Walt & Bruinsma, 2006).

Finally, Meissner *et al* (2004) and Bezuidenhoudt *et al* (2017) noticed the formation of PTFE dust, downstream of the reactors in their respective systems, which was formed by the autopolymerisation of TFE. Meissner *et al* (2004) attributed this formation to system temperatures below 600 °C and a TFE concentration above 50 mol%.

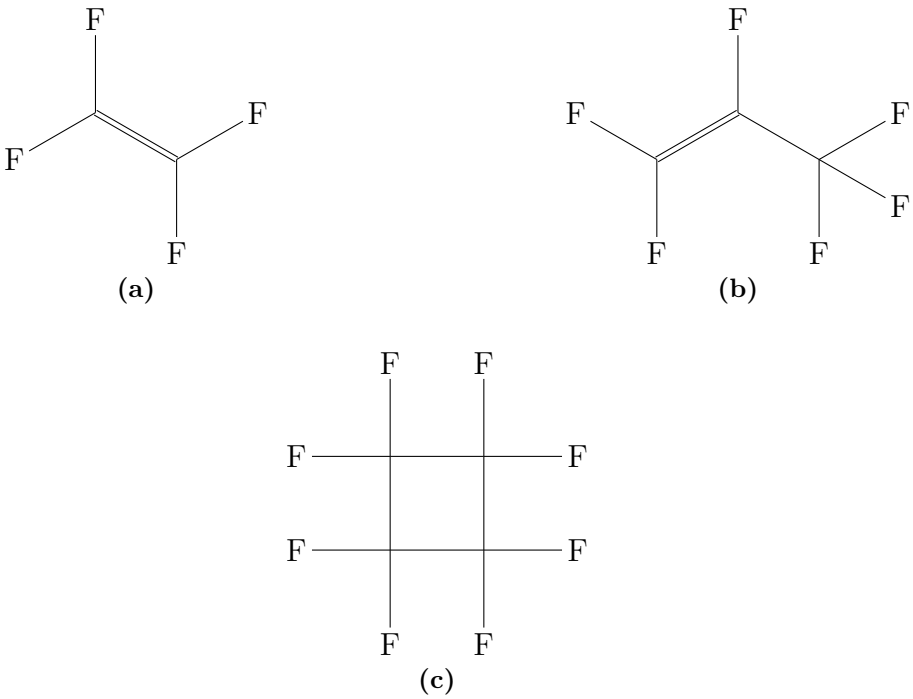

Figure 4: Chemical structures for (a) TFE, (b) HFP and (c) OFCB

2.1.3 Decomposition Mechanism

When Lewis & Naylor (1947) first studied the depolymerisation of PTFE, they proposed a mechanism that starts with the splitting off of TFE-units. Under conditions of increased pressure, these units undergo secondary reactions to form higher molecular mass compounds, such as HFP and OFCB. Their theory has since been refined to produce a mechanism similar to what can be expected during a polymerisation reaction. The reaction starts with the initiation by random chain scission, as shown in Equation 1 (Van der Walt & Bruinsma (2006); Bezuidenhoudt *et al* (2017))

$$—(CF_2—CF_2)_n— \longrightarrow R_a—CF_2 \cdot + \cdot CF_2—R_b \tag{1}$$

Where R denotes the residual polymer chain. Primary product formation starts with difluorocarbene formation (Equation 2)

$$R_a—CF_2\cdot \longrightarrow \cdot\cdot CF_2 + \cdot CF_2—R_b \tag{2}$$

which leads to TFE formation (Equation 3)

$$2 \cdot\cdot CF_2 \longrightarrow CF_2 = CF_2 \tag{3}$$

Secondary reactions lead to OFCB (Equation 4) and HFP (Equation 5) formation

$$2CF_2 = CF_2 \longrightarrow C_4F_8 \tag{4}$$

$$CF_2 = CF_2 + \cdot\cdot CF_2 \longrightarrow CF_3—CF = CF_2 \tag{5}$$

A tertiary reaction step also leads to HFP formation (Equation 6), together with either 1-OFB or i-OFB formation (Equation 7)

$$C_4F_8 \longrightarrow CF_3—CF = CF_2 + \cdot\cdot CF_2 \tag{6}$$

$$\begin{aligned} CF_3—CF = CF_2 + \cdot\cdot CF_2 &\longrightarrow CF_3CF_2CF = CF2 \\ or &\longrightarrow (CF_3)_2C—CF_2 \end{aligned} \tag{7}$$

Finally, the reaction mechanism exhibits a recombination step, which forms PTFE oligomeric waxes

$$R_a—CF_2 \cdot + \cdot CF_2—R_b \longrightarrow R_a—CF_2—CF_2—R_b \tag{8}$$

2.1.4 Temperature and Pressure Effects

Meissner *et al* (2004), Van der Walt & Bruinsma (2006) and Bezuidenhoudt *et al* (2017), all produced contour plots that depict the effects of temperature and pressure on product formation for their respective systems. The work done by Bezuidenhoudt *et al* (2017) is of particular importance, as this research was performed in the Fluoro-polymer laboratory and characterises the product distributions that can possibly be produced in the pyrolysis reactor (which serves as feed to the distillation column).

This characterisation employs response surface methodology to quantify the effect of temperature and pressure on the product distributions of TFE, HFP and OFCB. Their response function for component i, was defined as

$$Y_i = \beta_0 + \beta_1 X_1 + \beta_2 X_2 + \beta_3 X_1^2 + \beta_4 X_2^2 \tag{9}$$

where X_i is a coded factor value for either temperature or pressure. In this instance, an i-value of 1 denotes temperature, while an i-value of 2 denotes pressure

$$X_i = \frac{(x_i - a)}{b} \tag{10}$$

with the constants a and b calculated by

$$a = \frac{x_H + x_L}{2} \tag{11}$$

and

$$b = \frac{x_H - x_L}{2} \tag{12}$$

The subscripts H and L in Equations 11 and 12 refer to the higher and lower values in the temperature and pressure ranges studied. Their temperatures ranged from 650 °C to 750 °C, while their pressures ranged from < 10 kPa to 40 kPa. The coefficient values fitted to Equation 9 are presented in Table 1, while the resulting contour plots are illustrated in Figure 5.

Table 1: Coefficient values for Equation 9 for TFE, HFP and OFCB (Bezuidenhoudt, Sonnendecker & Crouse, 2017)

	Coefficients				
Component	β_0	β_1	β_2	β_3	β_4
TFE	0.5927	-0.0642	-0.333	-0.0823	0.1028
HFP	0.1121	0.0314	0.0675	0.0344	-0.0314
OFCB	0.2853	0.0259	0.2544	0.0508	-0.0601

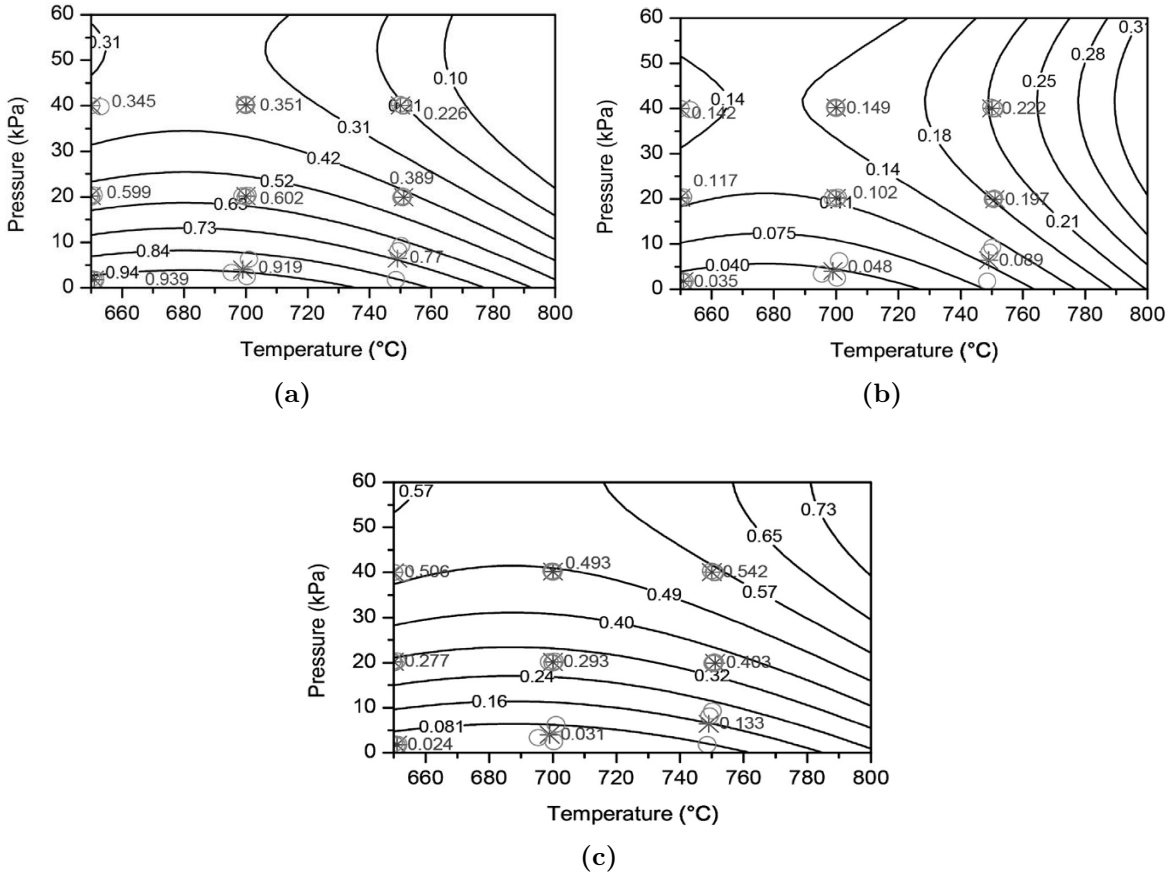

Figure 5: Contour plots describing the effect of temperature and pressure on the fractional distribution of (a) TFE, (b) HFP and (c) OFCB in the pyrolysis reactor product stream (Bezuidenhoudt, Sonnendecker & Crouse, 2017)

During the analysis of their contour plots for TFE, Bezuidenhoudt *et al* (2017) found that TFE is optimally produced at the lower ends of the temperature and pressure ranges (around 675 °C and < 10 kPa), where TFE mole fractions around 95 % were produced. Increases in both temperature and pressure lead to a decrease in TFE concentrations, with changes in pressure having a greater effect on TFE's production.

The decline in TFE's concentration with increased temperature and pressure is coupled with an increase in OFCB's concentration, with pressure, once again, being the dominant factor for OFCB's increase. It was observed that operating the reactor at a temperature and pressure of 750 °C and 40 kPa, will produce a maximum OFCB concentration of 55 %.

The statistical analysis of HFP-production yielded interesting results. From the HFP contour map, the authors marked that HFP production has a higher sensitivity to changes in pressure. This changes, however, around an operating pressure of about 30 kPa, where the sensitivity shifts to changes in temperature. The optimal operating conditions for HFP production were determined to be at a temperature and pressure of 750 °C and 40 kPa, which yielded an HFP molar concentration of 25 %.

2.2 Separating Mixtures of TFE, HFP and OFCB

Separating the product mixture is the next step in PTFE's chemical recycling route. This step is important as it fulfills the demand for pure TFE required to produce high-quality PTFE. The literature describes that previous separation activities for mixtures of TFE, HFP and OFCB were achieved by batch distillation, such as the Podbielniak distillation column used by Lewis & Naylor (1947) and the batch packed distillation column designed by Conradie (2011).

Recycling PTFE waste on a larger scale will, however, require continuous distillation columns to keep up with the upstream production rates. Creating a fundamental understanding of the total system with the help of modelling equations, can lead to a valuable tool that will not only aid in the design of continuous columns, but also in controlling these systems during operation.

2.2.1 Packed Column Modelling Approaches

The literature describes two methods that can be employed to model mass transfer in packed columns: one where the mass and energy balances are written as differential

equations and solved by integrating over the height of the packed section, while the other method divides the packed section into smaller subsections and treats each subsection analogous to a tray in a staged column (Krishnamurthy & Taylor, 1985b). The second method will be used in the present work as it will simplify the computational load imposed by integrating over the height of the packed section, especially when the model is extended to use in a dynamic simulation that introduces an additional integration dimension over time. Using the second method will also make it easier to adapt the model, should it be required to be used as a design tool to build a new column for an up-scaled version of the process being developed. Accuracy of the model will be maintained by choosing an adequate number of sub-sections to divide the actual packed section into. Of course, this may turn into a balancing act, as increasing the number of subsections increases the required computation time (Taylor & Krishna, 1993: 398-399).

2.2.2 Equilibrium Based steady-state Modelling

Equilibrium-based distillation column models are built on the assumption that the vapour and liquid compositions leaving a stage are in equilibrium with each other, as illustrated in Figure 6 (Ramesh *et al*, 2007). This assumption forms the basis of what is known as the MESH equations (**m**aterial balances, **e**quilibrium relationships, **s**ummation equations and ent**h**alpy equations) to set up an equilibrium column model (Taylor, Krishna & Kooijman, 2003).

Using the MESH-methodology, together with Figure 6, a steady-state, equilibrium based model can be derived as follows: for a stage n, in a column with N stages (including the reboiler and condenser), the mass balance over the stage, for component i, can be written as (Wankat, 2012: 217-227)

$$z_{i,n}F_n = y_{i,n}V_n + x_{i,n}L_n - y_{i,n+1}V_{n+1} - x_{i,n-1}L_{n-1} \tag{13}$$

where the compositions of the leaving vapour and liquid streams are related by the equilibrium relationship

$$y_{i,n} = K_{i,n}x_{i,n} \tag{14}$$

with $K_{i,n}$ calculated using a suitable thermodynamic model (as will be discussed in Section 2.2.6). Furthermore, the vapour and liquid mole fractions must sum to unity

$$\sum_{i=1}^{c} y_{i,n} = 1 \tag{15}$$

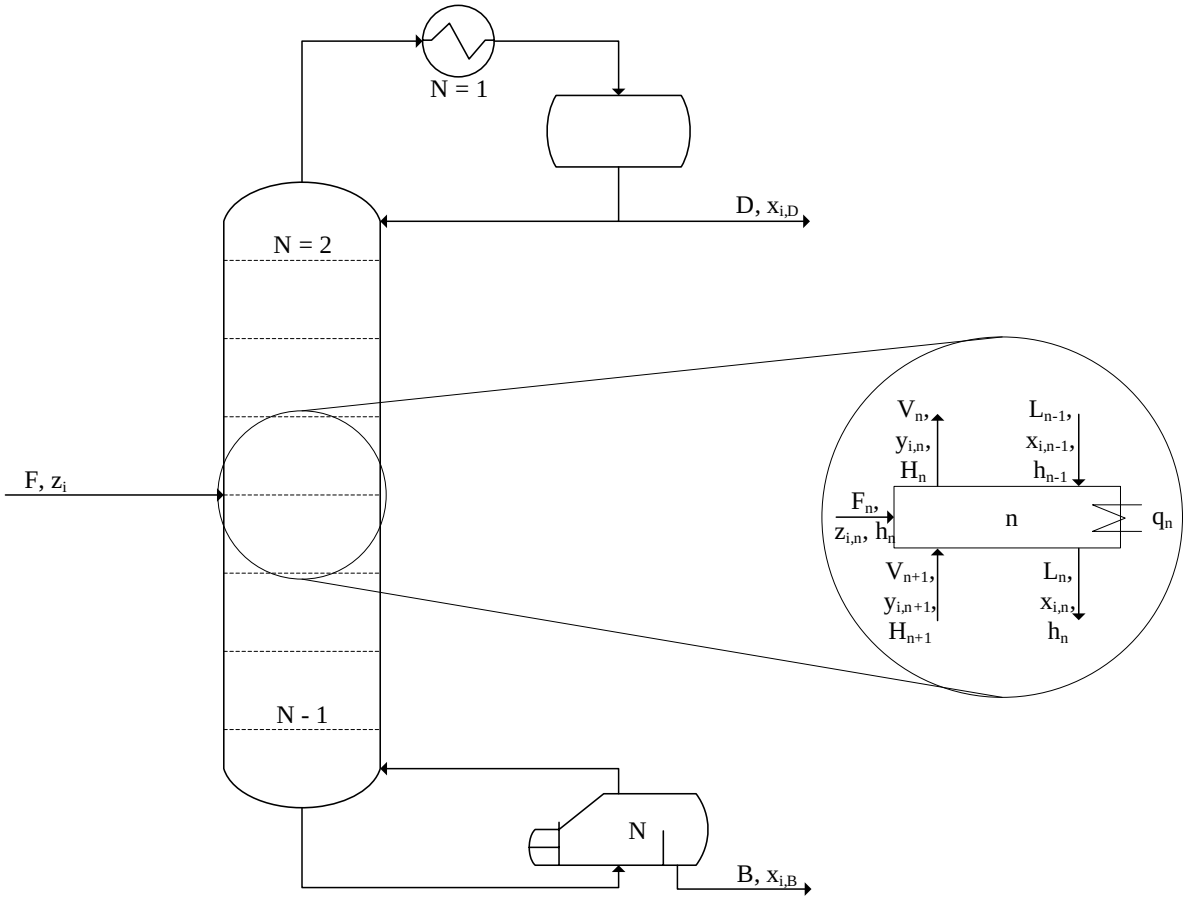

Figure 6: Column profile used in deriving steady-state, equilibrium modelling equations (adapted from Wankat (2012: 218))

and

$$\sum_{i=1}^{c} x_{i,n} = 1 \tag{16}$$

where c denotes the total number of components. Finally, the energy balance on the stage can be derived as

$$F_n h_{F_n} + q_n = L_n h_n + V_n H_n - V_{n+1} H_{n+1} - L_{n-1} h_{n-1} \tag{17}$$

where q_n is heat lost or gained from the outside environment of the column and H_n and h_n are vapour and liquid enthalpies, respectively. The same method can be used to derive material and energy balances for the reboiler and condenser. The material balance over the condenser is derived as

$$y_{i,2} V_2 = x_{i,1} L_1 + x_{i,D} D \tag{18}$$

while the energy balance is derived as

$$H_2 V_2 - Q_1 = h_1 L_1 + h_D D \tag{19}$$

where Q_1 denotes the heat removed by the condenser. For the reboiler, the material balance is derived as

$$x_{i,N-1}L_{N-1} = y_{i,N}V_N + x_{i,B}B \tag{20}$$

and the energy balance is derived as

$$h_{N-1}L_{N-1} + Q_N = H_N V_N + h_B B \tag{21}$$

with Q_N being the heat added by the reboiler. In the case of partial reboilers and condensers, the equilibrium relationship of Equation 14 will also apply.

2.2.3 Equilibrium Based Dynamic Modelling

The steady-state model presented in Section 2.2.2, can readily be extended to a dynamic model with the incorporation of an accumulation term for the liquid molar holdup, M_n^L, on a stage. The vapour hold-up is usually neglected due to the large difference in density between the liquid and the vapour (Skogestad, 1993). This is illustrated in the model set up by Ramesh *et al* (2007). The total mass balance over the condenser can be written as

$$\frac{dM_1^L}{dt} = V_2 - (L_1 + D) \tag{22}$$

while the component balances are written as

$$\frac{d(M_1^L x_{i,1})}{dt} = y_{i,2}V_2 - (L_1 + D)x_{i,D} \tag{23}$$

and the energy balance around the condenser is written as

$$\frac{d(M_1^L h_D)}{dt} = V_2 H_2 - (L_1 + D)h_1 - Q_1 \tag{24}$$

Similarly, the total mass, component and energy balances over the plates can be written as in Equations 25, 26 and 27

$$\frac{dM_n^L}{dt} = L_{n-1} - L_n - V_n + V_{n+1} + F_n \tag{25}$$

$$\frac{d(M_n^L x_{i,n})}{dt} = x_{i,n-1}L_{n-1} - x_{i,n}L_n - y_{i,n}V_n + y_{i,n+1}V_{n+1} + z_{i,n}F_n \tag{26}$$

$$\frac{d(M_n^L h_n)}{dt} = L_{n-1}h_{n-1} - L_n h_n - V_n H_n + V_{n+1}H_{n+1} + F_n h_n + Q_n \tag{27}$$

Finally, the same derivations are made for the balances over the reboiler

$$\frac{dM_N^L}{dt} = L_{N-1} - V_N - B \tag{28}$$

$$\frac{d(M_N^L x_{i,N})}{dt} = x_{i,N-1}L_{N-1} - y_{i,N}V_N - x_{i,B}B \tag{29}$$

$$\frac{d(M_N^L h_N)}{dt} = L_{N-1}h_{N-1} - V_N H_N - Bh_B + Q_B \tag{30}$$

It is worth mentioning that these equilibrium-based models usually lack some accuracy, due to the fact that a stage rarely reaches vapour-liquid equilibrium (Taylor, Krishna & Kooijman, 2003). This is usually accounted for by defining an equilibrium tray's efficiency, of which the Murphree vapour efficiency is the most popular (Ramesh *et al*, 2007). The Murphree efficiency is defined as (Wankat, 2012: 149)

$$E_{MV} = \frac{\overline{y}_n - \overline{y}_{n+1}}{y_n^* - \overline{y}_{n+1}} \tag{31}$$

where $\overline{y}_n$ and $\overline{y}_{n+1}$ denotes the average vapour mole fractions and y_n^* denotes the equilibrium vapour composition that would have been in equilibrium with the actual liquid composition. The packed column analogue to a tray efficiency is the height equivalent to a theoretical plate (HETP) (Taylor, Krishna & Kooijman, 2003). HETP can fundamentally be defined by Equation 32 (Wankat, 2012: 389), however, the literature is rich with different correlations for HETP, which are usually dependant on the type of packing in use (Taylor, Krishna & Kooijman, 2003). Using the correct HETP can therefore make it possible to model a packed column as a stage column, even though it is conceptually incorrect (Wankat, 2012: 661).

$$HETP = \frac{packing\ height}{number\ of\ theoretical\ stages} \tag{32}$$

2.2.4 Rate Based Column Modelling

Equilibrium-based distillation column models are somewhat limited in accuracy. This is due to the fact that equilibrium models are not a true representation of the actual mass-transfer taking place inside the column. The use of efficiencies and HETP models to correct for this are also limited (Taylor, Krishna & Kooijman, 2003):

- Efficiencies are actually composition dependant and vary from stage to stage, but this is rarely taken into account;
- Murphree vapour efficiencies differ from the liquid efficiencies on the same tray;

- Efficiencies and HETPs differ significantly from their steady-state values under dynamic column operation, as they vary with time.

The problems arising from the use of efficiencies are further aggravated in multicomponent systems, where various diffusion phenomena (which can't take place in binary systems) take place due to the intermolecular interactions between the multicomponent species. These phenomena include osmotic diffusion, where a component diffuses through the bulk fluid in the absence of a concentration gradient for that component; reverse diffusion, which takes place against the concentration gradient; and a diffusion barrier, where no diffusive mass transfer occurs despite the presence of a composition gradient (Krishna & Standart, 1976). Consequently, point efficiencies don't lie between 0 and 1 as expected, but in the entire range between -∞ and +∞ (Krishnamurthy & Taylor, 1985a).

The limitations associated with equilibrium models can be avoided by setting up a system of equations that models the column as a mass- and heat-transfer, rate-governed process instead of an equilibrium process. The basis of such models are illustrated in Figure 7, which can be used to represent both a column tray and a packed section (Krishnamurthy & Taylor, 1985a). Similarly to the MESH-equations for equilibrium models, Figure 7 can be represented by what is known as the MERSHQ-equations (Taylor, Krishna & Kooijman, 2003):

- M: Material balances;
- E: Energy balances;
- R: Mass- and heat-transfer rate equations;
- S: Summation equations;
- H: Hydraulic equations for pressure drop;
- Q: Equilibrium equations.

Figure 7 suggests that the mass and energy transfer on a plate or a packed section is governed by diffusion through two film layers on each side of an interface, between the liquid and vapour phases. The stage is assumed to be in mechanical equilibrium (*ie*, the vapour and liquid phases are at the same pressure), but not in thermodynamic (or thermal) equilibrium. Only at the interface are the two phases in thermodynamic and thermal equilibrium with each other (Krishnamurthy & Taylor, 1985a). These assumptions therefore require that the mass and energy balances are split for the two phases.

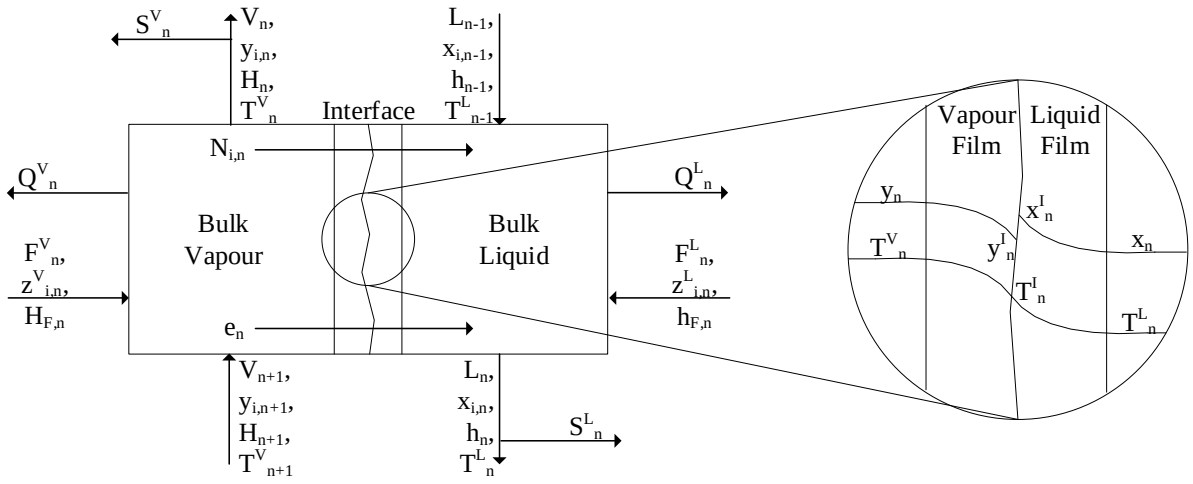

Figure 7: The basis for rate-based model derivations (adapted from Krishnamurthy & Taylor (1985a))

The mass balance for component i in the vapour phase can be written as

$$M_{i,n}^V \equiv \left(1 + r_n^V\right) v_{i,n} - v_{i,n-1} - f_{i,n}^V + \mathcal{N}_{i,n}^V = 0 \tag{33}$$

and for the liquid phase, as

$$M_{i,n}^L \equiv \left(1 + r_n^L\right) l_{i,n} - l_{i,n-1} - f_{i,n}^L - \mathcal{N}_{i,n}^L = 0 \tag{34}$$

where r_n^V and r_n^L denotes the ratio between the side stream and interstage flow for the vapour and liquid phases, respectively

$$r_n^V = \frac{S_n^V}{V_n} \tag{35}$$

$$r_n^L = \frac{S_n^L}{L_n} \tag{36}$$

The last terms ($\mathcal{N}_{i,n}^V$ and $\mathcal{N}_{i,n}^L$) of Equations 33 and 34, denotes the interphase mass transfer rates of component i in the vapour and liquid phases, respectively and are functions of the point molar fluxes ($N_{i,n}^V$ and $N_{i,n}^L$),

$$\mathcal{N}_{i,n}^V = \int N_{in}^V da_n \tag{37}$$

and

$$\mathcal{N}_{i,n}^L = \int N_{i,n}^L da_n \tag{38}$$

with da_n representing a differential amount of the total interfacial area. Performing a

material balance over the interface, I, will yield

$$M_{i,n}^{I} \equiv \mathcal{N}_{i,n}^{V} - \mathcal{N}_{i,n}^{L} = 0 \tag{39}$$

and is a result of the assumption that there is no mass accumulation around the interface (Krishnamurthy & Taylor, 1985a). Equation 39 holds when the model is extended to dynamic simulations (Kooijman & Taylor, 1995). The energy balance for the vapour phase can be written as

$$E_{n}^{V} \equiv \left(1 + r_{n}^{V}\right) V_{n} H_{n} - V_{n+1} H_{n+1} + Q_{n}^{V} - F_{n}^{V} H_{n}^{F} + \mathcal{E}_{n}^{V} = 0 \tag{40}$$

and for the liquid phase, as

$$E_{n}^{L} \equiv \left(1 + r_{n}^{L}\right) L_{n} h_{n} - L_{n+1} h_{n+1} + Q_{n}^{L} - F_{n}^{L} h_{n}^{F} - \mathcal{E}_{n}^{L} = 0 \tag{41}$$

Similar to the interphase mass transfer rates, the interphase energy transfer rates ($\mathcal{E}_{i,n}^{V}$ and $\mathcal{E}_{i,n}^{L}$) can be calculated from the point energy fluxes,

$$\mathcal{E}_{i,n}^{V} = \int e_{i,n}^{V} da_{n} \tag{42}$$

and

$$\mathcal{E}_{i,n}^{L} = \int e_{in}^{L} da_{n} \tag{43}$$

An energy balance around the interface also yields no energy accumulation

$$E_{i,n}^{I} \equiv \mathcal{E}_{i,n}^{V} - \mathcal{E}_{i,n}^{L} = 0 \tag{44}$$

The complexity of the integrations that are required by Equations 37, 38, 42 and 43 can be reduced by making the following assumptions (Krishnamurthy & Taylor, 1985a):

- There exists a constant interface state on any stage n and;
- Mass transfer coefficients on any stage n are constant.

The result of these assumptions are that the integrated mass and energy transfer rates are equal to the average fluxes on a particular stage, multiplied by the total interfacial area on that stage, as can be seen in Equations 45 to 48

$$\mathcal{N}_{i,n}^{V} = N_{i,n}^{V} a_{n} \equiv \mathcal{N}_{i,n}^{V}\left(k_{ij}^{V} a_{n},\ y_{j,n}^{I},\ \overline{y}_{j,n},\ \overline{T}_{n}^{V},\ T_{n}^{I},\ \mathcal{N}_{j,n}^{V} \quad j = 1, 2 \ldots c\right) \tag{45}$$

$$\mathcal{N}_{i,n}^{L} = N_{i,n}^{L} a_{n} \equiv \mathcal{N}_{i,n}^{L}\left(k_{ij}^{L} a_{n},\ x_{j,n}^{I},\ \overline{x}_{j,n},\ \overline{T}_{n}^{L},\ T_{n}^{I},\ \mathcal{N}_{j,n}^{L} \quad j = 1, 2 \ldots c\right) \tag{46}$$

$$\mathcal{E}_n^V = e_n^V a_n \equiv \mathcal{E}_n^V \left(h_n^V a_n,\ \overline{T}_n^V,\ T_n^I,\ \overline{y}_j,\ \mathcal{N}_{j,n}^V \right) \tag{47}$$

$$\mathcal{E}_n^L = e_n^L a_n \equiv \mathcal{E}_n^L \left(h_n^L a_n,\ \overline{T}_n^L,\ T_n^I,\ \overline{x}_j,\ \mathcal{N}_{j,n}^L \right) \tag{48}$$

here, the terms $\overline{y}_{i,n}$, $\overline{x}_{i,n}$, $\overline{T}_{i,n}^V$ and $\overline{T}_{i,n}^L$ refer to the integrated average bulk phase conditions. Calculation of the interfacial mass and heat fluxes will be discussed in Section 2.2.5. As mentioned before, the liquid and vapour phases at the interface are assumed to be in thermodynamic equilibrium with each other, therefore

$$y_{i,n}^I = K_{i,n}^I x_{i,n}^I \tag{49}$$

which also has to adhere to the summation equations

$$\sum_{i=1}^{c} y_{i,n}^I = 1 \tag{50}$$

and

$$\sum_{i=1}^{c} x_{i,n}^I = 1 \tag{51}$$

Finally, the pressure on each stage can be calculate from

$$P_n = P_{n-1} - \Delta P \tag{52}$$

where the pressure drop, ΔP, can be calculated from correlations for the specific tray or packing in use (Taylor, Kooijman & Hung, 1994). Rate equations have not been derived for the condenser and reboiler, as they can be assumed to be equilibrium contacts (Krishnamurthy & Taylor, 1985a). Although the equations presented in this section only model the steady-state, rate-based behaviour of distillation columns, they can easily be adapted to a dynamic model by adding the accumulation terms for the molar hold-ups on each phase.

2.2.5 The Maxwell-Stefan Equations

The molar transfer rates of Equations 45 and 46 can be calculated using a suitable diffusion model. Fick's law usually comes to mind, as it is a popular model taught at undergraduate level. Its accuracy is, however, limited to binary systems or very dilute multicomponent systems, due to its linear nature. It can therefore not predict the various diffusion phenomena that were mentioned in Section 2.2.4 (osmotic and reverse diffusion and the presence of diffusion barriers). The Maxwell-Stefan equations have proven to predict these phenomena quite accurately (Krishna & Wesselingh, 1997), and will therefore

be utilised in the current work.

Figure 7 depicts the concept of simultaneous mass and energy transfer across the two films. A matrix-based solution for the Maxwell-Stefan approach to mass transfer is presented in Equations 53 to 73. The vapour and liquid mass transfer rates can be calculated using Equations 53 and 54 (Krishna & Standart, 1976)

$$\boldsymbol{\mathcal{N}^V} = \boldsymbol{J^V} + \overline{\boldsymbol{y}}\mathcal{N}_t^V \quad i = 1, 2 \ldots c-1 \tag{53}$$

$$\boldsymbol{\mathcal{N}^L} = \boldsymbol{J^L} + \overline{\boldsymbol{x}}\mathcal{N}_t^L \quad i = 1, 2 \ldots c-1 \tag{54}$$

where the first column matrix term to the right hand side of the equation sign describes the diffusive component and the second term describes the convective component of the mass transfer rates. In a system with c-components, only $c-1$ equations are independent, due to the fact that the vapour and liquid compositions add to unity and the diffusive flux terms, J_i, must sum to zero (Krishna & Standart, 1979). The total mass transfer rate is obtained from the summation of the individual rates

$$\mathcal{N}_t = \sum_{i=1}^{c} \mathcal{N}_i \tag{55}$$

The vapour and liquid diffusive rates are represented by Equations 56 and 57, respectively

$$\boldsymbol{J^V} = \boldsymbol{k^V}\, a\, \boldsymbol{\Xi^V}\left(\overline{\boldsymbol{y}} - \boldsymbol{y^I}\right) \quad i = 1, 2 \ldots c-1 \tag{56}$$

$$\boldsymbol{J^L} = \boldsymbol{k^L} a\, \boldsymbol{\Xi^L}\left(\boldsymbol{x^I} - \overline{\boldsymbol{x}}\right) \quad i = 1, 2 \ldots c-1 \tag{57}$$

here, the superscript I denotes the compositions at the interface (which are assumed to be at thermodynamic equilibrium, as mentioned in Section 2.2.4), while the overhead bars indicate bulk compositions. The matrices for the vapour and liquid mass transfer coefficients are calculated using Equations 58 and 59, respectively (the $\boldsymbol{\Xi}$-matrices are flux correction matrices, and are defined in Equations 67 to 73)

$$\boldsymbol{k^V} = \boldsymbol{B^V}^{-1} \tag{58}$$

$$\boldsymbol{k^L} = \boldsymbol{B^L}^{-1}\boldsymbol{\Gamma} \tag{59}$$

where the elements for the $\boldsymbol{B}$-matrices are calculated using Equations 60 and 61

$$B_{ii} = \frac{z_i}{k_{ic}} + \sum_{\substack{k=1 \\ k \neq i}}^{c} \frac{z_k}{k_{ik}} \tag{60}$$

$$B_{ij} = -z_i \left(\frac{1}{k_{ij}} - \frac{1}{k_{ic}} \right) \tag{61}$$

The binary vapour and liquid mass transfer coefficients can be calculated using Equations 62 and 63, respectively (Krishnamurthy & Taylor, 1985b)

$$k_{ij}^V = 5.23 \left(\frac{\rho^V u^V}{a_p \mu^V} \right)^{0.7} \left(\frac{\mu^V}{\rho^V D_{ij}^V} \right)^{\frac{1}{3}} \left(\frac{D_{ij}^V P}{a_p d_p^2 RT} \right) \tag{62}$$

$$k_{ij}^L = 0.0051 \left(a_p d_p \right)^{0.4} \left(\frac{\rho^L}{M^L} \right) \left(\frac{\mu^L g}{\rho^L} \right)^{\frac{1}{3}} \left(\frac{\rho^L u^L}{a_e \mu^L} \right)^{\frac{2}{3}} \left(\frac{\mu^L}{\rho^L D_{ij}^L} \right)^{-0.5} \tag{63}$$

where a_p is the total interfacial area of the packing (in $\mathrm{m^2 \cdot m^{-3}}$ of packing), d_p is the particle diameter of the packing (in m), D_{ij}^V and D_{ij}^L are the vapour and liquid binary diffusion coefficients (in $\mathrm{m^2 \cdot s^{-1}}$) and M^L denotes the liquid phase molar mass ($\mathrm{kg \cdot kmol^{-1}}$). The effective interfacial area calculated using Equation 64

$$\frac{a_e}{a_p} = 1 - \exp \left[-1.45 \left(\frac{\sigma_c}{\sigma^L} \right)^{0.75} \left(\frac{\rho^L u^L}{a_p \mu^L} \right)^{0.1} \left(\frac{\left(u^L \right)^2 a_p}{g} \right)^{-0.05} \left(\frac{\rho^L \left(u^L \right)^2}{a_p \sigma^L} \right)^{0.2} \right] \tag{64}$$

where σ_c denotes the critical surface tension of the packing material. The units for the terms in Equations 62 to 64 are all in SI. The thermodynamic liquid correction factor (Γ) matrix in Equation 59 accounts for liquid mixture non-ideality. The elements for this matrix can be calculated using Equation 65

$$\Gamma_{ij} = \delta_{ij} + x_i \frac{\partial ln \gamma_i}{\partial x_j} \tag{65}$$

where γ_i represents the activity coefficient and will be described in Section 2.2.6.4. δ_{ij} is known as the Kronecker-delta and is described by Equation 66

$$\delta_{ij} = \begin{cases} 1, & \text{if } i = j \\ 0, & \text{if } i \neq j \end{cases} \tag{66}$$

The $\boldsymbol{\Xi}$-matrices serve as flux correction factors that converts the $\boldsymbol{J}$-matrices from zero to finite fluxes. The flux correction matrices can either be evaluated at the bulk fluid conditions (denoted by a subscript B) or at the interface (denoted by a subscript I). The $\boldsymbol{\Xi}$-matrices for the vapour phase with the bulk fluid or the interface as the diffusional path origins, are described by Equations 67 and 68, respectively (Taylor & Krishna, 1993: 162-179)

$$\boldsymbol{\Xi}_{\boldsymbol{B}}^{\boldsymbol{V}} = \boldsymbol{\Phi}^{\boldsymbol{V}} \left(\exp \left(\boldsymbol{\Phi}^{\boldsymbol{V}} \right) - \boldsymbol{I} \right)^{-1} \tag{67}$$

$$\boldsymbol{\Xi}_{\boldsymbol{I}}^{\boldsymbol{V}} = \boldsymbol{\Phi}^{\boldsymbol{V}} \exp \left(\boldsymbol{\Phi}^{\boldsymbol{V}} \right) \left(\exp \left(\boldsymbol{\Phi}^{\boldsymbol{V}} \right) - \boldsymbol{I} \right)^{-1} \tag{68}$$

where the $\boldsymbol{I}$-matrix indicates the identity matrix. The elements for the matrix of rate factors, $\boldsymbol{\Phi}$, are described by Equations 69 and 70

$$\Phi_{ii} = \frac{\mathcal{N}_i}{k_{ic}a} + \sum_{\substack{k=1 \\ k \neq i}}^{c} \frac{\mathcal{N}_k}{k_{ik}a} \tag{69}$$

$$\Phi_{ij} = -\mathcal{N}_i \left(\frac{1}{k_{ij}a} - \frac{1}{k_{ic}a} \right) \tag{70}$$

Similarly to Equations 67 and 68, the correction factor matrix for the liquid phase can be calculated by either Equation 71 or 72 (Taylor & Krishna, 1993: 209-212)

$$\boldsymbol{\Xi}_{\boldsymbol{B}}^{\boldsymbol{L}} = \boldsymbol{\Theta}^{\boldsymbol{L}} \left(\exp\left(\boldsymbol{\Theta}^{\boldsymbol{L}}\right) - \boldsymbol{I} \right)^{-1} \tag{71}$$

$$\boldsymbol{\Xi}_{\boldsymbol{I}}^{\boldsymbol{L}} = \boldsymbol{\Theta}^{\boldsymbol{L}} \exp\left(\boldsymbol{\Theta}^{\boldsymbol{L}}\right) \left(\exp\left(\boldsymbol{\Theta}^{\boldsymbol{L}}\right) - \boldsymbol{I} \right)^{-1} \tag{72}$$

where the augmented rate factor matrix, $\boldsymbol{\Theta}$, is defined by Equation 73

$$\boldsymbol{\Theta}^{\boldsymbol{L}} = \boldsymbol{\Gamma}^{-1} \boldsymbol{\Phi}^{\boldsymbol{L}} \tag{73}$$

Analogously to the mass transfer rates, the heat transfer rates are made up of a conductive heat flux term and a convective contribution due to enthalpic interphase transport (Krishnamurthy & Taylor, 1985a). The vapour and liquid phase heat transfer rates are defined by Equations 74 and 75, respectively

$$\mathcal{E}^V = q^V + \sum_{i=1}^{c} \mathcal{N}_{i,n}^V H_{i,n} \tag{74}$$

$$\mathcal{E}^L = q^L + \sum_{i=1}^{c} \mathcal{N}_{i,n}^L h_{i,n} \tag{75}$$

The vapour phase conductive heat flux, that has been corrected for finite flux, is defined by Equation 76 (Taylor & Krishna, 1993: 279-281)

$$q^V = h^V a \frac{\epsilon^V}{\left(\exp \epsilon^V - 1\right)} \left(T^V - T^I \right) \tag{76}$$

with ϵ^V obtained from Equation 77

$$\epsilon^V = \frac{\sum_{i=1}^{c} \mathcal{N}_i C p_i^V}{h^V a} \tag{77}$$

For the liquid phase, Equation 78 does not incorporate a finite flux correction factor. This is due to the fact that the liquid phase heat transfer coefficient, h^L, usually has a

high enough value that results in the correction factor approximating unity.

$$q^L = h^L a \left(T^L - T^I\right) \tag{78}$$

The zero flux heat transfer coefficients can be estimated from appropriate analogies that relates the heat transfer coefficients to mass transfer coefficients. The Chilton-Colburn analogy can be used for the vapour phase (Equation 79) while a penetration-type mechanism can be used for the liquid phase (Equation 80) (Krishnamurthy & Taylor, 1985b)

$$h^V = k^V C_P^V \left(Le^V\right)^{\frac{2}{3}} \tag{79}$$

$$h^L = k^L C_P^L \left(Le^L\right)^{\frac{1}{2}} \tag{80}$$

where Le is the Lewis number, and is defined by Equation 81

$$Le = \frac{k}{\rho C_P D_{ij}} \tag{81}$$

with k, the thermal conductivity, in $\mathrm{W{\cdot}m^{-1}K^{-1}}$. The only thing left to solve for is the mass transfer rate of component c. This cannot be accomplished explicitly with the use of Equations 53 to 73, due to the restriction posed by the fact that there exists only $c-1$ independent species. This complication is known as the "bootstrap problem" and, for systems with simultaneous mass and energy transfer, can be overcome with the help of Equation 82 (when using the vapour phase diffusion flux) or Equation 83 (when using the liquid phase diffusion flux), which calculates the total mass transfer rates (Taylor & Krishna, 1993: 281-282)

$$\mathcal{N}_t = \frac{q^L - q^V}{\lambda_y} - \frac{\sum_{i=1}^{c} \left(\lambda_i - \lambda_n\right) J_i^V}{\lambda_y} \tag{82}$$

$$\mathcal{N}_t = \frac{q^L - q^V}{\lambda_x} - \frac{\sum_{i=1}^{c} \left(\lambda_i - \lambda_n\right) J_i^L}{\lambda_x} \tag{83}$$

where λ_i is defined as the difference between the vapour and liquid enthalpies of each component i

$$\lambda_i = H_i - h_i \tag{84}$$

while λ_y can be calculated from Equation 85

$$\lambda_y = \sum_{i=1}^{c} \lambda_i y_i \tag{85}$$

and λ_x from Equation 86

$$\lambda_x = \sum_{i=1}^{c} \lambda_i x_i \tag{86}$$

Finally, the mass transfer rate for component c can then be calculated using Equation 55.

In summary, mass transfer rates ($\mathcal{N}_i$) are obtained by matrix evaluations, which consists of a diffusive flux column matrix ($\boldsymbol{J}$) and a convective flux column matrix ($\overline{\boldsymbol{y}}\mathcal{N}_t$). The diffusive flux matrix, in turn, comes from the product of a mass transfer coefficient square matrix ($\boldsymbol{k}a$), a finite flux correction matrix ($\boldsymbol{\Xi}$) and a concentration gradient driving force (defined as $\left(\overline{\boldsymbol{y}} - \boldsymbol{y^I}\right)$ for the vapour phase and $\left(\boldsymbol{x^I} - \overline{\boldsymbol{x}}\right)$ for the liquid phase). The vapour phase mass transfer coefficient matrix is calculated by inverting a matrix, $\boldsymbol{B}$ (with its elements defined by Equations 60 and 61). The liquid phase mass transfer coefficient is corrected for non-ideal molecular interactions, by multiplying the inverted liquid phase $\boldsymbol{B}$-matrix, with a thermodynamic correction factor matrix, $\boldsymbol{\Gamma}$ (its elements are defined by Equations 65 and 66).

Furthermore, the vapour and liquid phase flux correction matrices are characterised by the rate factor matrix ($\boldsymbol{\Phi}$) for the vapour phase (with elements defined by Equations 69 and 70) and the augmented rate factor matrix ($\boldsymbol{\Theta}$) for the liquid phase (which is defined in Equation 73). Unfortunately, for a system containing c-components, the matrix algebra only delivers $c-1$ mass transfer rates, as only $c-1$ equations are independent. This is problematic, as all the mass transfer rates are required to calculate $\mathcal{N}_t$. For distillation systems, however, $\mathcal{N}_t$ can be calculated by either Equation 82 or 83 (which is derived from the interphase energy transfer model), which solves this problem.

2.2.6 Thermodynamic Modelling

Using the correct thermodynamic model to describe the vapour-liquid equilibrium (VLE) interactions of the components that need to be separated, forms an important first step towards generating a mathematical characterisation of the total distillation system. Such a model, which uses the Peng-Robinson (PR) equation of state (EoS), modified by the Mathias-Copeman (MC) alpha function and utilising the Wong-Sandler (WS) mixing rules, together with the non-random-two-liquid (NRTL) activity coefficient, has been fitted to experimental data for the TFE-OFCB (Conradie *et al* (2012)), TFE-HFP (Conradie *et al* (2013)) and HFP-OFCB (Conradie *et al* (2015)) binary systems. A similar model has been used by Shiflett & Sandler (1998) to predict the VLE-behaviour of seven fluorocarbon binary systems.

2.2.6.1 Peng-Robinson Equation of State

Peng & Robinson (1976) presented their cubic equation of state (Equation 87), a modified version of the van der Waals EoS, as a relationship that can predict the vapour pressure of single component systems, as well as the volumetric behaviour and phase behaviour of single and multicomponent systems.

$$P = \frac{RT}{v-b} - \frac{a(T)}{v(v+b)+b(v-b)} \tag{87}$$

At the critical point of a single specie, we have

$$a(T_c) = 0.45724\frac{R^2T_c^2}{P_c} \tag{88}$$

$$b(T_c) = 0.07780\frac{RT_c}{P_c} \tag{89}$$

Since only the a-constant is a function of temperature, its value is calculated by incorporating a dimensionless alpha-function

$$a(T) = a(T_c) \times \alpha(T_r, \omega) \tag{90}$$

while

$$b(T) = b(T_c) \tag{91}$$

Equation 87 can be rewritten as a cubic polynomial, to allow for simple root solving to produce three roots. In the two-phase pressure and temperature ranges, the largest positive root will yield the vapour-phase compressibility factor (Z), while the smallest positive root will be the liquid compressibility factor. The polynomial expansion is represented by Equation 92

$$Z^3 - (1-B)\,Z^2 + \left(A - 3B^2 - 2B\right)Z - \left(AB - B^2 - B^3\right) = 0 \tag{92}$$

where

$$A = \frac{aP}{R^2T^2} \tag{93}$$

$$B = \frac{bP}{RT} \tag{94}$$

$$Z = \frac{Pv}{RT} \tag{95}$$

2.2.6.2 Mathias-Copeman Alpha Function

The thermodynamic model prescribed by Conradie (2011) for the three binary systems does not make use of the original Peng-Robinson alpha function, but rather the Mathias-Copeman alpha function

$$\alpha_i(T) = \left[1 + c_{1,i}(1 - \sqrt{T_r}) + c_{2,i}(1 - \sqrt{T_r})^2 + c_{3,i}(1 - \sqrt{T_r})^3\right]^2 \tag{96}$$

where the coefficients, $c_{1,i}, c_{2,i}$ and $c_{3,i}$ are experimentally fitted to Equation 96 for component i. The values for these coefficients are presented in Table 2. Furthermore, the reduced temperature, T_r, is calculated by dividing the system temperature by the component's critical temperature.

Table 2: Mathias-Copeman alpha function coefficients for the three binary systems

	Coefficients		
Component	c_1	c_2	c_3
TFE-OFCB binary system[a]			
TFE	0.5939	0.7535	0.3769
OFCB	0.8471	0.4952	-0.5524
TFE-HFP binary system[b]			
TFE	0.5939	0.7535	0.3769
HFP	0.8872	-0.1307	0.7628
HFP-OFCB binary system[c]			
HFP	0.9188	-0.8018	3.8497
OFCB	0.8542	0.4006	-0.2659

[a](Conradie *et al* (2012))
[b](Conradie *et al* (2013))
[c](Conradie *et al* (2015))

2.2.6.3 Wong-Sandler Mixing Rules

The Wong-Sandler mixing rules were developed to extend the use of cubic equations of state in thermodynamic property predictions, especially VLE-interactions, to non-ideal mixtures. Wong, Orbey & Sandler (1992) also showed that this mixing model can accurately extrapolate data gathered at moderate temperatures and pressures, to much harsher process conditions. The mixture parameters are calculated using Equations 97 and 98

$$b_m = \frac{\sum_i \sum_j x_i x_j \left(b - \frac{a}{RT}\right)_{ij}}{1 + \frac{A^E_\infty(x)}{RT} - \sum_i x_i \left(\frac{a_i}{b_i RT}\right)} \tag{97}$$

$$a_m = b_m \left[\sum_i x_i \frac{a_i}{b_i} - \frac{A^E_\infty(x)}{\sigma}\right] \tag{98}$$

where A^E_∞ is the Helmholtz free energy at infinite pressure. Furthermore, the $\left(b - \frac{a}{RT}\right)_{ij}$ component in Equation 97 is calculated using Equation 99

$$\left(b - \frac{a}{RT}\right)_{ij} = \frac{1}{2}\left[\left(b_i - \frac{a_i}{RT}\right) + \left(b_j - \frac{a_j}{RT}\right)\right](1 - k_{ij}) \tag{99}$$

while the σ-parameter in Equation 98, for the Peng-Robinson EoS, can be calculated using Equation 100

$$\sigma = \frac{ln\left(\sqrt{2} - 1\right)}{\sqrt{2}} = -0.62323 \tag{100}$$

Finally, the k_{ij}-parameter in Equation 99 can be calculated using Equation 101

$$k_{ij} = aT^2 + bT + c \tag{101}$$

which has been fitted to the data produced by Conradie (2011: 107-116). The constants for Equation 101 are given in Table 3.

Table 3: Constants to calculate k_{ij} using Equation 101 (Conradie, 2011: 122)

Binary system	Constants		
	a	b	c
TFE-HFP	9.251×10^{-5}	-3.928×10^{-2}	3.679
TFE-OFCB	-6.019×10^{-4}	0.3374	-47.19
HFP-OFCB	1.023×10^{-4}	-6.254×10^{-2}	9.36

2.2.6.4 NRTL Activity Coefficient

The non-random-two-liquid (NRTL) activity coefficient model can accurately predict non-ideal liquid phase behaviour, including partial immiscibility (Prausnitz, Lichtenthaler & de Azevedo, 1999: 261-262). Equation 102 defines the NRTL excess Gibbs energy for a binary system

$$\frac{G^E}{RT} = x_1 x_2 \left(\frac{\tau_{21} G_{21}}{x_1 + x_2 G_{21}} + \frac{\tau_{12} G_{12}}{x_2 + x_1 G_{12}}\right) \tag{102}$$

where the coefficients, τ_{ij}, are dependent on temperature and the energy interaction parameters, g_{ij}

$$\tau_{ij} = \frac{g_{ij} - g_{jj}}{RT} \tag{103}$$

Similarly, Conradie (2011: 121-122) fitted the temperature dependence of the τ_{ij}-values to Equation 104

$$\tau_{ij}RT = a + bT^{-1} + fT \tag{104}$$

with the constants, a, b and f presented in Table 4. Furthermore,

$$G_{ij} = exp(-\alpha\tau_{ij}) \tag{105}$$

where the α-parameter is related to the mixture's non-randomness and can vary from 0.2 to 0.47. It is, however, recommended to use a value of 0.3 (Prausnitz *et al*, 1999: 261). Equation 106 is used to calculate the activity coefficient of a component in a binary mixture

$$ln\gamma_i = x_j^2 \left[\tau_{ji} \left(\frac{G_{ji}}{x_i + x_j G_{ji}} \right)^2 + \frac{\tau_{ij} G_{ij}}{(x_j + x_i G_{ij})^2} \right] \tag{106}$$

Equations 102 and 106 can be extended to multicomponent mixtures (Equations 107 and 108) and only require the constants obtained from binary data (Prausnitz *et al*, 1999: 287-290).

$$\frac{G^E}{RT} = \sum_{i=1} x_i \frac{\sum\limits_{j=1} \tau_{ji} G_{ji} x_j}{\sum\limits_{l=1} G_{li} x_l} \tag{107}$$

$$ln\gamma_i = \frac{\sum\limits_{j=1} \tau_{ji} G_{ji} x_j}{\sum\limits_{l=1} G_{li} x_l} + \sum_{j=1} \frac{x_j G_{ij}}{\sum\limits_{l=1} G_{lj} x_l} \left(\tau_{ij} - \frac{\sum\limits_{r=1} x_r \tau_{rj} G_{rj}}{\sum\limits_{l=1} G_{lj} x_l} \right) \tag{108}$$

Table 4: Constants to calculate τ_{ij} using Equation 104 (Conradie, 2011: 122)

Binary system	Constants					
	a_{ij}	a_{ji}	b_{ij}	b_{ji}	f_{ij}	f_{ji}
TFE-HFP	10.71	-3.807	-2336	830.2	0	0
TFE-OFCB	-1.039	1.92	0	0	9.0115×10^{-3}	-0.05979
HFP-OFCB	2.463	-1.076	-360.7	104.9	0	0

2.2.6.5 Gamma-Phi VLE Algorithms

Simple phase equilibria calculations for ideal systems are based on the combination of Raoult's (Equation 109) and Dalton's (Equation 110) laws

$$p_i = x_i P_i^* \tag{109}$$

$$p_i = y_i P \tag{110}$$

where the vapour pressure of component i, P_i^*, is usually calculated using Antoine's equation

$$lnP_i^* = A_i - \frac{B_i}{T + C_i} \tag{111}$$

Many VLE systems are, however, far from ideal and cannot be predicted using Equations 110 to 111 without introducing an error. Consequently, these equations need to be modified to account for the non-ideal behaviour in both the liquid and vapour phases, as illustrated in Equation 112

$$\Phi_i y_i P = \gamma_i x_i P_i^* \tag{112}$$

where liquid phase deviations are accounted for by the activity coefficient, γ_i, while vapour phase non-idealities are corrected by the introduction of a fugacity coefficient, Φ_i (Smith, Van Ness & Abbott, 2005: 545-547)

$$\Phi_i = \frac{\hat{\phi}_i}{\phi_i^*} \exp\left[-\frac{v_i^l \left(P - P_i^*\right)}{RT}\right] \tag{113}$$

with $\hat{\phi}_i$ denoting the fugacity coefficient of component i in the mixture, while ϕ_i^* denotes the pure component fugacity at its saturation pressure. The exponential term to the right in Equation 113 is known as the Poynting factor and serves as a correction factor at increased pressures.

Peng & Robinson (1976) derived a pure component fugacity coefficient for their equation of state and presented it as Equation 114

$$\ln \phi_i^* = Z - 1 - \ln\left(Z - B\right) - \frac{A}{2B\sqrt{2}} \ln\left(\frac{Z + \left(1 + \sqrt{2}\right) B}{Z + \left(1 - \sqrt{2}\right) B}\right) \tag{114}$$

with A, B, and Z defined by Equations 93 to 95. Wong & Sandler (1992) took the Peng-Robinson model and applied their mixing rule in the derivation of the fugacity coefficient for species in a mixture, as shown in Equation 115.

$$\ln \hat{\phi}_i = -\ln\left[\frac{P(v-b_m)}{RT}\right] + \frac{1}{b_m}\left(\frac{\partial n b_m}{\partial n_i}\right)\left(\frac{Pv}{RT}-1\right) + \frac{1}{2\sqrt{2}}\left(\frac{a_m}{b_m RT}\right)\left[\frac{1}{a_m}\left(\frac{1}{n}\frac{\partial n^2 a_m}{\partial n_i}\right) - \frac{1}{b_m}\left(\frac{\partial n b_m}{\partial n_i}\right)\right]\ln\left[\frac{v+b_m\left(1-\sqrt{2}\right)}{v+b_m\left(1+\sqrt{2}\right)}\right] \tag{115}$$

The partial derivatives required in Equation 115 are described by Equations 116 to 121

$$\frac{\partial n b_m}{\partial n_i} = \frac{1}{(1-D)}\left(\frac{1}{n}\frac{\partial n^2 Q}{\partial n_i}\right) - \frac{Q}{(1-D)^2}\left(1-\frac{\partial n D}{\partial n_i}\right) \tag{116}$$

$$\frac{1}{RT}\left(\frac{1}{n}\frac{\partial n^2 a_m}{\partial n_i}\right) = D\frac{\partial n b_m}{\partial n_i} + b_m\frac{\partial n D}{\partial n_i} \tag{117}$$

$$\left(\frac{1}{n}\frac{\partial n^2 Q}{\partial n_i}\right) = 2\sum_j x_j\left(b-\frac{a}{RT}\right)_{ij} \tag{118}$$

$$\frac{\partial n D}{\partial n_i} = \frac{a_i}{b_i RT} + \frac{\ln \gamma_{\infty i}}{\sigma} \tag{119}$$

$$Q = \sum_i\sum_j x_i x_j\left(b-\frac{a}{RT}\right)_{ij} \tag{120}$$

$$D = \sum_i x_i\frac{a_i}{b_i RT} + \frac{A^E_\infty}{\sigma RT} \tag{121}$$

The entire thermodynamic model has temperature, pressure and composition interdependencies which need to be solved simultaneously. The algorithms presented in Figures 8 and 9 provide simple maps to help solve the set of VLE equations. Each algorithm requires either liquid or vapour composition, together with system pressure or temperature as inputs and returns the opposite values.

2.2.7 Heat Transfer Models for Condensers and Reboilers

The reboiler and condenser are important pieces of equipment, that drives distillation through the addition and removal of heat to and from the system. This, in turn, provides the boil-up vapour and reflux liquid that is required to create the counter-current fluid flow for mass transfer. Adequate heat transfer models of these pieces of equipment are therefore required for the simulations. The heat duties for both the condenser and the reboiler can be calculated using Equation 122 (Çengel & Ghajar, 2015: 651-653)

$$Q = UA\Delta T_{lm} \tag{122}$$

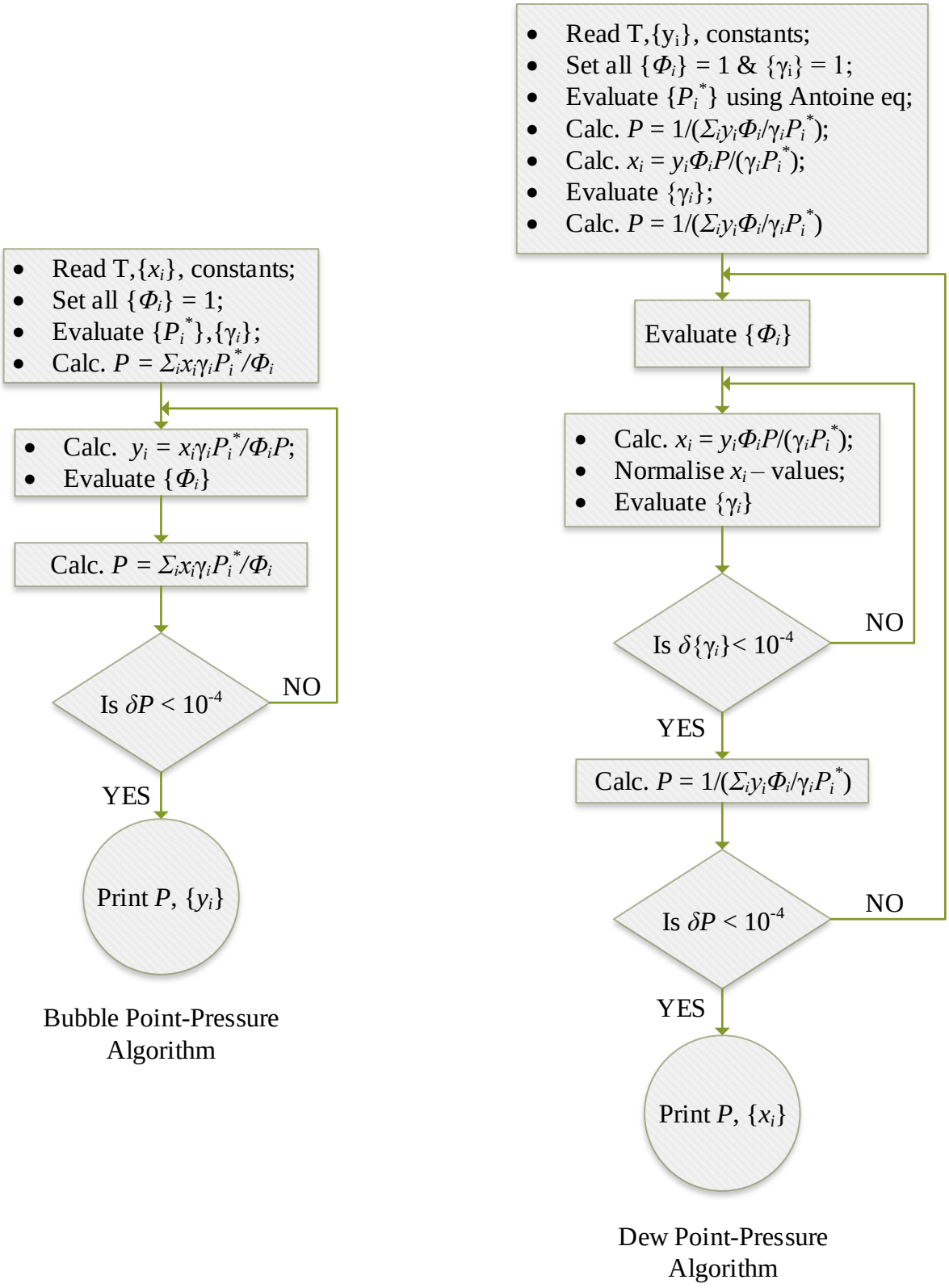

Figure 8: VLE algorithms to solve bubble point-pressure (left) dew point-pressure (right) systems (adapted from Smith, Van Ness & Abbott (2005: 548))

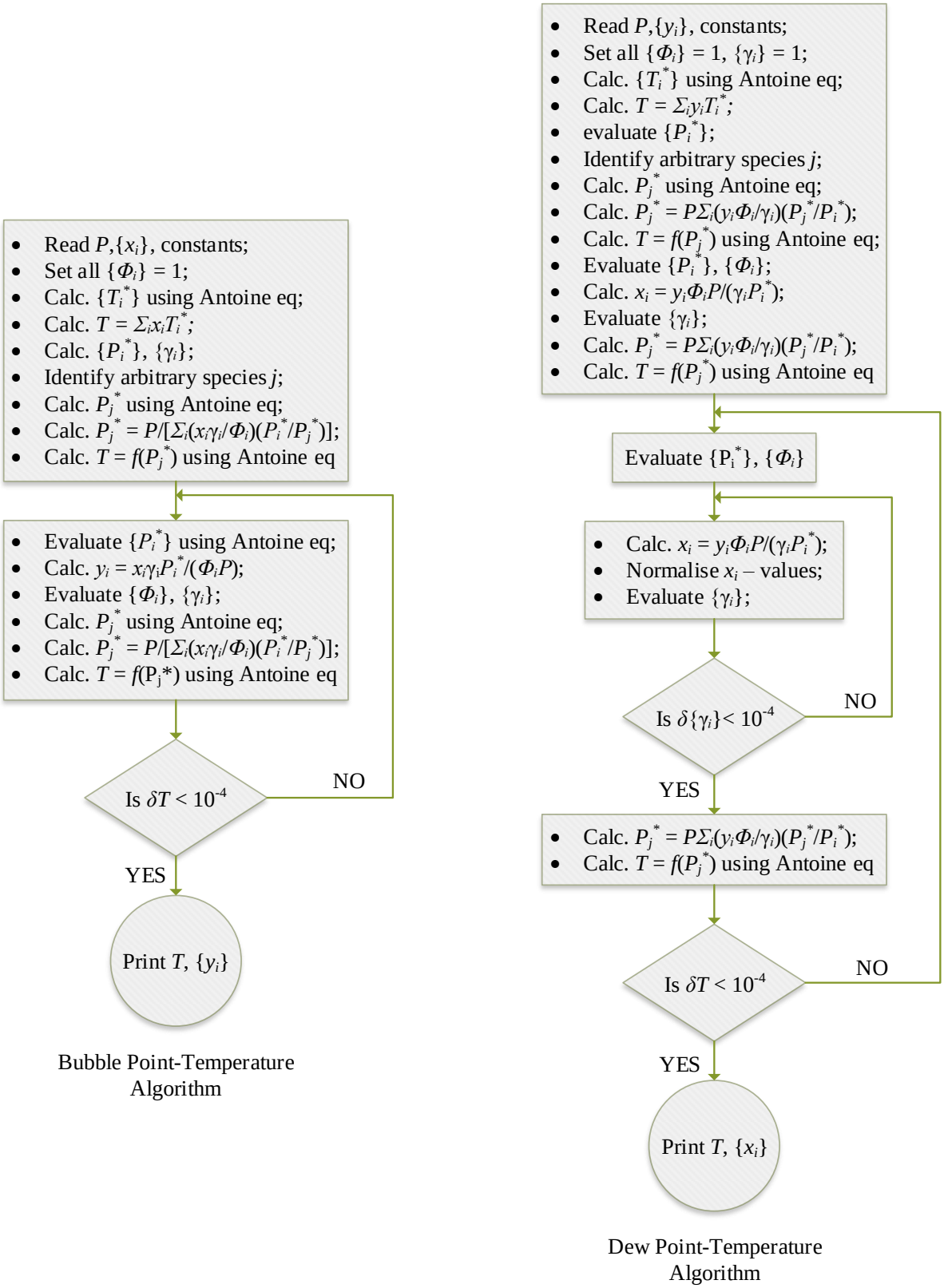

Figure 9: VLE algorithms to solve bubble point-temperature (left) dew point-temperature (right) systems (adapted from Smith, Van Ness & Abbott (2005: 549-550))

where U denotes the overall heat transfer coefficient in $W{\cdot}m^{-2}K^{-1}$, A is the heat transfer surface area in m^2 and ΔT_{lm} is the log-mean temperature difference, in K, and is defined by Equation 123

$$\Delta T_{lm} = \frac{(T_{h,in} - T_{c,out}) - (T_{h,out} - T_{c,in})}{\ln\left[\frac{(T_{h,in} - T_{c,out})}{(T_{h,out} - T_{c,in})}\right]} \tag{123}$$

The overall heat transfer coefficient-area term can be calculated by a resistance network analogue defined be Equation 124

$$\frac{1}{UA} = \frac{1}{U_o A_o} = \frac{1}{U_i A_i} = \frac{1}{h_i A_i} + \frac{\ln(D_o/D_i)}{2\pi k L} + \frac{1}{h_o A_o} \tag{124}$$

where subscript i denotes the environment of the inside fluid and subscript o denotes the outside fluid environment. Furthermore, the second term on the right-hand side of Equation 124 describes the heat conduction through a cylindrical vessel wall, such as a tube.

Equation 125 defines the heat transfer coefficient for vapour condensation inside vertical tubes for Reynolds numbers up to 30 (Sinnott, 2005: 711-713)

$$h_c = 0.926 k^L \left[\frac{\rho^L \left(\rho^L - \rho^V\right) g}{\mu^L \Gamma_v}\right]^{\frac{1}{3}} \tag{125}$$

with Γ_v defined by Equation 126

$$\Gamma_v = \frac{W_c}{N_t \pi D_i} \tag{126}$$

where W_c is the total condensate flow through the tubes and N_t is the total number of tubes in the bundle. The Reynolds number for the flow through the tubes is described by Equation 127

$$Re = \frac{4\Gamma_v}{\mu^L} \tag{127}$$

The use of Equation 125 is conservative for Reynolds numbers between 30 and 2000, after which the flow becomes turbulent and Equation 128 has to be used

$$h_c = h_i' \left[\frac{1 + \sqrt{\rho^L/\rho^V}}{2}\right] \tag{128}$$

where h_i' is calculated using Equation 129

$$h_i' = 0.021 \left(\frac{k^L}{D_i}\right) Re^{0.8} Pr^{0.43} \tag{129}$$

and the Prandtl number is described by Equation 130

$$Pr = \frac{C_P^L \mu^L}{k^L} \tag{130}$$

The heat transfer coefficient on the shell-side for shell and tube type heat exchangers can be calculated with the procedure described by Sinnott (2005: 671-675). Firstly, the cross-flow area for the row of tubes is calculated using Equation 131

$$A_s = \frac{(p_t - D_o)\, D_s l_B}{p_t} \tag{131}$$

where D_s is the shell inside diameter, l_b is the baffle spacing and p_t is the tube pitch, as illustrated in Figure 10. Next, the fluid mass flux (G_s) is calculated from the mass flow rate (W_s) and the crossflow area (A_s) using Equation 132

$$G_s = \frac{W_s}{A_s} \tag{132}$$

The shell side effective hydraulic diameter is required to calculate the Reynolds number (using Equation 135). For a tube arrangement with a square pitch, Equation 133 can be used to calculate the equivalent diameter, while Equation 134 describes the equivalent diameter for a triangular pitch tube arrangement

$$D_{e,square\ pitch} = \frac{4\left(p_t^2 - \pi\frac{D_o^2}{4}\right)}{\pi D_o} \tag{133}$$

$$D_{e,triangular\ pitch} = \frac{4\left(0.435 p_t^2 - 0.125\pi D_o^2\right)}{0.5\pi D_o} \tag{134}$$

$$Re = \frac{G_s D_e}{\mu} \tag{135}$$

Finally, Equation 136 calculates the Nusselt number and, subsequently, the heat transfer coefficient

$$Nu = \frac{h_s D_e}{k} = j_h Re Pr^{\frac{1}{3}} \left(\frac{\mu}{\mu_w}\right)^{0.14} \tag{136}$$

where j_h is a heat transfer factor that can be read off Figure 11.

The distillation column in this study uses a batch reboiler that is heated by fluid flowing through a jacket. The expected boiling mechanism is, therefore, pool boiling, which, if assumed to be in the nucleate boiling region, can be expressed by Equation 137 (Sinnott, 2005: 732-733)

$$h_{nb} = 0.00122 \left[\frac{k_L^{0.79} C_{P,L}^{0.45} \rho_L^{0.49}}{\sigma^{0.5} \mu_L^{0.29} \lambda^{0.24} \rho_V^{0.24}}\right] (T_w - T_s)^{0.24} (P_w^* - P_s^*)^{0.75} \tag{137}$$

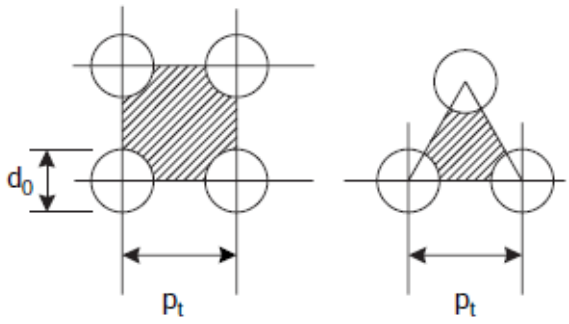

Figure 10: Square and equilateral triangle tube arrangements (Sinnott, 2005: 671)

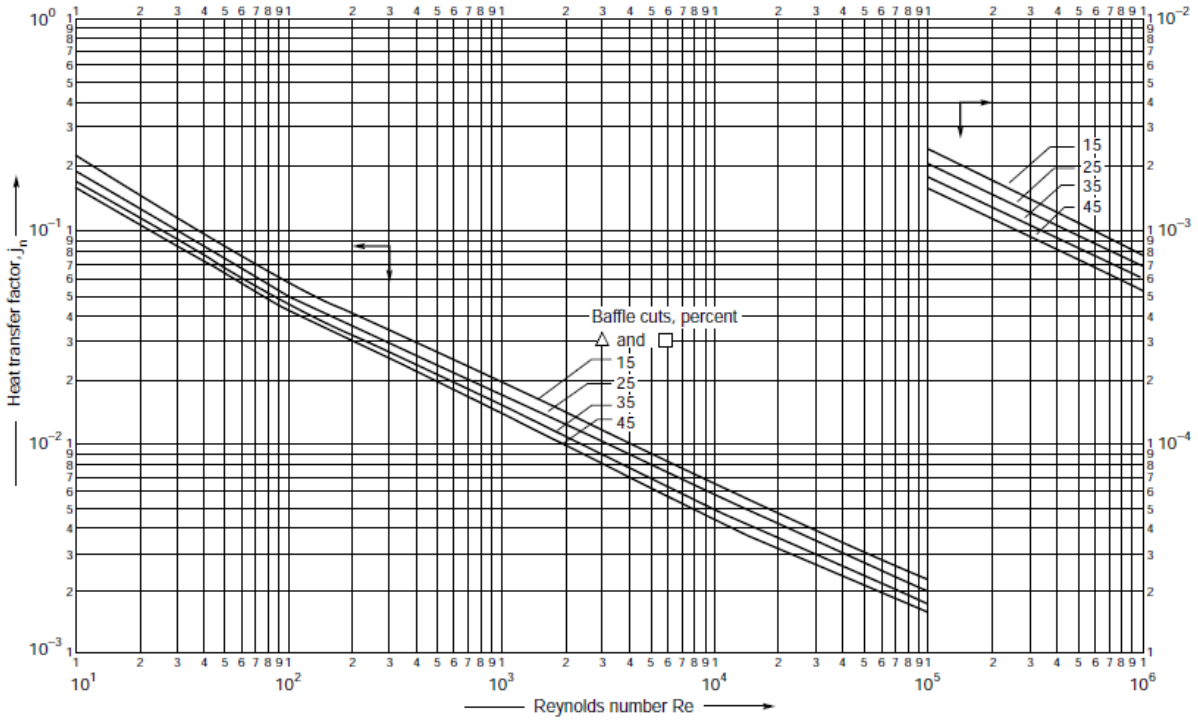

Figure 11: Shell side heat transfer factors (Sinnott, 2005: 673)

where T_w denotes the wall surface temperature with P_w^* denoting the corresponding vapour pressure at that temperature, while T_s and P_s^* denote the boiling liquid's saturation temperature and vapour pressure, respectively. The assumption for nucleate boiling will hold under excess temperature differences in the range 5 K $\leq \Delta T_{excess} \leq$ 30 K. Operating in this regime will be beneficial, as it is the pool boiling regime with the highest efficiency (Çengel & Ghajar, 2015: 602-605).

Finally, the Nusselt number for the utility fluid in the jacket can be calculated from the same models used to describe heat transfer of fluids flowing in the annulus of two concentric pipes (Sinnott, 2005: 775-777). Equation 138 describes a popular heat transfer coefficient model for flow through tubes (Çengel & Ghajar, 2015: 494-499)

$$Nu = \frac{hD_e}{k} = \frac{0.125f\,(Re - 1000)\,Pr}{1 + 12.7\,(0.125f)^{0.5}\left(Pr^{\frac{2}{3}} - 1\right)} \tag{138}$$

and is valid for the Prandtl number range $0.5 \leq Pr \leq 2000$ and the Reynolds number range $3\times10^3 \leq Re \leq 5\times10^6$. The friction factor, f, can be calculated using Equations 139 to 141, which describes the *Churchill* friction factor model (Greeff & Skinner, 2000: 28)

$$f = 8\left[\left(\frac{8}{Re}\right)^{12} + \frac{1}{(A+B)^{1.5}}\right]^{\frac{1}{12}} \tag{139}$$

$$A = \left(-2.457\ln\left[\left(\frac{7}{Re}\right)^{0.9} + 0.27\left(\frac{\varepsilon}{D_e}\right)\right]\right)^{16} \tag{140}$$

$$B = \left(\frac{37530}{Re}\right)^{16} \tag{141}$$

This model is easy to implement in simulations and delivers accurate friction factor values for all Reynolds numbers. Furthermore, the equivalent hydraulic diameter for the jacket can be calculated using Equation 142

$$D_e = \frac{4\,(D_o^2 - D_i^2)\,\frac{\pi}{4}}{\pi\,(D_o + D_i)} = D_o - D_i \tag{142}$$

It is worth mentioning that when working with heat transfer in an annulus where one of the walls are assumed to be adiabatic, a correction factor has to be applied to the Nusselt number. The correction factor where the outer wall is assumed to be adiabatic (due to insulation), is defined by Equation 143

$$F_i = 0.86\left(\frac{D_i}{D_o}\right)^{-0.16} \tag{143}$$

2.2.8 Packed Column Hydraulics

Understanding the hydrodynamics that takes place on a packed section is very important, as it governs the efficiency of the packing. The effect of liquid and vapour flow rates on pressure drop is illustrated in Figure 12. When very low liquid flow rates flow through the packing, a pressure drop that approximates the dry packing pressure drop is produced (as seen in the region AB). The reason for this is that the amount of liquid flowing through the packing has little effect on the variable hole sizes created by the packing. Pressure drop is, therefore, only proportional to the square of the vapour flow rate (Perry & Green, 1999: 14-40).

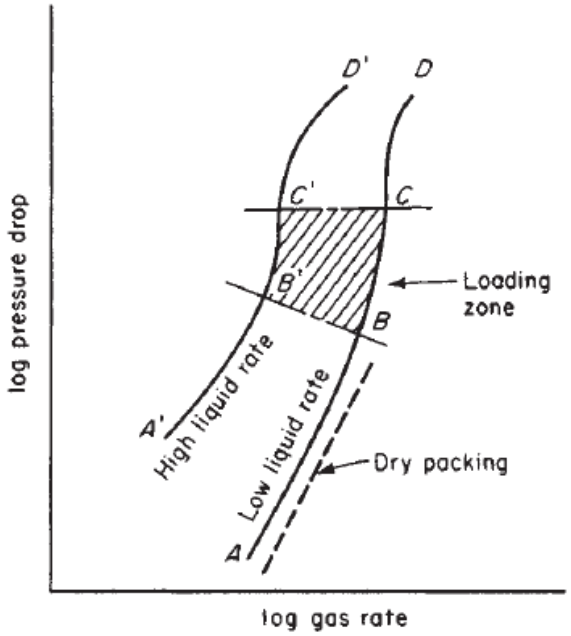

Figure 12: Packed column pressure drop zones (Perry & Green, 1999: 14-40)

Increasing the liquid rate will cause the pressure drop curve to move to the left, parallel to, but slightly above the region *AB*. This increase in liquid flow rate increases in pressure drop, as the liquid will cause the voids to start closing up, therefore increasing the frictional forces on the gas flowing through the voids. Complete filling of the packing voids creates the region *A'B'*, where the gas flow loses a portion of its energy to support the liquid in the column and the pressure drop is proportional to the gas flow rate, raised to a power smaller than two. At the point where the voids fill up with liquid, a phase inversion occurs as the packed column switches from vapour continuous to liquid continuous operation (Kister, 1992: 469-471).

Region *BB'* marks a point where an increasing gas rate starts to interfere with the liquid's ability to drain freely from the packing, causing it to accumulate or "load", thus giving this region the name *the loading zone* (shown between the regions *BC* and *B'C'*). In this region, the accumulated liquid effectively reduces the available cross-sectional area for vapour flow, causing the pressure drop to rise sharply.

A further increase in the vapour flow rate increases the liquid holdup, to a point that the liquid surface becomes continuous across the top of the packing. This causes the slopes in Figure 12 to increase until they become nearly vertical (in other words, a small increase in vapour rate results in a large increase in pressure drop). At this point (on line *CC'*), flooding occurs and column operation is no longer stable. A stable operation mode above the flooding region (above point *D* or *D'*) is, however, in some instances possible. In this region, the column essentially functions as a bubble column and is of little industrial use, due to very low mass transfer rates.

Figure 13 illustrates how the efficiency of the packing is affected when the gas rate is increased at a constant liquid to gas rate ratio (L/V). Point A on Figure 13 indicates the optimum conditions for high efficiency, however, a packed column is never designed to operate at point A, due to the sharp rise to the flood point when the vapour flow rate is increased past point A. Instead, packed columns are usually designed to operate in the pre-loading region, where the efficiency is approximately constant. This region is characterised by a turbulent liquid film which wets the packing sufficiently without excessively accumulating on the packing, thus producing good mass transfer rates (Kister, 1992: 471-472).

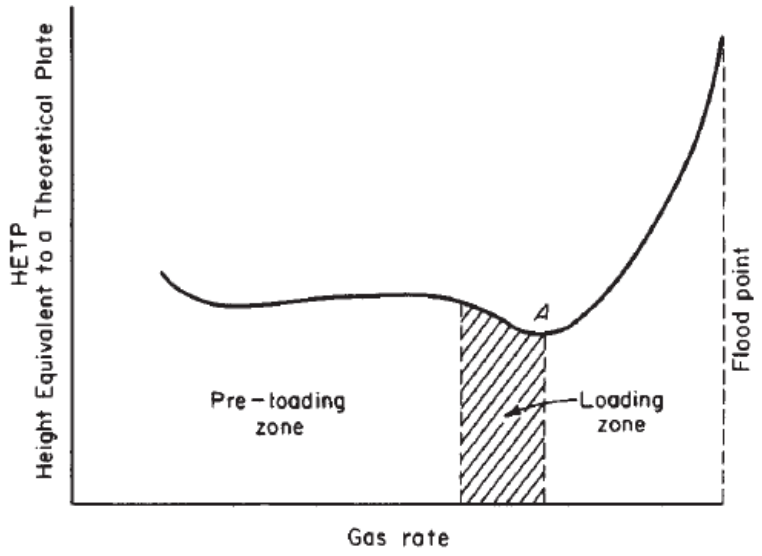

Figure 13: Packed column efficiency characteristics (Perry & Green, 1999: 14-41)

The prediction of flooding points is made possible by general pressure drop correlations (GDPC), such as in Figure 14. The figure correlates the vapour and liquid flow with the pressure drop to indicate the column's operational proximity to the flood point, with the curve at the pressure drop of 1.5 inH_2O·ft^{-1} of packing representing incipient flooding conditions (Perry & Green, 1999: 14-41–14-42). The abscissa of Figure 14 is termed the flow parameter and is calculated using Equation 144

$$F_{LG} = \frac{L}{G}\sqrt{\frac{\rho^V}{\rho^L}} \tag{144}$$

where L and G are the liquid and vapour mass fluxes in lb·ft^{-2}hr^{-1} (or kg·m^{-2}s^{-1}), respectively, and ρ^L and ρ^V are the liquid and vapour densities. The ordinate of Figure 14 is termed the capacity parameter and is calculated using Equation 145

$$C_p = C_s F^{0.5} \nu^{0.05} \tag{145}$$

here, F is the packing factor (in ft^{-1}) and is dependent on the type of packing, while ν is the kinematic viscosity in cS. C_s is calculated using Equation 146

$$C_s = u^V \sqrt{\frac{\rho^V}{\rho^L - \rho^V}} \tag{146}$$

where u^V is the superficial gas velocity in ft·s^{-1}.

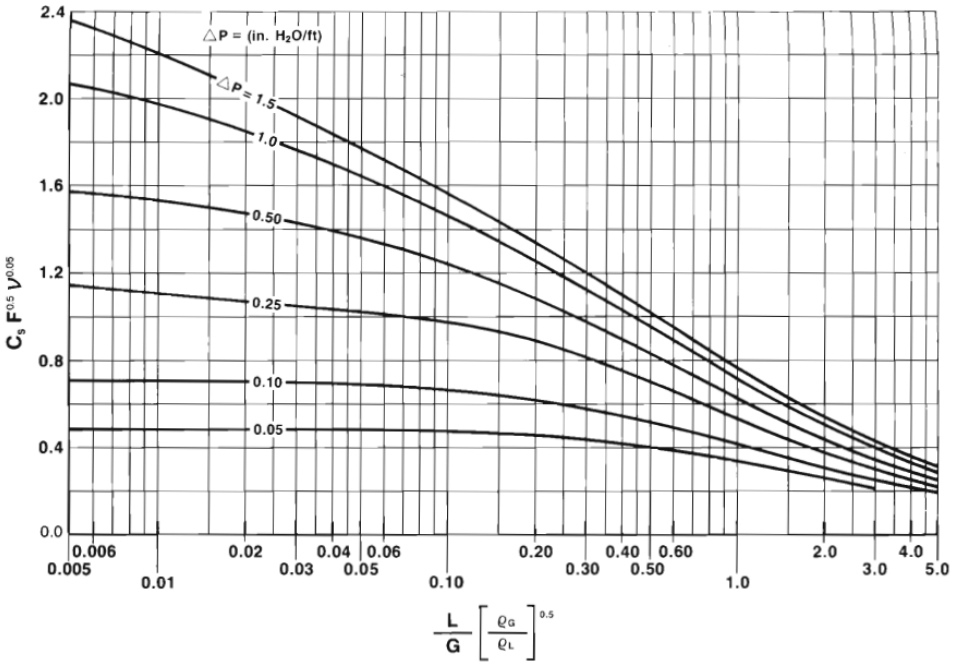

Figure 14: Generalised pressure drop correlation for packed columns (Perry & Green, 1999: 14-41)

From the discussion surrounding Figure 12, one can deduce that there are two types of pressure drop modes that are observed on a packed bed: the dry pressure drop, when only vapour flows through the packing and the irrigated (or wetted) pressure drop, created by the additional friction from the counter-current flowing liquid. It has, therefore, become standard practice to define the total pressure drop as the sum of the dry pressure drop (ΔP_d) and the pressure drop caused by the liquid flow over the packing.

$$\Delta P_t = \Delta P_d + \Delta P_L \tag{147}$$

A known pressure drop model for random packings is the Robbins-model (Perry & Green (1999: 14-42–14-45), Kister (1992: 497-499) and Ludwig (1997: 297-298)), where the dry pressure drop (in units of inH_2O·ft^{-1} of packing) is calculated using Equation 148

$$\Delta P_d = C_3 G_f^2 10^{C_4 L_f} \tag{148}$$

where C_3 and C_4 are constants defined by Equations 149 and 150, respectively

$$C_3 = 7.4 \times 10^{-8} \tag{149}$$

$$C_4 = 2.7 \times 10^{-5} \tag{150}$$

The term G_f is the gas loading factor, in lb·hr^{-1}ft^{-2}, and is calculated using Equation 151

$$G_f = \begin{cases} 986 F_s \left(\frac{F_{pd}}{20}\right)^{0.5}, & P \leq 1\ atm \\ 986 F_s \left(\frac{F_{pd}}{20}\right)^{0.5} \times 10^{0.3} \rho^V, & P > 1\ atm \end{cases} \tag{151}$$

with the gas density, ρ^V, in units of lb·ft^{-3}. The liquid loading factor, L_f, is calculated using Equation 152

$$L_f = \begin{cases} L \left[\frac{62.4}{\rho^L}\right] \left[\frac{20}{F_{pd}}\right]^{0.5} \left(\mu^L\right)^{0.1}, & \text{if } F_{pd} < 15 \\ L \left[\frac{62.4}{\rho^L}\right] \left[\frac{F_{pd}}{20}\right]^{0.5} \left(\mu^L\right)^{0.1}, & \text{if } 15 \leq F_{pd} < 200 \\ L \left[\frac{62.4}{\rho^L}\right] \left[\frac{F_{pd}}{20}\right]^{0.5} \left(\mu^L\right)^{0.2}, & \text{if } F_{pd} \geq 200 \end{cases} \tag{152}$$

with the dynamic viscosity, μ^L, in cP. The superficial F_s-factor for gas is given by Equation 153

$$F_s = u^V \left(\rho^V\right)^{0.5} \tag{153}$$

The dry packing factor, F_{pd}, is a dimensionless constant that depends on the packing type and this value is usually reported by the packing's vendor. Finally, the liquid pressure drop can be calculated using Equation 154

$$\Delta P_L = 0.4 \left[\frac{L_f}{20000}\right]^{0.1} (\Delta P_d)^4 \tag{154}$$

Due to the Robbins-model's empirical nature, care needs to be taken to ensure constant units.

Analogously to pressure drop, the total amount of liquid hold-up is made up of two terms, namely the static hold-up and the operating hold-up. The static hold-up is defined as the amount of liquid left on the packing, after operation has ceased and the column has been allowed to drain and is held in place by the forces balanced between surface tension and gravity. The operational hold-up is the dynamic hold-up on the packed section that drains away when normal operation stops (Perry & Green, 1999: 14-46–14-48).

These definitions are important in packed column design, as they allow the designer to factor in the mass of liquid on each packed section when determining the packed section and tower support loads (Ludwig, 1997: 317-319). However, for a modelling exercise, it is more convenient to describe the effect of the total liquid hold-up on the liquid flow

rate, as shown in Equation 155 (Richardson, Harker & Backhurst, 2002: 228-229)

$$h^L = 0.143 \left(\frac{L}{d_p} \right)^{0.6} \tag{155}$$

where the liquid hold-up, h^L, is in m^3 of liquid per m^3 of packing, the liquid mass flux, L, is in $kg{\cdot}m^{-2}s^{-1}$ and the equivalent packing diameter, d_p, is in mm. Equation 155 was re-written and slightly modified by Karlström & Breitholtz (1992) to produce a molar liquid flowrate as a function of the liquid hold-up on a packed section

$$L = \left(\frac{d_p^3 \left(7 h^L \frac{M}{\rho^L} \right)^5}{M^3 A^2} \right)^{1/3} \tag{156}$$

with L in $kmol{\cdot}s^{-1}$, A in m^2, M in $kg{\cdot}kmol^{-1}$ and ρ^L in $kg{\cdot}m^{-3}$.

2.2.9 Physical and Thermodynamic Properties

The following section contains the physical and thermophysical properties required to evaluate the modelling equations. Table 5 contains a list of references from where the physical properties were obtained.

Table 5: Physical properties list of references

Property	Reference
Critical properties	Conradie (2011), Yaws (2010a)
Density	Yaws (2010a), Perry & Green (1999: 2-355–2-358)
Diffusivity	Perry & Green (1999: 2-370–2-372)
	Wilke & Chang (1955)
Enthalpy	Yaws (2009)
Liquid surface tension	Yaws (2010a)
Thermal conductivity	Yaws (2003), Yaws (2010b)
Vapour pressure	Conradie (2011), Coquelet *et al* (2010), NIST (2018)
	Furukawa, McCoskey & Reilly (1953)
Viscosity	Yaws (2010a)

2.2.9.1 Critical Properties, Acentric Factors and Molar Masses

Table 6: Critical properties, acentric Factors and molar masses of TFE, HFP and OFCB

Name	Property					
	T_c (K)	P_c (kPa)	V_c (m^3·$kmol^{-1}$)	z_c (-)	M (kg·$kmol^{-1}$)	ω (-)
TFE	306.45	3944	0.172	0.266	100.016	0.223
HFP	358.9	3136	0.268	0.254	150.03	0.3529
OFCB	388.4	2777.5	0.3248	0.279	200.031	0.356

2.2.9.2 Density Data

Equation 157 correlates the liquid density

$$\rho^L = A \times B^{-\left(1-\frac{T}{C}\right)^n} \tag{157}$$

with the temperature (T) in K and the density in g·mL^{-1}. The coefficients for Equation 157 are given in Table 7.

Table 7: Liquid density coefficients for Equation 157

Name	Coefficient				Temperature Range	
	A (-)	B (-)	C (K)	n (-)	T_{min} (K)	T_{max} (K)
TFE	0.5815	0.27626	306.45	0.28571	142	306.45
HFP	0.5598	0.24208	368	0.3113	116.65	368
OFCB	0.6159	0.26446	388.37	0.2777	232.96	388.37

The pure component vapour density can be calculated by the ideal gas law that has been corrected by compressibility factor z

$$\rho^V = \frac{PM}{zRT} \tag{158}$$

which can be calculated by the Lee-Kesler method that calculates the compressibility factor of a simple fluid (denoted by a superscrpit 0) with respect to a heavy reference fluid (superscript h), as shown in Equation 159 (Perry & Green, 1999: 2-358)

$$z = z^{(0)} + \frac{\omega}{\omega^{(h)}}\left(z^{(h)} - z^{(0)}\right) \tag{159}$$

where the acentric factor of the heavy reference fluid (usually n-octane) has a value of 0.3978. The z-parameter for the simple and heavy reference fluids can be calculated by Equations 160 through 163, with the required coefficients given in Table 8.

$$z^{(i)} = \frac{P_r V_r}{T_r} = 1 + \frac{B}{V_r} + \frac{C}{V_r^2} + \frac{D}{V_r^5} + \frac{c_4}{T_r^3 V_r^2}\left[\beta + \frac{\gamma}{V_r^2}\right] \exp\left[\frac{-\gamma}{V_r^2}\right] \tag{160}$$

$$B = b_1 - \left(\frac{b_2}{T_r}\right) - \left(\frac{b_3}{T_r^2}\right) - \left(\frac{b_4}{T_r^3}\right) \tag{161}$$

$$C = c_1 - \left(\frac{c_2}{T_r}\right) - \left(\frac{c_3}{T_r^3}\right) \tag{162}$$

$$D = d_1 + \left(\frac{d_2}{T_r}\right) \tag{163}$$

Alternatively, the Peng-Robinson EoS described in Section 2.2.6.1 can be used to calculate the molar volume of a compound, after which the vapour density can be produced by dividing the compound's molar mass by the calculated molar volume. Finally, the mixed liquid and vapour densities can be calculated using Equation 164

$$\frac{1}{\rho_m} = \sum \frac{x_i}{\rho_i} \tag{164}$$

where x_i is the mass fraction of species i.

Table 8: Coefficients for the Lee-Kesler equations

Coefficient	Simple Fluid	Heavy Reference Fluid
b_1	0.1181193	0.2026579
b_2	0.265728	0.331511
b_3	0.15479	0.027655
b_4	0.030323	0.203488
c_1	0.0236744	0.0313385
c_2	0.0186984	0.0503618
c_3	0	0.016901
c_4	0.042724	0.041577
d_1	0.155488×10^{-4}	0.48736×10^{-4}
d_2	0.623689×10^{-4}	0.0740336×10^{-4}
β	0.65392	1.226
γ	0.060167	0.03754

2.2.9.3 Diffusivity Correlations

The binary vapour diffusion coefficients of non-hydrocarbon gas mixtures can be estimated using Equation 165

$$D_{ij}^{V} = \frac{1.013 \times 10^{-2} T^{1.75} \left(\frac{1}{M_i} + \frac{1}{M_j}\right)^{0.5}}{P\left(\sum v_i^{\frac{1}{3}} + \sum v_j^{\frac{1}{3}}\right)^2} \tag{165}$$

where D_{ij}^{V} has units of $m^2 \cdot s^{-1}$ when T and P are in K and Pa, respectively. The term v_i is the molecular diffusion volume of component i, made up by summing the contributions from the atoms in that molecule (Perry & Green (1999: 2-370) & Taylor & Krishna (1993: 68-69)). The atomic volumes are calculated by taking the sum of the products between the elemental ratio number and the atomic volume increments of the elements in that molecule. For instance, fluorine has an atomic volume number of 14.7, while carbon has an atomic volume number of 15.9. The molecular diffusion number for TFE can therefore be calculated as 15.9×2 + 14.7×4 = 90.6. Similarly, the molecular diffusion volumes for HFP and OFCB can be calculated as 135.9 and 181.2, respectively.

The liquid binary diffusion coefficients are calculated in a two-step process. First, the binary diffusion coefficients at infinite dilution are calculated using Equation 166

$$D_{ij}^{0,L} = 7.4 \times 10^{-8} \frac{(\phi_j M_j)^{\frac{1}{2}} T}{\mu_j V_i^{0.6}} \tag{166}$$

where component i is the solute and component j is the solvent. The term ϕ has a value of 1 for nonassociated solvents (Wilke & Chang, 1955). $D_{ij}^{0,L}$ has units of $cm^2 \cdot s^{-1}$, while M, T, V and μ are in units of $g \cdot mol^{-1}$, K, $cm^3 \cdot mol^{-1}$ and cP, respectively. Once the two binary diffusion coefficients at infinite dilution are known, they can be adjusted to the actual molar compositions with the use of Equation 167

$$D_{ij}^{L} \mu_{ij} = \left[\left(D_{ij}^{0,L} \mu_j\right)^{x_j} \left(D_{ji}^{0,L} \mu_i\right)^{x_i}\right] \alpha \tag{167}$$

where α is a thermodynamic correction factor which, for the NRTL model, has the form of Equation 168 (Taylor & Krishna, 1993: 78)

$$\alpha = 1 - 2x_i x_j \left[\frac{\tau_i G_{ji}^2}{(x_i + x_j G_{ji})^3} + \frac{\tau_j G_{ij}^2}{(x_j + x_i G_{ij})^3}\right] \tag{168}$$

2.2.9.4 Enthalpy Data

The liquid and vapour heat capacities for TFE, HFP and OFCB have been correlated against Equation 169

$$C_P = A + BT + CT^2 + DT^3 + ET^4 + FT^5 + GT^6 \tag{169}$$

with C_P in units of J·mol^{-1}K^{-1} and T in K. The coefficients for Equation 169 for the liquid phase are given in Table 9, while the coefficients for the vapour phase are given in Table 10. Mixture heat capacities can be calculated using Equation 170

$$C_{P,m} = \sum z_i C_{P,i} \tag{170}$$

where z_i represents either the liquid or the vapour molar fractions.

Table 9: Liquid heat capacity coefficients for Equation 169

Name	Coefficient				Temperature Range	
	A (-)	B (-)	C (-)	D (-)	T_{min} (K)	T_{max} (K)
TFE	-4.776	1.528	-7.907×10^{-3}	1.602×10^{-5}	143	276
HFP	32.491	1.175	-5.434×10^{-3}	1.016×10^{-5}	116.65	305.78
OFCB	-83.681	2.963	-0.01136	1.670×10^{-5}	232.96	327.77

The enthalpy of vapourisation (in kJ·mol^{-1}) for each compound can be calculated using Equation 171

$$\lambda^V = A\left(1 - \frac{T}{B}\right)^n \tag{171}$$

with the coefficients for Equation 171 given in Table 11. The same mixing rule that was used for heat capacities (Equation 170) can be used for λ^V.

Table 10: Vapour heat capacity coefficients for Equation 169 in the temperature range 250 K ≤ T ≤ 1500 K

Name	Coefficient						
	A (-)	B (-)	C (-)	D (-)	E (-)	F (-)	G (-)
TFE	18.08	0.32	-4.8×10^{-4}	4.7×10^{-7}	-3.1×10^{-10}	1.1×10^{-13}	-1.8×10^{-17}
HFP	79.38	-0.22	2.1×10^{-3}	-4.2×10^{-6}	4×10^{-9}	-1.8×10^{-12}	3.3×10^{-16}
OFCB	-40.07	1.28	-3.2×10^{-3}	5×10^{-6}	-4.6×10^{-9}	2.2×10^{-12}	-4.1×10^{-16}

Table 11: Heat of vapourisation coefficients for Equation 171

Name	Coefficient			Temperature Range	
	A (-)	B (K)	n (-)	T_{min} (K)	T_{max} (K)
TFE	25.129	306.45	0.386	142	306.45
HFP	29.323	368	0.381	116.65	368
OFCB	36.82	388.37	0.396	232.96	388.37

2.2.9.5 Liquid Surface Tension

Equation 172 correlates the liquid surface tension, in units of dyne·cm^{-1}

$$\sigma^L = A\left(1 - \frac{T}{B}\right)^n \tag{172}$$

with the coefficients A, B and n given in Table 12. The mixed surface tension can be calculated using Equation 173 (Perry & Green, 1999: 2-372)

$$\sigma_m = \sum_{i=1}^{c}\sum_{j=1}^{c}\left(\rho_m^L\right)^2\left(\frac{x_i}{\rho_i^L}\right)\left(\frac{x_j}{\rho_j^L}\right)\left(\sigma_i\sigma_j\right)^{0.5} \tag{173}$$

Table 12: Surface tension coefficients for Equation 172

Name	Coefficient			Temperature Range	
	A (-)	B (K)	n (-)	T_{min} (K)	T_{max} (K)
TFE	49.571	306.45	1.2222	142	306.45
HFP	42.321	368	1.2222	116.65	368
OFCB	54.52	388.37	1.317	232.96	388.37

2.2.9.6 Thermal Conductivity

Both the liquid and vapour thermal conductivity can be calculated by Equation 174

$$k = A + BT + CT^2 + DT^3 \tag{174}$$

where k has units of W·m^{-1}K^{-1} and T is in K. The liquid thermal conductivity coefficients are given in Table 13 and the vapour thermal conductivity coefficients are given

in Table 14. Equation 175 can be used to calculate the thermal conductivity for vapour mixtures (Perry & Green, 1999: 2-368)

$$k_m^V = \sum_{i=1}^{c} \frac{y_i k_i}{y_j A_{ij}} \tag{175}$$

with the binary interaction parameter defined by Equation 176

$$A_{ij} = \frac{1}{4}\left\{1 + \left[\frac{\mu_i}{\mu_j}\left(\frac{M_j}{M_i}\right)^{0.75}\left(\frac{T+S_i}{T+S_j}\right)\right]^{0.5}\right\}^2 \left(\frac{T+S_{ij}}{T+S_i}\right) \tag{176}$$

where S_i (or S_j) is calculated by Equation 177

$$S_{i,j} = 1.5 T_{bi,j} \tag{177}$$

with $T_{bi,j}$ denoting the pure component normal boiling temperatures. S_{ij} is calculated using Equation 178

$$S_{ij} = \sqrt{S_i S_j} \tag{178}$$

The liquid phase thermal conductivity mixing rule is given by Equation 179 (Perry & Green, 1999: 2-370)

$$k_m^L = \sum_{i=1}^{c}\sum_{j=1}^{c} \phi_i \phi_j k_{ij} \tag{179}$$

where Equation 180 describes ϕ_i

$$\phi_i = \frac{x_i V_i}{\sum_{j=1}^{c} x_j V_j} \tag{180}$$

here, V_i has units of $m^3 \cdot kmol^{-1}$. Furthermore, k_{ij} is calculated using Equation 181

$$k_{ij} = \frac{2}{\left(\frac{1}{k_i}\right) + \left(\frac{1}{k_j}\right)} \tag{181}$$

Table 13: Liquid thermal conductivity coefficients for Equation 174

Name	Coefficient			Temperature Range	
	A (-)	B (-)	C (-)	T_{min} (K)	T_{max} (K)
TFE	0.1811	-1.83E-04	-8.69E-07	172	236.45
HFP	0.1554	-1.52E-04	-4.67E-07	146.65	298
OFCB	0.1188	1.365E-05	-6.48E-07	233	369

Table 14: Vapour thermal conductivity coefficients for Equation 174 in the temperature range 250 K ≤ T ≤ 1500 K

Name	Coefficient			
	A (-)	B (-)	C (-)	D (-)
TFE	-0.010388	9.042E-05	-6.45E-09	-3.68752E-12
HFP	-0.009903	6.98365E-05	2.8834E-08	-1.62096E-11
OFCB	-0.010711	7.251E-05	1.853E-09	-3.52583E-12

2.2.9.7 Vapour Pressure

Furukawa, McCoskey & Reilly (1953) reported vapour pressure data for TFE in the temperature range 142 K ≤ T ≤ 208 K (given in Table 17), which they correlated to Equation 182

$$\log_{10} P^* = 4.71241 - \frac{972.981}{T} + 4.816562 \times 10^{-2} - 2.427347 \times 10^{-4} T^2 + 3.958793 \times 10^{-7} T^3 \tag{182}$$

where P^* is in mmHg and T in K. This data was then later fitted to the Antione equation of the form given in Equation 183 and published in the *NIST Chemistry Webbook* (NIST, 2018)

$$\log_{10} P^* = A - \frac{B}{T + C} \tag{183}$$

with P^* in bar and T in K. Antoine coefficients for HFP and OFCB were also found in the *NIST Chemistry Webbook*. These coefficients are given in Table 15.

Table 15: Vapour pressure coefficients for the Antoine equation (Equation 183)

Name	Coefficient			Temperature Range	
	A (-)	B (-)	C (-)	T_{min} (K)	T_{max} (K)
TFE	4.02877	686.188	-26.945	142	208
HFP	4.51288	1028.267	-14.694	232.5	292.9
OFCB	4.254	1007.399	-30.205	233	388.37

Conradie (2011) produced vapour pressure data for TFE, HFP and OFCB (shown in Table 16). This TFE data, which falls in a higher temperature range than that produced by Furukawa *et al* (1953), was plotted against the two models to check their extrapolation accuracy, as shown in Figure 15. The Antoine fit reported by NIST (2018) proved to be

fairly accurate, however, a new fit was performed to further minimise the errors. The new correlation was fitted to the Antoine equation of the form given in Equation 111 and yielded new coefficients with values of A = 14.068515, B = 1634.261 and C = -24.542, with P^* in kPa and T in K. The result is illustrated in Figure 16.

Table 16: Vapour pressure data for tetrafluoroethylene, hexafluoropropylene and octafluorocyclobutane generated by Conradie (2011)

TFE		HFP		OFCB	
T (K)	P^* (kPa)	T (K)	P^* (kPa)	T (K)	P^* (kPa)
248.2	864	248.14	120	247.9	39
253.34	1017	253.27	150	248.25	41
263.18	1367	263.01	225	253.38	51
273.14	1804	282.92	452	265.93	92
283.19	2340	292.76	617	267.92	99
-	-	303.07	832	269.89	110
-	-	313.38	1099	272.9	122
-	-	323.06	1408	277.87	148
-	-	334.96	1863	287.89	216
-	-	345.26	2345	292.89	257
-	-	352.78	2757	303.37	362
-	-	-	-	313.09	486
-	-	-	-	322.53	635
-	-	-	-	335.34	889
-	-	-	-	342.37	1055
-	-	-	-	352.36	1329

The same procedure was used to check the validity of the NIST (2018) Antoine fit for HFP's vapour pressure. In addition to the data produced by Conradie (2011), a second data set was found and included in the plot. As seen in Figure 16, the NIST (2018) fit loses accuracy with an increase in temperature. A new fit was therefore also correlated against the HFP vapour pressure data obtained by Coquelet *et al* (2010). The new coefficients for Equation 111 are A = 7.78208, B = 2240.999 and C = 21.597, with P^* in MPa and T in K.

Finally, the NIST (2018) Antoine model for OFCB was tested against the data produced by Conradie (2011). The model fits the data well (Figure 18) and it was therefore decided to use this model as is.

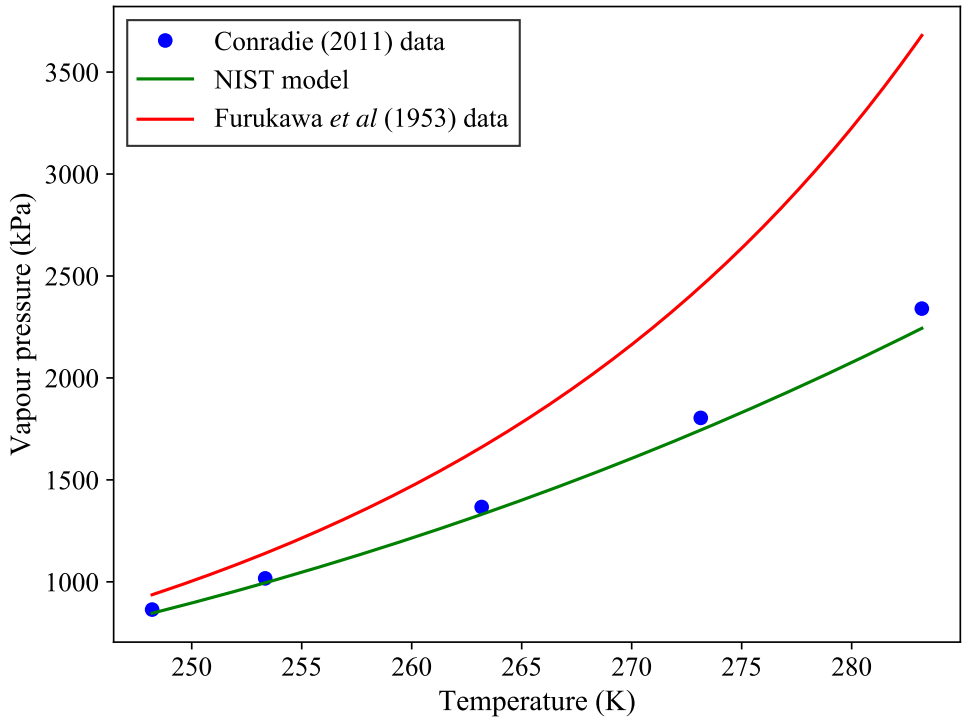

Figure 15: Tetrafluoroethylene vapour pressure model extrapolation to the data produced by Conradie (2011)

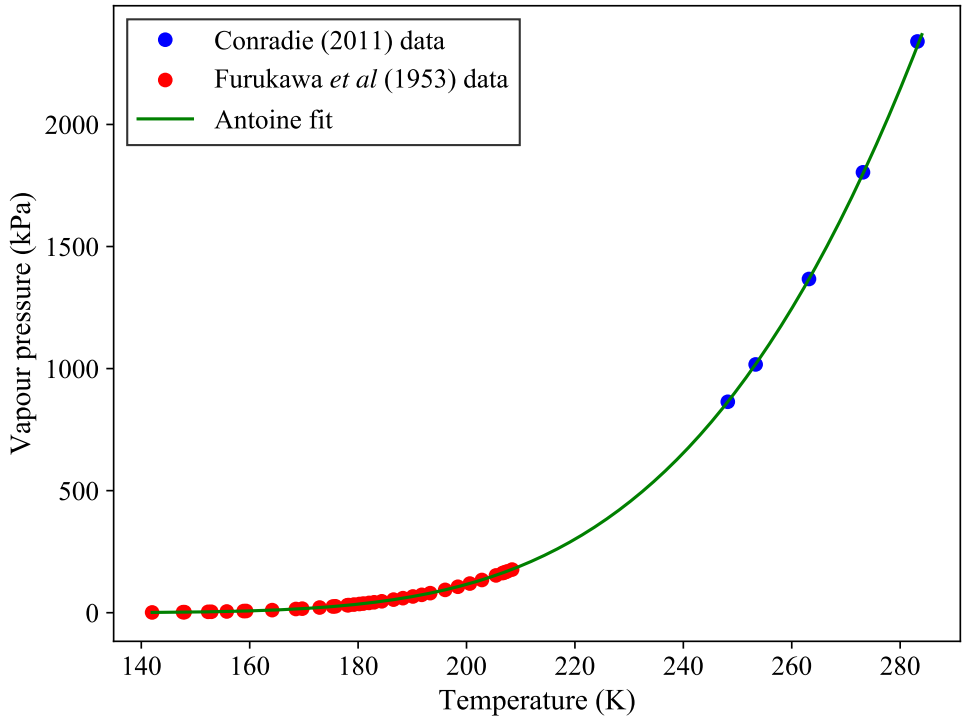

Figure 16: New Antoine equation fit to the data sets of Furukawa, McCoskey & Reilly (1953) and Conradie (2011)

Table 17: Tetrafluoroethylene vapour pressure data produced by Furukawa, McCoskey & Reilly (1953)

T (K)	P* (mmHg)
142	8.70
147.7	16.70
147.98	17.10
152.33	26.90
152.92	28.60
155.77	37.80
158.89	50.50
159.34	52.50
164.15	79.70
168.52	114.30
169.69	124.70
172.9	159.20
175.35	190.70
175.82	197.10
178.02	229.80
178.27	234.20
179.23	249.90
180.23	267.30
180.96	281.10
182.01	301.00
182.96	320.40
184.37	350.80
186.54	402.20
188.27	447.00
190.11	499.20
191.74	549.10
193.3	601.00
196.06	701.60
198.41	797.50
200.61	895.80
202.84	1005.60
205.44	1146.10
206.66	1217.80
206.99	1236.30
207.5	1268.60
208.41	1325.10

Table 18: Hexafluoropropylene vapour pressure data produced by Coquelet *et al* (2010)

T (K)	P* (MPa)
253.26	0.1497
258.26	0.1841
263.16	0.2245
268.24	0.272
273.24	0.3268
278.21	0.389
278.22	0.3886
283.23	0.459
288.21	0.5371
293.19	0.6259
298.22	0.7283
303.22	0.8397
308.21	0.9634
313.21	1.0999
318.22	1.2506
323.2	1.4135
328.21	1.5951
333.21	1.7914
338.18	2.0079
343.21	2.2438
348.22	2.5005
353.23	2.7823
355.24	2.903
356.24	2.9653
356.76	2.9985
357.06	3.0175
357.27	3.031
357.47	3.0442
357.56	3.0504
358.26	3.0951
358.76	3.1281

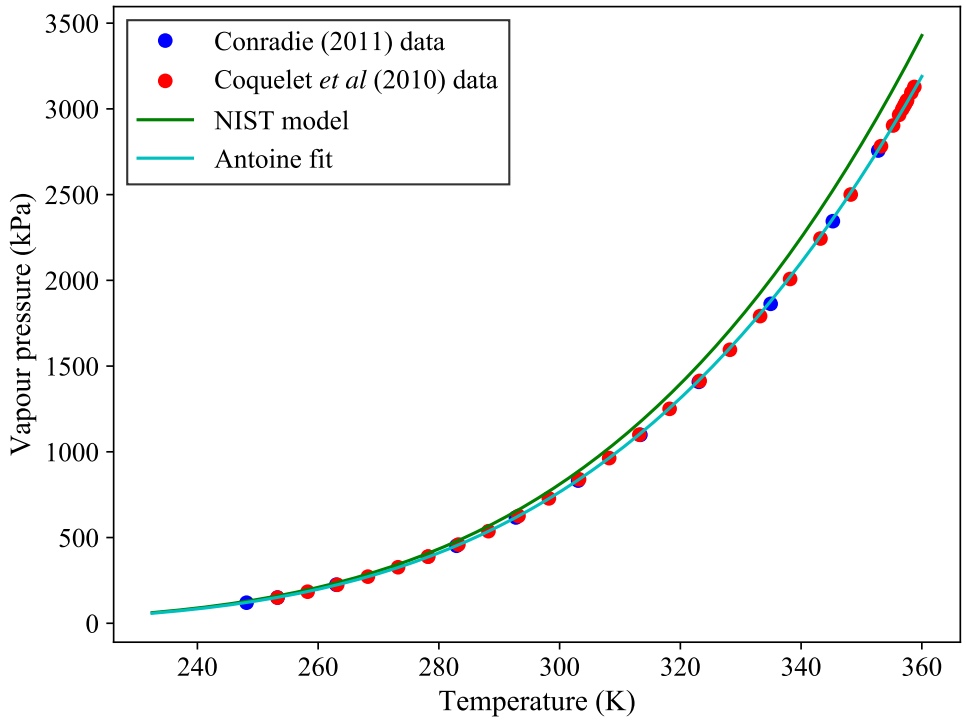

Figure 17: HFP experimental data compared to the NIST and new Antoine equation fit

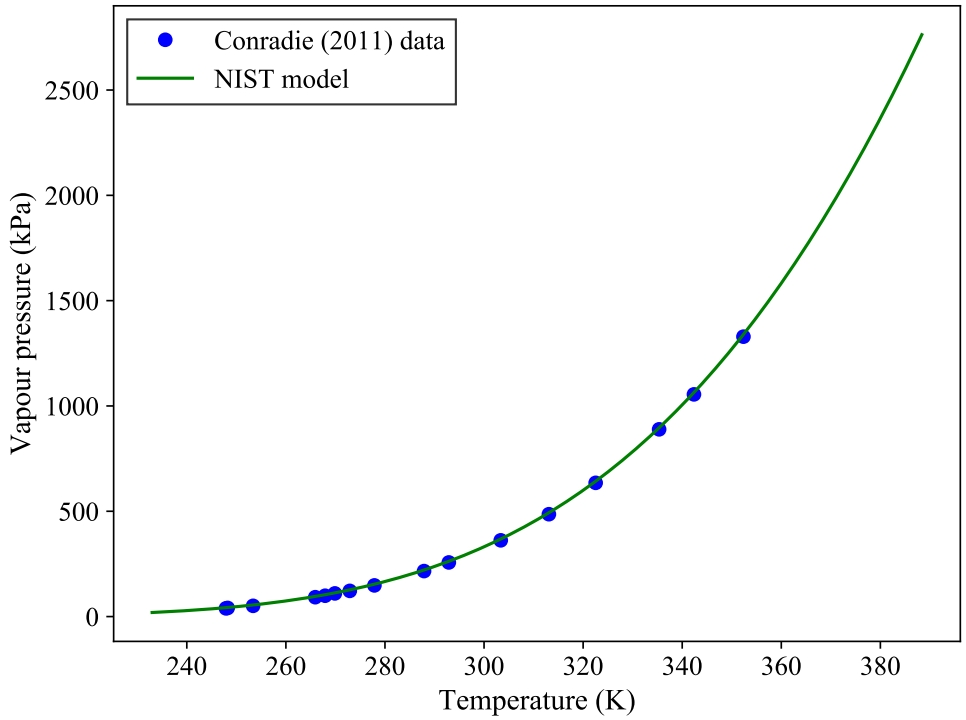

Figure 18: NIST Antoine fit compared to experimental vapour pressure data for OFCB

2.2.9.8 Viscosity Data

Equation 184 defines the liquid viscosity

$$\mu^L = 10^{A+\frac{B}{T}+CT+DT^2} \tag{184}$$

with μ^L in cP and T in K. The coefficients for Equation 184 are given in Table 19. The liquid viscosity mixing rule is given by Equation 185 (Perry & Green, 1999: 2-367)

$$\ln \mu_m = \sum x_i \ln \mu_i \tag{185}$$

Table 19: Liquid viscosity coefficients for Equation 184

Name	Coefficient				Temperature Range	
	A (-)	B (-)	C (-)	D (-)	T_{min} (K)	T_{max} (K)
TFE	-6.47315	491.334	0.0303637	-6.0987×10^{-5}	156	291
HFP	-3.83064	364.451	0.0136638	-2.55235×10^{-5}	148	350
OFCB	-2.0637	493.25	3.8652×10^{-5}	-2.0508×10^{-8}	245	388

The vapour viscosity data is correlated using Equation 186

$$\mu^V = A + BT + CT^2 + DT^3 \tag{186}$$

here, μ^V has units of cP and T is in K. Values for the coefficients in Equation 186 are given in Table 20.

Table 20: Vapour viscosity coefficients for Equation 186 in the temperature range 250 K $\leq$ T $\leq$ 1500 K

Name	Coefficient			
	A (-)	B (-)	C (-)	D (-)
TFE	-15.2117	0.620364	-2.6188×10^{-4}	6.27111×10^{-8}
HFP	-17.3897	0.533031	-2.0518×10^{-4}	4.64262×10^{-8}
OFCB	-17.1376	0.504045	-1.8595×10^{-4}	4.0854×10^{-8}

Vapour viscosity mixtures can be calculated using Equation 187

$$\mu_m = \sum_{i=1}^{c} \frac{\mu_i}{1 + \sum\limits_{\substack{j=1 \\ j \neq i}}^{c} \left(Q_{ij} \frac{x_j}{x_i} \right)} \tag{187}$$

where the parameter, Q_{ij}, can be calculated using Equation 188

$$Q_{ij} = \frac{1 + \left[\left(\frac{\mu_i}{\mu_j} \right)^{0.5} \left(\frac{M_j}{M_i} \right)^{0.25} \right]^2}{\sqrt{8} \left[1 + \frac{M_i}{M_j} \right]^{0.5}} \tag{188}$$

Model Developement

3.1 System Description

An understanding of the distillation column's physical structure, as well as the auxiliary equipment, is needed to derive a mathematical model that mimics the internal workings of the distillation system. The full distillation column system used in the laboratory is depicted by the process flow diagram (PFD) in Figure 19. The distillation column consists of five individual packed sections, with copper shavings used as the packing material. The feed to the column can be connected to any of the five supporting plates that hold up the packed sections, or to the top of the reboiler. Furthermore, the column is fitted with a split cooling jacket (split into a top and bottom half), that can be utilised to help cool the column before an experiment takes place. Further information on dimensions of the column is presented in Table 21.

Table 21: Internal working dimensions for the distillation column

Dimension	Value	Units
Total column height	1.45	m
Height of a packed section	150	mm
Column inside diameter	20	mm
Head-space between packed sections	80	mm
Approximate packing diameter	5	mm
Approximate packing length to diameter ratio	1	-

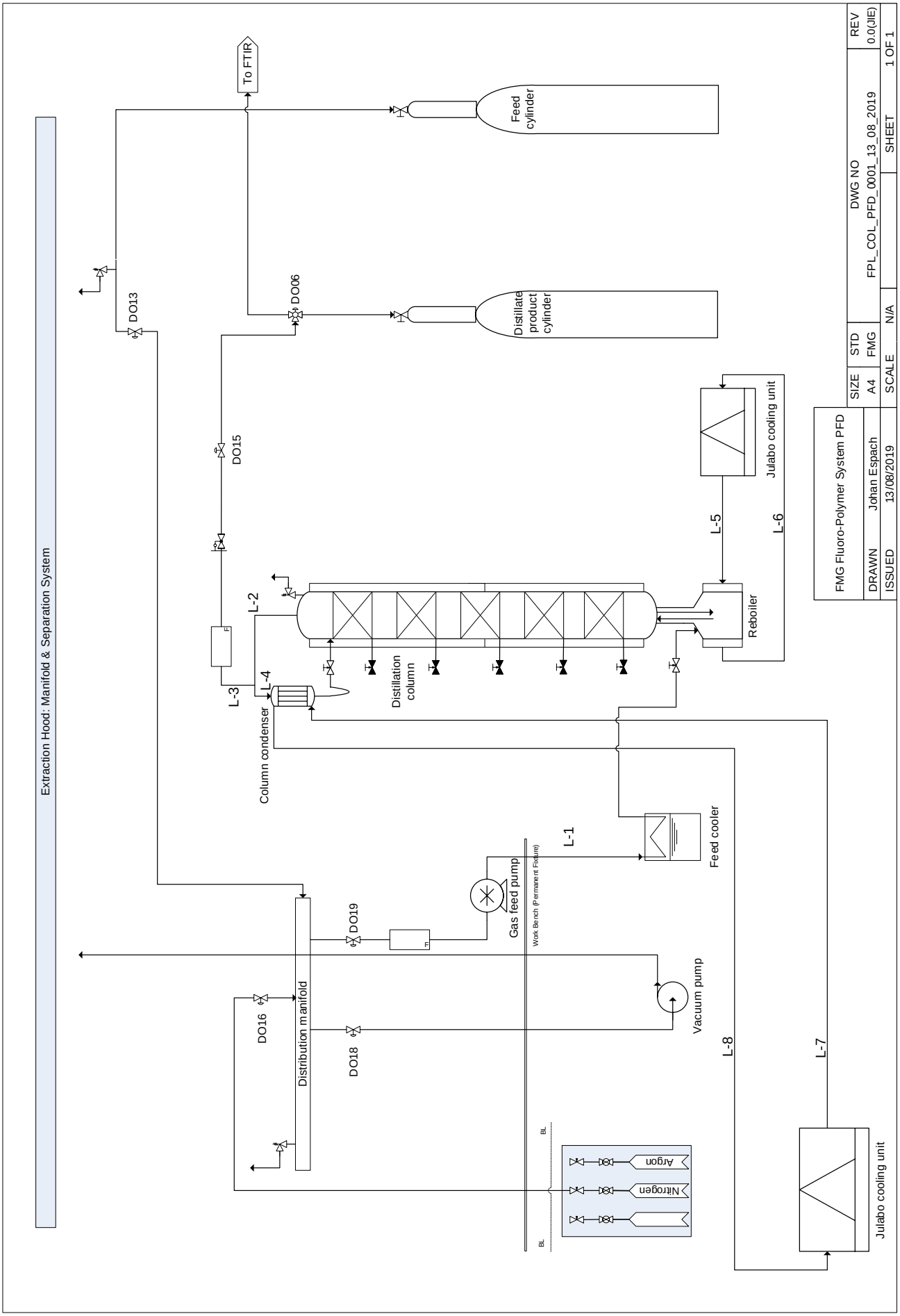

Figure 19: Distillation column process flow diagram

The condenser consists of a tube bundle that is cooled by pumping liquid methanol through the shell-side of the heat exchanger. The methanol is supplied by a Julabo cooling unit, at a user-specified temperature. The cooling fluid enters the condenser from the bottom and is directed by baffles to create a cross-flow pattern over the tube bundle. The vapours coming from the column enters the condenser at the top to fill a head-space before entering the tubes, where the condensation takes place. The distillate product is drawn off by removing some of the vapour from the head-space. A sectioned view of the condenser is presented in Figure 20, that depicts the tube bundle, baffles, vapour head-space and inlet and outlet tube connections. Some of the important condenser dimensions are given in Table 22.

The condensate coming from the condenser drains into a reflux line that is bent into an inverted siphon, before flowing back into the column. The reflux line configuration is depicted in Figure 21. The purpose of this design is to facilitate the accumulation of the reflux fluid to, in turn, ensure steady, continuous reflux flow into the column, analogously to a reflux drum on larger columns. A hand-operated needle valve is also installed in the reflux line, to offer an additional resistance to flow.

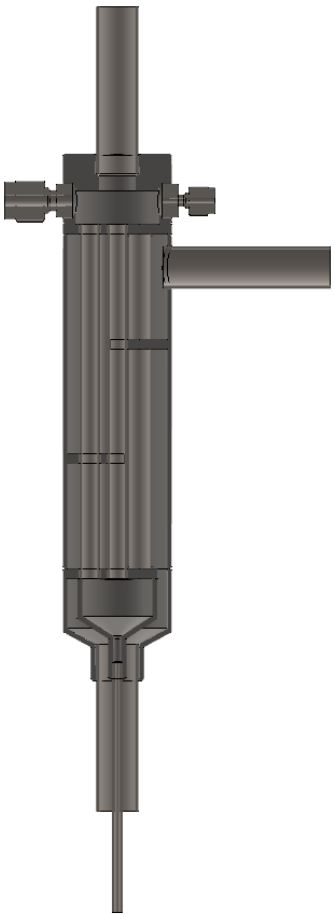

Figure 20: Sectioned view of the condenser

Table 22: Working dimensions for the condenser and reflux line

Dimension	Value	Units
Condenser		
Number of cooling tubes	6	-
Tube active cooling length	100	mm
Tube inside diameter	4.6	mm
Tube outside diameter	6.5	mm
Tube pitch (triangular)	8.97	mm
Shell inside diameter	30	mm
Number of baffles	2	-
Baffle spacing	31.3	mm
Baffle cut	0.43	%
Baffle thickness	3	mm
Vapour inlet tube diameter	10.88	mm
Condensate exit tube diameter	1.395	mm
Cooling fluid inlet & exit tube diameters	10.88	mm
Reflux Line		
Tube inside diameter	1.395	mm
Total U-tube length	290	mm
Length of horizontal tube piece	100	mm
Length of vertical tube piece	100	mm
Minimum volume required for flow	0.596	mL

Finally, a batch-style reboiler (*ie*, there is no outflow for a bottoms product) is installed at the bottom of the column. Heat transfer takes place *via* a jacket around the reboiler, with utility fluid supplied to the jacket by a second Julabo refrigeration unit. This second Julabo utilises a thermofluid that is supplied by the Julabo manufacturer. The inner cavity of the reboiler has a diameter of 104 mm, a height of 118 mm and a wall thickness of 4 mm. The jacket has an inner diameter of 165 mm and a height of 152 mm. Furthermore, the reboiler, column, condenser and reflux line are all well insulated.

The purpose of the fed-batch column configuration is to have a versatile laboratory distillation column that can (most importantly) produce TFE of an acceptable purity, given time, space and capital expenditure constraints. The configuration has the added advantage of providing a way to separate binary HFP-OFCB mixtures. Of course, an industrial-scale operation would rather see two columns for the sequential, fully-continuous separation of the initial ternary mixture, but this will add too much complexity (at a high cost) to an already complex system.

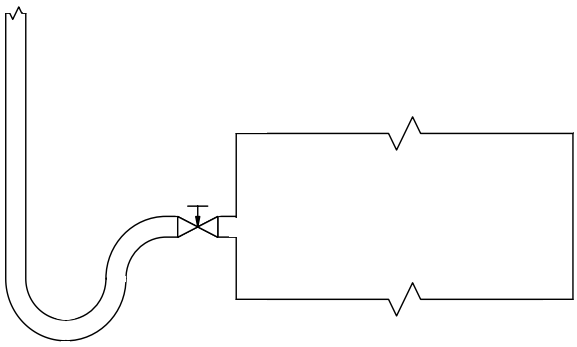

Figure 21: Schematic of the reflux line

3.2 Column Operational Considerations

The next important aspect to consider before developing a model for the column would be to theorise a column configuration that will facilitate effective separations practically. One of the biggest issues faced with the TFE-HFP-OFCB ternary system is the high freezing temperature of OFCB (-40.2 °C (Furukawa, McCoskey & Reilly, 1954)) relative to the dew point of TFE (-75.62 °C at 1 atm (Furukawa *et al*, 1953)). Consequently, the ternary mixture cannot be fed to the column as a liquid. Feeding a two-phase mixture is also not feasible, due to the difficulty of sourcing a cryogenic pump that operates at the low feed flow rates that the column was designed for. Finally, pressurising the feed to lower the dew point of TFE is also out of the question, as a pressure cap of 200 kPa has been imposed in the laboratory for safety reasons (TFE may undergo violent auto-polymerisation at high pressures).

The feed should, therefore, be introduced into the column as a vapour, which, at ambient room temperatures (between 20 °C to 30 °C during the day in Pretoria, depending on the season), will be superheated. The best column configuration for the scenario will be to introduce the feed to the bottom of the column, under the bottom-most packed section. This mode of operation is analogous to an enriching-only column, as illustrated by the McCabe-Thiele diagrams in Figure 22 for the three binary systems. Since heat will be introduced into the system by the superheated vapour feed, the reboiler should be run at a low temperature to prevent additional boilup. Once most of the TFE has been removed from the system, the mode of operation can be switched over to batch distillation, to separate the HFP-OFCB mixture that has accumulated in the reboiler.

Running the column in continuous-enriching mode has the advantage of producing a fairly pure distillate product. This, however, comes with the price of a high reflux rate requirement (between 3.4 and 5 for the systems in Figure 22), which, in turn, imposes high heat duty requirements on the condenser. Additionally, this mode of operation leads to a lower theoretical fractional recovery for TFE. Similarly, the fractional recovery for

batch distillation is also lower than that for conventional, continuous distillation.

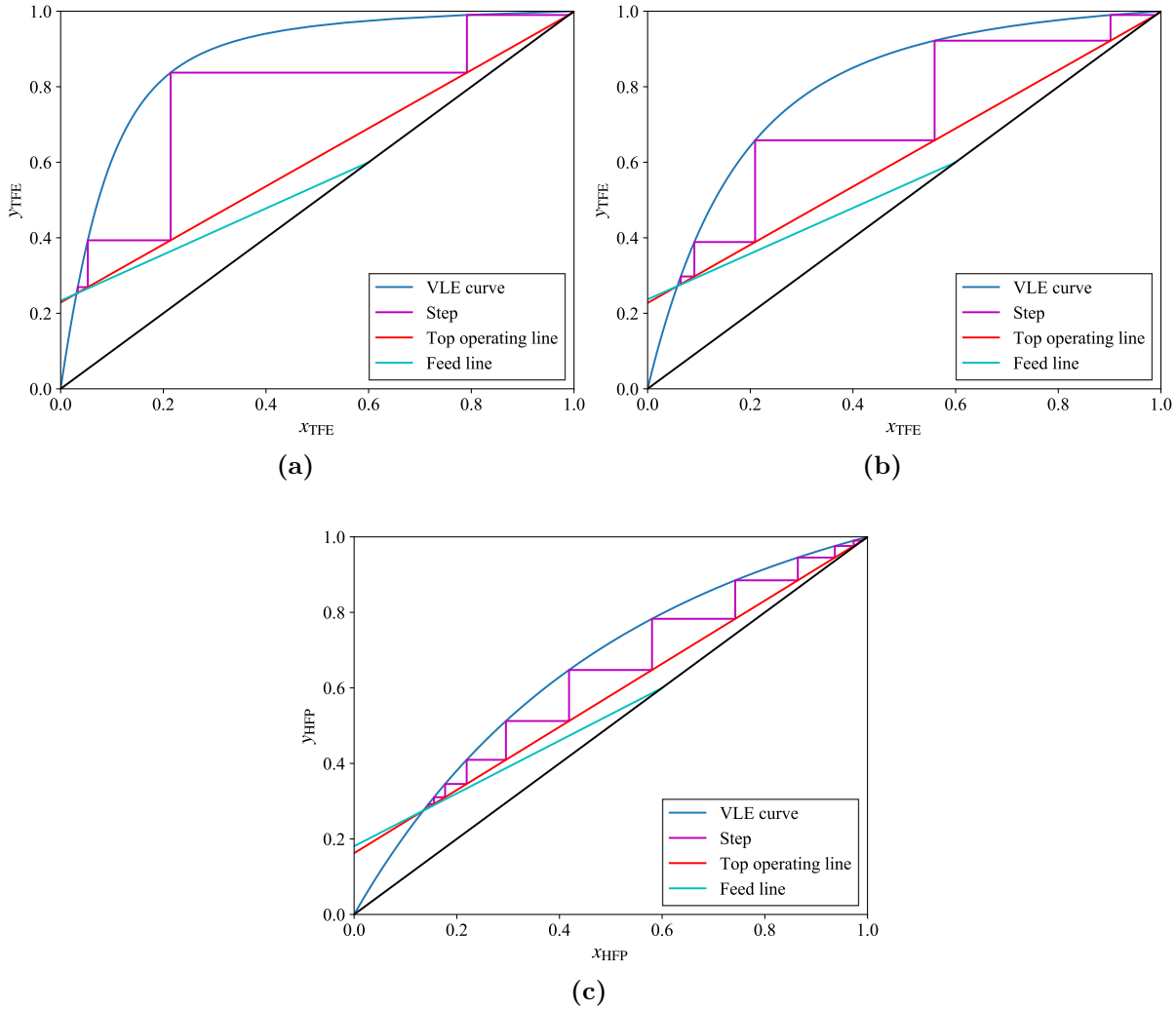

Figure 22: McCabe-Thiele diagrams for the TFE-OFCB (a), TFE-HFP (b) and HFP-OFCB (c) binary systems

3.3 Equilibrium-Based Dynamic Model

Both the equilibrium and rate-based modelling approaches will be employed to create simulations of the laboratory column, to generate a comparison between the speed and accuracy of these models. The equilibrium-based dynamic simulation was put together using the building blocks described in Section 2.2.2 and Sections 2.2.6 to 2.2.9. These building blocks were used to derive a model, specific to the laboratory column, by breaking up the problem into the following elements:

- The reboiler;
- The feed (bottom-most) packed section, which, in contrast to the convention mentioned in Section 2.2.2, will be labelled as section 1;

- Packed sections 2 to 4;
- Packed section 5;
- The condenser and, finally;
- The reflux-line.

Furthermore, the following assumptions were made in the derivation of the equilibrium-based model:

- Each packed section height is equivalent to one equilibrium stage;
- The vapour and liquid streams leaving a packed section are in thermodynamic equilibrium;
- The vapour hold-ups on the packed sections are negligible;
- The operating pressure is well controlled and remains constant;
- The pressure drop over the packed sections are insignificant, due to the low internal flow rates (this will be tested).

This section will focus on the main elements mentioned above, as well as on the algorithm used to perform the main simulation integration, while the supporting modelling equations will be dealt with in Section 3.5. The main equilibrium-based dynamic model can be summarised as follows:

Reboiler

$$\frac{d\left(M_{reb}^{L}x_{i,reb}\right)}{dt} = x_{i,1}L_1 - y_{i,reb}V_{reb}$$
$$\frac{d\left(M_{reb}^{L}h_{reb}\right)}{dt} = L_1h_1 + Q_{reb} - V_{reb}H_{reb}$$
$$M_{reb}^{L} = \sum M_{reb}^{L}x_{i,reb}$$
$$x_{i,reb} = \frac{M_{reb}^{L}x_{i,reb}}{M_{reb}^{L}},\ y_{i,reb} = K_{i,reb}x_{i,reb}$$
$$h_{reb} = \frac{M_{reb}^{L}h_{reb}}{M_{reb}^{L}},\ H_{reb} = H(T_{reb}, y_{i,reb})$$
$$T_{reb} = T(h_{reb}, x_{i,reb})$$
$$K_{i,reb} = K(P, T_{reb}, x_{i,reb}, y_{i,reb})$$

Feed packed section

$$\frac{d\left(M_1^L x_{i,1}\right)}{dt} = z_i F + y_{i,reb} V_{reb} + x_{i,2} L_2 - y_{i,1} V_1 - x_{i,1} L_1$$
$$\frac{d\left(M_1^L h_1\right)}{dt} = F H_F + V_{reb} H_{reb} + L_2 h_2 - V_1 H_1 - L_1 h_1$$
$$M_1^L = \sum M_1^L x_{i,1}$$
$$x_{i,1} = \frac{M_1^L x_{i,1}}{M_1^L},\ y_{i,1} = K_{i,1} x_{i,1}$$
$$h_1 = \frac{M_1^L h_1}{M_1^L},\ H_1 = H(T_1, y_{i,1})$$
$$\Delta P_1 = \Delta P_1(P, T_1, L_1, V_1, x_{i,1}, y_{i,1})$$
$$T_1 = T(h_1, x_{i,1})$$
$$K_{i,1} = K(P, T_1, x_{i,1}, y_{i,1})$$

Packed sections n = 2 to n = 4

$$\frac{d\left(M_n^L x_{i,n}\right)}{dt} = y_{i,n-1} V_{n-1} + x_{i,n+1} L_{n+1} - y_{i,n} V_n - x_{i,n} L_n$$
$$\frac{d\left(M_n^L h_n\right)}{dt} = V_{n-1} H_{n-1} + L_{n+1} h_{n+1} - V_n H_n - L_n h_n$$
$$M_n^L = \sum M_n^L x_{i,n}$$
$$x_{i,n} = \frac{M_n^L x_{i,n}}{M_n^L},\ y_{i,n} = K_{i,n} x_{i,n}$$
$$h_n = \frac{M_n^L h_n}{M_n^L},\ H_n = H(T_n, y_{i,n})$$
$$\Delta P_n = \Delta P_n(P, T_n, L_n, V_n, x_{i,n}, y_{i,n})$$
$$T_n = T(h_n, x_{i,n})$$
$$K_{i,n} = K(P, T_n, x_{i,n}, y_{i,n})$$

Packed section 5

$$\frac{d\left(M_5^L x_{i,5}\right)}{dt} = y_{i,4}V_4 + x_{i,refl}L_{refl} - y_{i,5}V_5 - x_{i,5}L_5$$
$$\frac{d\left(M_5^L h_5\right)}{dt} = V_4H_4 + L_{refl}h_{refl} - V_5H_5 - L_5h_5$$
$$M_5^L = \sum M_5^L x_{i,5}$$
$$x_{i,5} = \frac{M_5^L x_{i,5}}{M_5^L},\ y_{i,5} = K_{i,5}x_{i,5}$$
$$h_5 = \frac{M_5^L h_5}{M_5^L},\ H_5 = H(T_5, y_{i,5})$$
$$\Delta P_5 = \Delta P_5(P, T_5, L_5, V_5, x_{i,5}, y_{i,5})$$
$$T_5 = T(h_5, x_{i,5})$$
$$K_{i,5} = K(P, T_5, x_{i,5}, y_{i,5})$$

Condenser

$$L_{cond}\left(h_{cond} - H_5\right) = Q_{cond}$$
$$D = V_5 - L_{cond}$$
$$x_{i,cond} = y_{i,D} = y_{i,5}$$
$$T_{cond} = T(P, x_{i,cond})$$

Reflux line

$$\frac{d\left(M_{refl}^L x_{i,refl}\right)}{dt} = x_{i,cond}L_{cond} - x_{i,refl}L_{refl}$$
$$\frac{d\left(M_{refl}^L h_{refl}\right)}{dt} = L_{cond}h_{cond} - L_{refl}h_{refl}$$
$$M_{refl}^L = \sum M_{refl}^L x_{i,refl}$$
$$x_{i,refl} = \frac{M_{refl}^L x_{i,refl}}{M_{refl}^L}$$
$$T_{refl} = T(h_{refl}, x_{i,refl})$$

Omitted from the list of equations above, include the thermodynamic modelling equations, the heat duty models for the reboiler and condenser, the packing pressure drop model and the reflux and packed section hold-up outflow models. References to these models are presented in Table 23. The next step in this modelling exercise is to de-

termine whether the system has been fully defined by performing a degrees of freedom (DOF) analysis, which is represented in Table 24.

Table 23: Reference to supporting models used by the equilibrium-based dynamic model

Supporting Model Description	Section No.
Physical properties	3.5.1
Condenser heat duty	3.5.2
Enthalpies	3.5.3
VLE model	3.5.4
Packed section hold-up outflow	3.5.6
Pressure drop model	3.5.7
Reboiler heat duty	3.5.8
Reflux line hold-up outflow	3.5.9

Table 24: Simplified degree of freedom analysis for the equilibrium based dynamic model

Variable	Amount	Equation	Amount
$M_N^L x_{i,N}$[a]	3×7	Component mass balances	3×7
$M_N^L h_{i,N}$	7	Energy balances	7
M_N^L	7	Component mass summations	7
h_N	7	Calculated from energy balances and M_N^L	7
$x_{i,N}$	3×7	Calculations from mass balances and M_N^L	3×7
$y_{i,reb}$, all $y_{i,n}$	3×6	VLE calculations (produces $K_{i,reb}$, $K_{i,n}$, T_{reb}^*, T_i^*)	4×6
ΔP_n	5	Pressure drop model	5
T_N	8	Calculated from liquid enthalpies	8
H_{reb}, all H_n	6	Calculated from T_{reb}, T_n	6
Q_{cond}, L_c	2	Condenser model	2
Q_{reb}	1	Reboiler model	1
L_n	5	Packed section hold-up outflow model	5
L_{refl}	1	Reflux hold-up outflow model	1
V_n, V_{reb}	6	No dedicated equation for V_n, V_{reb}	0
Total	115	Total	115

[a] N represents a position ranging from the reboiler to the reflux line

Marked in the second last row of Table 24, is the fact that there is no dedicated equation to calculate V_n, even though the system is fully defined. This causes the system to have an index problem - an occurrence that can make a system of differential-algebraic equations (DAE's) difficult to solve. However, a simple solution to solve this particular problem is to use the VLE model in a bubble point calculation to generate temperature values for each packed section, along with the vapour compositions (Skogestad, 1993). The differential energy balance for the packed section is then turned into an algebraic equation, by first expanding the differential side of the equation using the product rule,

as shown in Equation 189

$$M_n^L \frac{dh_n}{dt} + h_n \frac{dM_n^L}{dt} = V_{n-1}H_{n-1} + L_{n+1}h_{n+1} - V_nH_n - L_nh_n \tag{189}$$

after which the total differential mass balance is substituted into dM_n/dt, simplified and rearranged to produce Equation 190

$$M_n^L \frac{dh_n}{dt} = V_{n-1}\left(H_{n-1} - h_n\right) + L_{n+1}\left(h_{n+1} - h_n\right) - V_n\left(H_n - h_n\right) \tag{190}$$

where h_n is now calculated from T_n using the enthalpy model, instead of the other way around. The gradient, dh_n/dt, is approximated by calculating the difference between the current and previous time-step h_n-values, as demonstrated in Equation 191

$$\frac{dh_n}{dt} = \frac{h_{n,k} - h_{n,k-1}}{\delta t} \tag{191}$$

with δt defining the time-step for the numerical integration. Euler's method (Equation 192) has been chosen as the integration technique for both the equilibrium and rate-based simulations, due its simplicity and robustness

$$x_{k+1} = x_k + f(x_k, t_k)\delta t \tag{192}$$

with

$$\delta t = t_{k+1} - t_k \tag{193}$$

The method derived by Equations 190 and 191 can also be used to calculate the vapour coming from the reboiler

$$M_{reb}^L \frac{dh_{reb}}{dt} = L_1\left(h_1 - h_{reb}\right) + V_{reb}\left(h_{reb} - H_{reb}\right) + Q_{reb} \tag{194}$$

Simulation programs that perform the numerical integration for both the equilibrium and rate-based modelling strategies, were written in the Python (v3.7) programming language. The integration iteration takes place within a for-loop that runs for a specified amount of time-steps. The supporting models, which are discussed in the subsequent sections, as referenced in Table 23, were programmed into functions that evaluate the particular models and return the resulting parameters, given the required inputs. These functions are called inside the integration for-loop to provide the parameters required by the continuity equations. Figure 23 depicts the algorithm used in the simulation program.

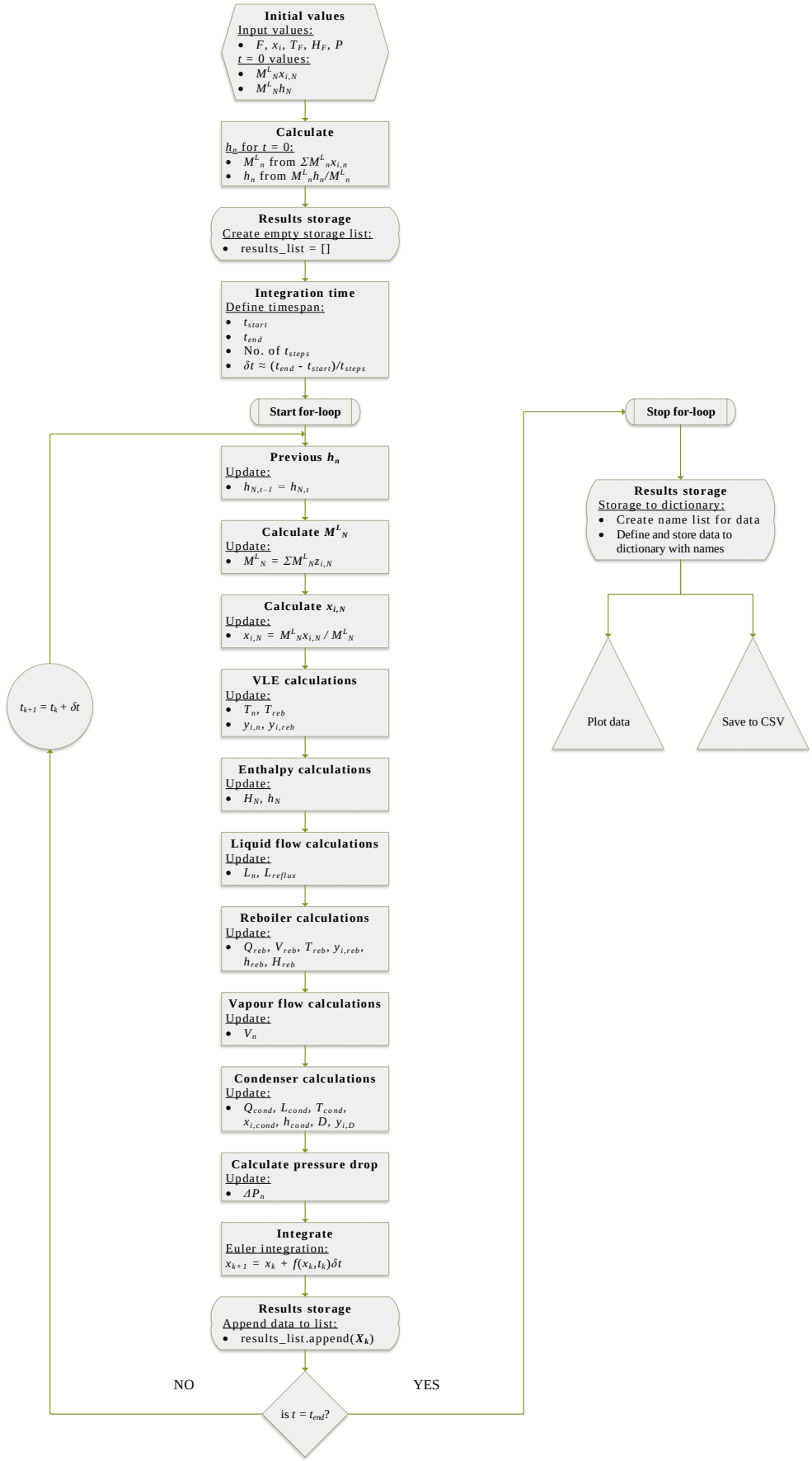

Figure 23: Algorithm for the equilibrium-based dynamic simulation

3.4 Rate-Based Dynamic Model

A summary of the rate-based dynamic model is presented below. Only the modelling equations for the packed sections are presented, as the models for the reboiler, condenser and reflux line stay the same as for the equilibrium-based model in Section 3.3. The assumption of negligible vapour hold-up has been carried over to the rate model, to avoid the index problem and to allow for the direct calculation of the vapour flows, compositions and temperatures. All the other equilibrium-based modelling assumptions were also made in deriving the rate-based model, except the assumption that the vapour and liquid streams leaving the packed sections are in thermodynamic equilibrium.

As with the equilibrium model, only the main simulation equations have been presented, with references to the auxiliary models given in Table 25. A degree of freedom analysis is shown in Table 26. Furthermore, the same method to create the equilibrium simulation was also employed to create rate-based simulations. There are, however, minor differences in the algorithm and an adjusted logic-flow is presented in Figure 24.

Feed packed section

$$\frac{d\left(M_1^L x_{i,1}\right)}{dt} = x_{i,2}L_2 - x_{i,1}L_1 + \mathcal{N}_{i,1}$$
$$\frac{d\left(M_1^L h_1\right)}{dt} = L_2 h_2 - L_1 h_1 + \mathcal{E}_{i,1}$$
$$0 = z_i F + y_{i,reb}V_{reb} - y_{i,1}V_1 - \mathcal{N}_{i,1}$$
$$0 = FH_F + V_{reb}H_{reb} - V_1 H_1 - \mathcal{E}_{i,1}$$
$$M_1^L = \sum M_1^L x_{i,1}$$
$$x_{i,1} = \frac{M_1^L x_{i,1}}{M_1^L}$$
$$h_1 = \frac{M_1^L h_1}{M_1^L}$$
$$\mathcal{N}_{i,1}, \mathcal{E}_{i,1} = \mathcal{N}_{i,1}, \mathcal{E}_{i,1}\left(\text{Maxwell-Stefan model}, T_1^L, T_1^V, L_1, V_1, x_{i,1}, y_{i,1}, P\right)$$
$$\Delta P_1 = \Delta P_1(P, T_1^L, T_1^V, L_1, V_1, x_{i,1}, y_{i,1})$$
$$T_1^L = T(h_1, x_{i,1})$$
$$T_1^V = T(H_1, y_{i,1})$$

Packed sections n = 2 to n = 4

$$\frac{d\left(M_n^L x_{i,n}\right)}{dt} = x_{i,n+1}L_{n+1} - x_{i,n}L_n + \mathcal{N}_{i,n}$$
$$\frac{d\left(M_n^L h_n\right)}{dt} = L_{n+1}h_{n+1} - L_n h_n + \mathcal{E}_{i,n}$$
$$0 = y_{i,n-1}V_{n-1} - y_{i,n}V_n - \mathcal{N}_{i,n}$$
$$0 = V_{n-1}H_{n-1} - V_n H_n - \mathcal{E}_{i,n}$$
$$M_n^L = \sum M_n^L x_{i,n}$$
$$x_{i,n} = \frac{M_n^L x_{i,n}}{M_n^L}$$
$$h_n = \frac{M_n^L h_n}{M_n^L}$$
$$\mathcal{N}_{i,n}, \mathcal{E}_{i,n} = \mathcal{N}_{i,n}, \mathcal{E}_{i,n}\left(\text{Maxwell-Stefan model}, T_n^L, T_n^V, L_n, V_n, x_{i,n}, y_{i,n}, P\right)$$
$$\Delta P_n = \Delta P_n(P, T_n^L, T_n^V, L_n, V_n, x_{i,n}, y_{i,n})$$
$$T_n^L = T(h_n, x_{i,n})$$
$$T_n^V = T(H_n, y_{i,n})$$

Packed section 5

$$\frac{d\left(M_5^L x_{i,5}\right)}{dt} = x_{i,refl}L_{refl} - x_{i,5}L_5 + \mathcal{N}_{i,5}$$
$$\frac{d\left(M_5^L h_5\right)}{dt} = L_{refl}h_{refl} - L_5 h_5 + \mathcal{E}_{i,5}$$
$$0 = y_{i,4}V_4 - y_{i,5}V_5 - \mathcal{N}_{i,5}$$
$$0 = V_4 H_4 - V_5 H_5 - \mathcal{E}_{i,5}$$
$$M_5^L = \sum M_5^L x_{i,5}$$
$$x_{i,5} = \frac{M_5^L x_{i,5}}{M_5^L}$$
$$h_5 = \frac{M_5^L h_5}{M_5^L}$$
$$\mathcal{N}_{i,5}, \mathcal{E}_{i,5} = \mathcal{N}_{i,5}, \mathcal{E}_{i,5}\left(\text{Maxwell-Stefan model}, T_5^L, T_5^V, L_5, V_5, x_{i,5}, y_{i,5}, P\right)$$
$$\Delta P_5 = \Delta P_5(P_{5,ave}, T_5^L, T_5^V, L_5, V_5, x_{i,5}, y_{i,5})$$
$$T_5^L = T(h_5, x_{i,5})$$
$$T_5^V = T(H_5, y_{i,5})$$

Table 25: Reference to supporting models used by the rate-based dynamic model

Supporting Model Description	Section No.
Physical properties	3.5.1
Condenser heat duty	3.5.2
Enthalpies	3.5.3
Integrated MS-Model, vapour flow & VLE	3.5.5
Packed section hold-up outflow	3.5.6
Pressure drop model	3.5.7
Reboiler heat duty	3.5.8
Reflux line hold-up outflow	3.5.9

Table 26: Simplified degree of freedom analysis for the rate-based model

Variable	Amount	Equation	Amount
$M_n^L x_{i,n}$	3x5	Liquid rate component balances	3x5
$M_\beta^L x_{i,\beta}$[a]	3x2	β-component balances	3x2
$M_n^L h_n$	5	Liquid rate energy balances	5
$M_\beta^L h_\beta$	2	β-energy balances	2
M_n^L	5	Liquid component mass summations	5
M_β^L	2	β-component mass summations	2
h_n, h_β	7	Calculated from energy balances and M_n^L, M_β^L	7
$x_{i,n}$, $z_{i,\beta}$	3x7	Calculated from mass balances and M_n^L, M_β^L	3x7
$y_{i,n}$, V_n	4x5	Vapour rate component balances	4x5
$y_{i,reb}$, T_{reb}^*	4	VLE calculations	4
ΔP_n	5	Pressure drop model	5
T_n^L, T_n^V, T_β	12	Calculated from liquid, vapour enthalpies	12
H_n	5	Calculated from rate energy balances	5
H_{reb}	1	Calculated from T_{reb}	1
$Qcond$, L_c	2	Condenser model	2
Q_{reb}, V_{reb}	2	Reboiler model	2
L_n	5	Packed section hold-up outflow model	5
L_{refl}	1	Reflux hold-up outflow model	1
Total	120	Total	120

[a] β represents the position of either the reboiler or the reflux line

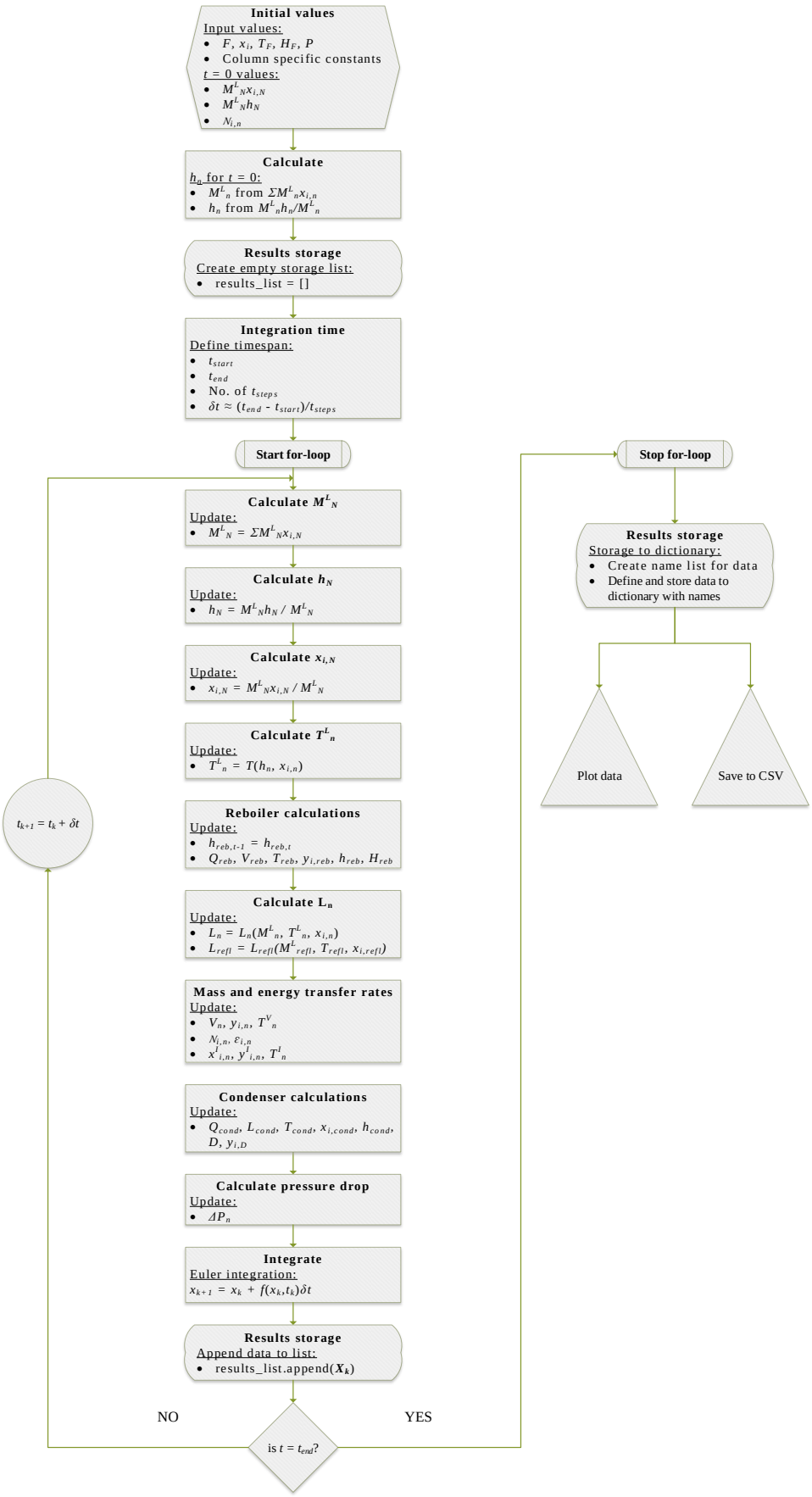

Figure 24: Algorithm for the rate-based dynamic simulation

3.5 Supporting Simulation Functions

The supporting simulation equations were programmed into functions, that can easily be called by other functions or the main simulation programs, to deliver the desired variables, given the required inputs. All variables are returned in SI units, with the required unit conversions performed inside the functions.

3.5.1 Physical Properties

The following summaries describe the internal workings of the physical property functions:

The molar mass, critical properties and acentric factor functions require a "molecule ID" string input, that is either `'TFE'`, `'HFP'` or `'OFCB'`. If-statements then relate the correct property value to the input and the function returns that value as the output.

The compressibility factor function requires temperature (in K) pressure (in kPa) and a molecule ID as inputs. The function then first calls the critical temperature and pressure and the acentric factor of that molecule and then calculates the reduced temperature and pressure. Next, a solve-function is defined to produce $z^{(0)}$ from Equations 160 to 163. This process is repeated in a second solve-function to produce $z^{(h)}$. Finally, the compressibility factor, z, is calculated from Equation 159 and returned as the output.

The pure vapour density function takes temperature, pressure and a molecule ID as inputs. The compressibility factor and molar mass functions are then called to produce the corresponding values, after which the vapour density for that compound is calculated using Equation 158 and returned.

The pure liquid density function only requires the temperature and molecule ID of the compound as inputs. If-statements relate the compound to the relevant coefficients in Table 7. The density is then calculated using Equation 157 and returned.

Mixed vapour and liquid density functions were programmed using the same algorithm, however, the inputs have some differences. The vapour mixed density function requires temperature, pressure and vapour mole fractions, while the liquid mixed density function requires temperature and the liquid mole fractions, as inputs. Inside the functions, the molar mass functions and the pure vapour or liquid density functions are called. The molar masses are then used to convert the mole fractions into mass fractions, after which Equation 164 is used to calculate the mixed densities.

Both the vapour and liquid viscosity functions require temperature and a molecule ID as inputs. As before, if-statements relate the compound's ID to its equation specific coefficients in Table 19 for the liquid phase or Table 20 for the vapour phase. Finally, the viscosities are calculated by either Equation 184 (liquid phase) or Equation 186 (vapour phase) and converted to SI units, before being returned.

The mixed liquid viscosity input requirements include the temperature and the liquid mole fractions. Inside the function, the pure component viscosities are calculated using the liquid viscosity function, after which the mixing rule of Equation 185 is applied to produce the mixed vapour viscosity.

Mixed vapour viscosity calculations are a bit more complicated. From the temperature input, the pure vapour viscosity values are calculated using the predefined function. This is followed by calling the molar mass function. Next, the interaction parameter, Q_{ij}, for each binary pair, is calculated using Equation 188 and the vapour mole fraction inputs. To prevent zero division in Equation 187, several if-statements are used to adjust the mixing parameters in the case of zero mole fractions. The first if-statements check for the presence of a component vapour mole fraction greater than or equal to one and sets the mixed viscosity value equal to that component's value. The next set of if-statements searches for a mole fraction smaller than or equal to zero, before calculating the mixture value based on the remaining two components. Finally, if the aforementioned if-statements are passed off as negative, the mixed viscosity is calculated based on the ternary system.

Pure component surface tension values are calculated using the same algorithm presented to calculate pure liquid densities and pure vapour and liquid viscosities. The required inputs are the temperature and a molecule ID. Surface tension values are calculated by Equation 172, using the coefficients listed in Table 12.

The mixed surface tension function requires the temperature and liquid mole fractions as inputs. First, the pure surface tension, the molar mass and the pure liquid density functions are called to produce the corresponding values for each component. The pure liquid densities are then converted from mass-based to mole-based units and Equation 164 is used to calculate the mole-based density for the mixture. Finally, Equation 173 is employed to calculate the surface tension mixture value.

Pure vapour and liquid heat capacity calculations both require upper and lower temperature limits and a molecule ID as inputs. Average heat capacity ($\overline{C_P}$) values are calculated from the integrated polynomial of Equation 169 (coefficients are found in Tables 9 and 10), between the upper and lower temperature limits, divided by the difference of the temperature limits.

Mixture vapour and liquid capacities are calculated by a simple algorithm. Upper and lower temperature limits and vapour or liquid mole fractions are required as inputs. Inside the functions, the average heat capacities are calculated using the applicable pre-defined functions. Equation 170 is then used to calculate the mixture average heat capacity.

Heats of vapourisation calculations follow the same methods that have reoccurred in this section. The pure heat of vapourisation functions take temperature and a molecule ID as inputs and calculates the heat of vapourisation using Equation 171 and the coefficients in Table 11. The mixed heat of vapourisation function requires temperature and mole fractions as inputs. It calculates the pure heat of vapourisation values using the aforementioned function and applies the same mixing rule used for the heat capacities.

Vapour and liquid thermal conductivities for pure components require temperature and a molecule ID as inputs. Equation 174 is used to calculate the thermal conductivities for both phases, using the coefficients in Tables 13 and 14 for the liquid and vapour phases, respectively.

The mixed vapour thermal conductivity function requires the standard input of temperature and vapour mole fractions. The calculations start with evaluating the pure vapour thermal conductivities, pure vapour viscosities and by calling the molar masses from the previously defined functions. Next, each component's saturation temperature at 1 atm is evaluated using one of the VLE functions (see Section 3.5.4). Equations 177, 178 and 176 are applied before calculating the mixture value using Equation 175.

Mixed liquid thermal conductivity calculations also start with the standard input of temperature and liquid mole fractions. Next, the pure component liquid thermal conductivity, molar mass and pure liquid density functions are called. The liquid density and molar mass values are used to calculate molar volumes, after which the binary thermal conductivity parameters are defined using Equation 181. Finally, the ϕ_i-parameters are calculated using Equation 180, before the mixture liquid thermal conductivity value is calculated (Equation 179) and returned.

3.5.2 Condenser Function

The main goal of the condenser function is to calculate the condensate rate. To achieve this, the following simplifying assumptions have been made:

- The condensate leaves the condenser as a saturated liquid;
- The outer walls of the condenser tubes are at the same temperature as the cooling fluid.

The second assumption is justified by the fact that $\dot{m}_{utility} \ggg \dot{m}_{condensate}$. For comparison, the Julabo cooling unit is rated to deliver a flow rate between 11 L·min^{-1} and 16 L·min^{-1} (0.148 kg·s^{-1} to 0.216 kg·s^{-1} for methanol at 0 °C) while the gas feed flow meter has a maximum flow rating of 500 sccm (standard cubic centimetre per minute, which translates to 3.77×10^{-5} kg·s^{-1} for pure TFE at 0 °C and 101.325 kPa).

Figure 25 depicts the algorithm used to evaluate the condenser modelling equations. The equations and supporting functions used in this model include:

- Equations 122 to 130;
- Liquid and vapour density functions (described in Section 3.5.1);
- Liquid heat capacity, viscosity and thermal conductivity functions (Section 3.5.1);
- Liquid and vapour enthalpy functions (Section 3.5.3);
- VLE bubble-point calculation function (Section 3.5.4).

3.5.3 Enthalpy Functions

The vapour and liquid enthalpy calculations follow the same form as presented in Wankat (2012: 226), where a temperature of 30 °C serves as a reference point where the enthalpies are evaluated. This leads to the vapour and liquid enthalpies being described Equations 195 and 196, respectively

$$H_m = \sum y_i \overline{C_{P,i}^V} \left(T - T_{ref}\right) \tag{195}$$

$$h_m = \sum x_i \overline{C_P^L}, i \left(T - T_{ref}\right) - \sum x_i \lambda_i^V \tag{196}$$

where the heats of vapourisation (λ_i^V) are evaluated at the reference temperature. The average heat capacities were evaluated over a wide temperature range that will contain the temperature in question. This was done so that Equations 195 and 196 can be re-written to calculate temperatures explicitly from the enthalpies, *ie*, without the need for

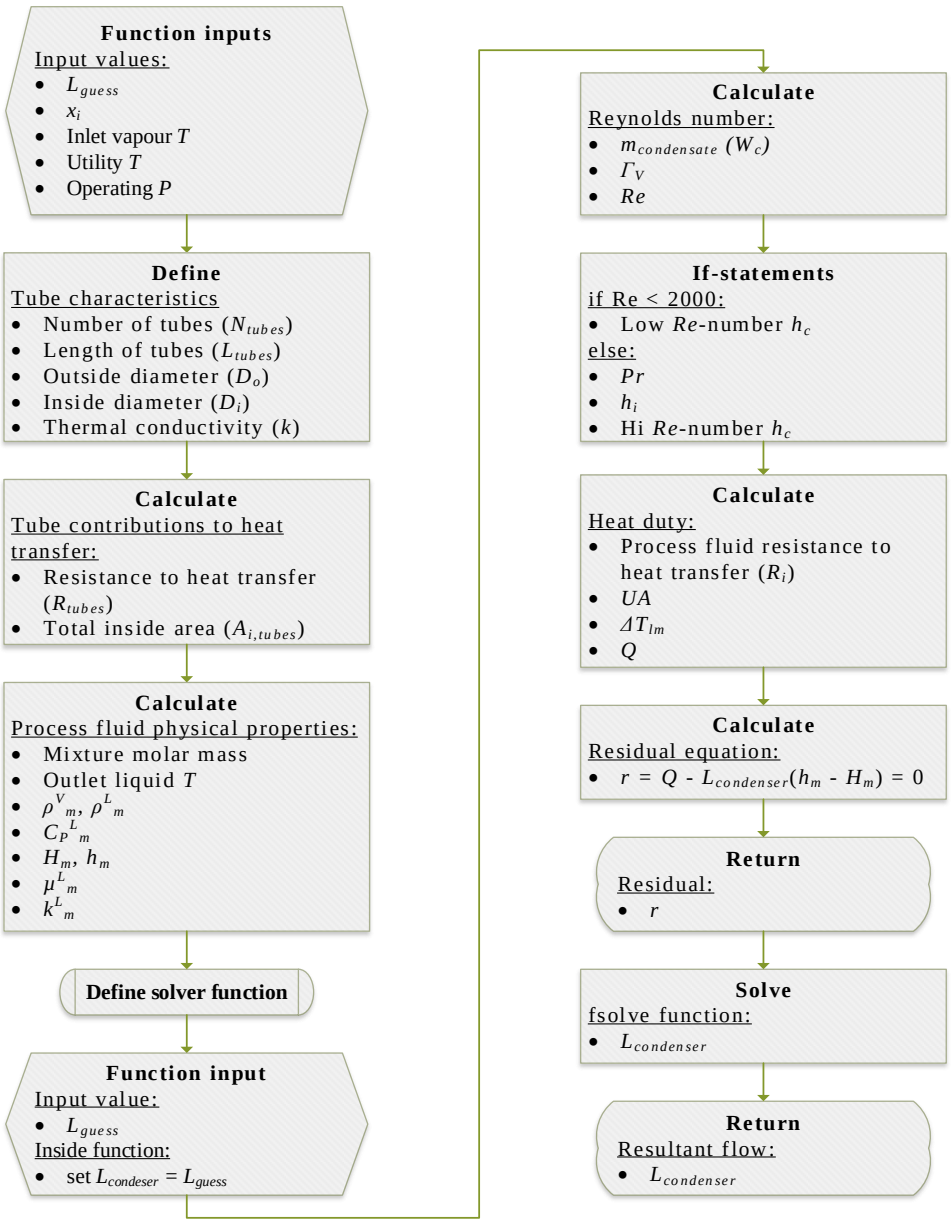

Figure 25: Condenser model algorithm

a solver function. Equations 195 and 196 can be re-written into Equations 197 and 198, respectively

$$T = T_{ref} + \frac{H_m}{\sum y_i \overline{C^V_{P,i}}} \tag{197}$$

$$T = T_{ref} + \frac{h_m + \sum x_i \lambda^V_i}{\sum x_i \overline{C^L_{P,i}}} \tag{198}$$

Four functions were therefore created for this section: two functions that require temperature and either vapour or liquid mole fractions as inputs, that deliver enthalpies from Equation 195 or 196, respectively; two functions that require the enthalpies and mole fractions as inputs and perform the opposite calculations of Equations 197 and 198.

3.5.4 VLE Functions

A number of functions were created to serve as building blocks from which variants of the complete VLE model were created. The VLE functions can be summarised as follows:

The Mathias-Copeman alpha function requires temperature and a molecule ID as inputs. The critical temperature function is then called and the reduced temperature is calculated. A set of if-statements relate the molecule ID to its Mathias-Copeman alpha function constants in Table 2, before calculating the alpha value using Equation 96.

Pure Peng-Robinson coefficients are produced by a dedicated function. The only input required is a molecule ID, which is used to call the component's critical temperature and pressure. The pure component $a(T_c)$ and $b(T_c)$-values are then calculated using Equations 88 and 89.

Two NRTL τ-value functions are used to calculate the τ_{ij} and τ_{ji}-coefficients that are required in the NRTL activity coefficient calculations. Both functions require temperature and the molecule ID's of the components in the binary pair, in descending order of relative volatility. Inside the function, if-statements relate the molecule IDs to the binary pair constants in Table 4, that are then applied in Equation 104 to yield the τ_{ij} and τ_{ji}-values.

The binary k_{ij}-function works in the same way as the τ-functions. The function takes temperature and two molecule IDs as inputs. If-statements match the constants in Table 3 and calculate k_{ij} using Equation 101.

Vapour pressures and saturation temperatures of pure components are calculated by two separate functions that are built around the Antoine model discussed in Section 2.2.9.7. The vapour pressure function requires a system temperature and a molecule ID as inputs. For the saturation temperature function, the system temperature input is replaced by system pressure input. Inside each function, if-statements relate the molecule ID to its applicable constants for the Antoine equation, which is then used to calculate the wanted value.

Excess Gibbs free energies for the Wong-Sandler mixing rules are calculated in a function that requires temperature and mole fractions as inputs. The function then calls the two τ-functions to calculate the τ_{ij} and τ_{ji}-values for each binary pair, after which the G_{ij} and G_{ji}-values are calculated using Equation 105. Finally, G^E is calculated using Equation 107 and returned.

Pure component molar volumes, which are required in the Φ-calculations, can be produced using the Peng-Robinson equation of state. This function requires the system pressure, temperature and a molecule ID as inputs. It then calls the Mathias-Copeman alpha-function and the pure Peng-Robinson coefficients function to produce the α, $a(T_c)$ and $b(T_c)$-values. After calculating $a(T)$ from α and $a(T_c)$, the values of A, B and z are calculated from Equations 93, 94 and 95. The lower case z is used here instead of the original upper case Z in Equation 95, as it is treated as a coefficient to the molar volume (v), that needs to be solved. Each term in Equation 92 is then labelled in the code (as C_1, C_2, C_3 and C_4) in order to serve as inputs to the *roots* root-solver function in the *numpy* Python package. Finally, the vapour and liquid phase molar volumes are filtered from the root-solver results by using the *max* and *min* Python functions.

Mixture molar volume calculations follow the same logic as the pure component calculations, with some differences. The inputs required are system pressure and temperature, as well as vapour and liquid mole fractions. Inside the function, the excess Gibbs free energy function is called, followed by the Mathias-Copeman alpha function, the Peng-Robinson pure component coefficients function and the binary k_{ij}-function. Next, the $a(T_c)$-values are calculated, after which the Wong-Sandler mixing rules of Equations 97 to 100 are applied to produce the mixture a_m and b_m-values. Finally, the values for A, B and z are calculated and the cubic roots of Equation 92 are solved and filtered to produce the mixture vapour and liquid molar volumes.

The activity coefficient function requires temperature and liquid mole fractions as inputs. Inside the function, the evaluations start by calling the τ_{ij} and τ_{ji}-functions, after which the G_{ij} and G_{ji}-values are calculated using Equation 105. Finally, Equation 108 is evaluated to produce the γ_i-values.

Pure saturated fugacities require system temperature, the vapour pressure and liquid molar volume of the pure component and a molecule ID as functional inputs. The calculations start by calling the Mathias-Copeman alpha and Peng-Robinson pure component coefficient functions. Next, $a(T)$ is calculated, followed by A, B and Z from Equations 93, 94 and 95. Finally, the saturated fugacity (ϕ^*) value is calculated using Equation 114.

Fugacity coefficient calculations for the γ-Φ VLE formulation require pressure, temperature and vapour mole fractions as inputs. The calculations start by calling the following functions: the excess Gibbs free energy function, the activity coefficient function, the Mathias-Copeman alpha and the Peng-Robinson pure component coefficient functions (from which $a(T)$ is calculated), the binary k_{ij}-function, the pure

component molar volume function (to generate pure liquid molar volumes) and the mixed molar volume function (to produce the system's vapour molar volume). The calculations that follow evaluate the partial derivatives of Equations 116 to 121 and the Wong-Sandler mixing rules of Equations 97 to 100. Finally, the $\hat{\phi}_i$-values are calculated using Equation 115, followed by the Φ-calculations from Equation 113.

The bubble-point pressure function utilises the γ-Φ VLE-formulation (Equation 112) to calculate the equilibrium pressure and vapour mole fractions, given the system temperature and liquid mole fractions. The algorithm used to calculate the required outputs is the same that was presented on the left-hand side of Figure 8.

The bubble-point temperature function is also based on the γ-Φ VLE-formulation, but requires a system pressure as one of the inputs (together with the liquid mole fractions) and delivers the temperature as an output (together with the vapour mole fractions). The algorithm used in this function is presented on the left-hand side of Figure 9.

The P-x-y diagrams for the three binary systems were generated (using the bubble-point pressure function) and plotted against the experimental data reported by Conradie (2011: 104-117), to test whether the vapour-liquid equilibrium model was put together correctly. The resulting graphs are presented in Figure 26. The model shows some deviation from the experimental data in the two systems that contain HFP, at the higher pressures. This could be because the model was originally regressed to the data by using the ϕ-ϕ VLE-method (Conradie *et al* (2015)), instead of the γ-Φ method. The ϕ-ϕ method is known to be more accurate than the γ-Φ method at high pressures, especially as a component's critical point is being approached (Perry & Green, 1999: 4-28–4-29). This will, however, never be a problem in the work presented here, as the column operating pressure will be kept below 200 kPa, ensuring that the γ-Φ VLE-method will provide acceptable accuracy.

3.5.5 Integrated Maxwell-Stefan, Vapour Flow and VLE Functions

Several functions were programmed to put the Maxwell-Stefan mass transfer model together. These functions can be grouped into minor and major functions. The minor functions possess fewer lines of code, in comparison to the major functions. The minor functions can be described as follows:

The binary diffusion coefficient function for the vapour phase requires temperature, pressure and molecule IDs for the two components, as inputs. Inside the function,

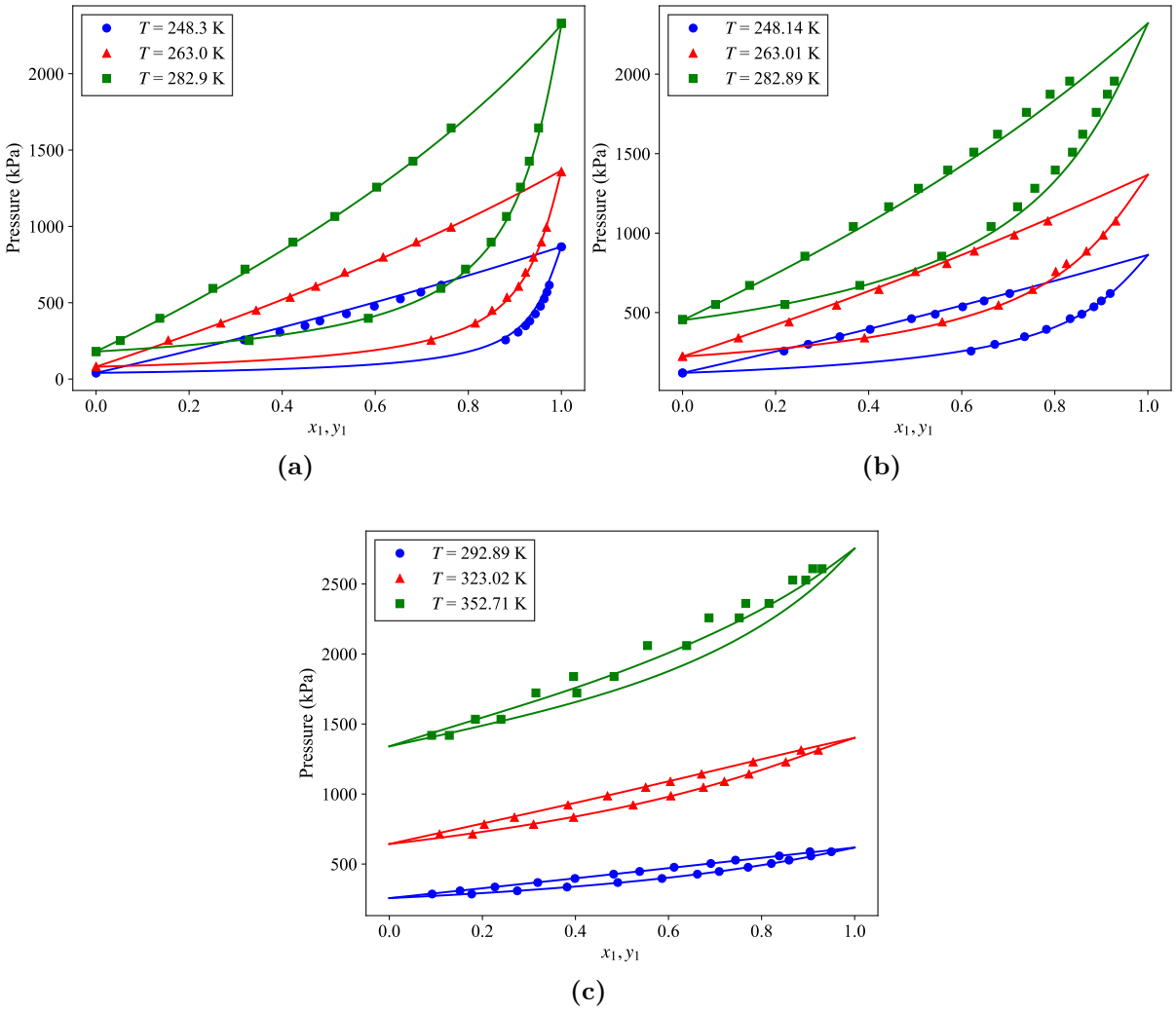

Figure 26: *P-x-y* diagrams for the (a) TFE(1)-OFCB(2), (b) TFE(1)-HFP(2) and (c) HFP(1)-OFCB(2) binary systems

if-statements check the molecule IDs and calculate the molecular diffusion volumes of the two components. The molar mass functions are then called, after which the diffusion coefficient is calculated using Equation 165.

Liquid binary diffusion coefficients require temperature, the liquid mole fractions of the two components and their molecule IDs as inputs. The first operation in the function is the normalisation of the liquid mole fractions (to take them from a ternary to a binary basis). Next, the molar mass, saturation temperature, pure liquid density, pure and mixed liquid viscosity (which are converted to units of cP) and the τ_{ij} and τ_{ji}-functions are evaluated. The liquid densities and molar masses are then used to calculate liquid molar volumes, which are converted to units of $cm^3 \cdot mol^{-1}$ before being used to calculate the infinite dilution binary diffusion coefficients (Equation 166). Finally, the infinite dilution diffusion coefficients are adjusted to the actual diffusion coefficients by first calculating the G_{ij} and G_{ji}-values, followed by the α-value defined by Equation 168, before calculating D_{ij}^{L}

from Equation 167.

The effective interfacial area function is built around Equation 64. The required inputs include liquid and vapour temperatures, system pressure and liquid and vapour molar flows and fractions. Inside the function, the mixed vapour and liquid densities, viscosities, molar masses and mixed liquid surface tension are evaluated. Next, the vapour and liquid superficial velocities are calculated, followed by the calculation of a_e, which is then returned as the output.

Binary mass transfer coefficient calculations for the vapour and liquid phases follow the same algorithm, with a few differences in the functional inputs. Both functions require the mole fractions and molecule IDs of the binary pair, as well as the specific phase molar flow rates and temperatures. In addition to these values, the vapour mass transfer coefficient function requires pressure, while the liquid phase function requires the effective interfacial area, as inputs. Inside the function, the mole fractions are normalised, followed by the evaluations of the molar mass, mixed density, mixed viscosity and binary diffusion coefficient functions. The superficial vapour and liquid velocities are then calculated in the respective functions, followed by the mass transfer coefficients (Equations 62 and 63).

The heat transfer coefficient functions were treated in the same way as the binary mass transfer coefficient functions. The common inputs include the mole fractions and molecule IDs of the two components in the binary pair and the phase-specific molar flows, heat capacities and temperatures. Additional inputs include the system pressure for the vapour phase function and the effective interfacial area for the liquid phase function. After the mole fractions have been normalised, the molar mass, binary diffusion coefficient, binary mass transfer coefficient, mixed thermal conductivity and mixed density functions are called. The Lewis numbers are then calculated, followed by the heat transfer coefficients.

The heat flux function is built around the vapour-phase heat flux equations (Equations 74 and 76). The inputs required include the vapour and liquid temperatures, mole fractions and molar flows, as well as the system pressure, the component molar fluxes across the two-phase interface and the interface temperature. Inside the function, pure component average vapour heat capacities are calculated, which are, in turn, used to calculate binary mixture heat capacities. This is done by applying the mixing rules of Equation 170, but with vapour mole fractions that are normalised to a binary pair basis. These values are required as inputs to the heat transfer coefficient functions, which are based on binary pairs due to their dependence on the binary mass transfer and diffusion coefficients. The binary heat transfer coefficients are then turned into effective heat transfer coefficients, in the same fashion

that effective diffusion coefficients can be calculated, as illustrated by Equation 199. The final processing of the heat transfer coefficients is to calculate the mixture heat transfer coefficient from the effective heat transfer coefficient values. Next, the vapour enthalpies are calculated between the vapour and interface temperatures, which is followed by calculating the effective interfacial area and converting its units from $m^2 \cdot m^{-3}$ to m^2. The final calculation is that of the heat flux.

$$h^V_{i,eff} = \frac{(1 - y_i)}{\sum_{k=1}^{c} (y_k / h_{ik})} \tag{199}$$

The first major function aims to calculate the vapour and liquid mass fluxes from the matrix operations reviewed in Section 2.2.5. The bulk fluid conditions were chosen as the reference points for the diffusional paths. The model was also simplified by assuming that each corrective factor matrix is equal to the identity matrix. This assumption is regularly made in distillation modelling (for example by J Peng, Edgar & Eldridge (2003) and Bonilla *et al* (2012)), especially after Powers *et al* (1988) found that the corrective flux matrix usually approximates the identity matrix, due to low mass transfer rates associated with distillation. The algorithm used in this function is shown in Figure 27.

The final function in this section is designed to solve the Maxwell-Stefan model. The algorithm for this function is depicted in Figure 28. The vapour phase flow, mole fractions and temperature calculations were made part of this function, as they are both required by and dependent on the mass transfer rates. Furthermore, the *fsolve*-solver function from the *scipy* Python package, was used to solve the system of equations.

3.5.6 Packed Section Liquid Outflow

The packed section liquid outflow function is made up of straightforward calculations. Function inputs consist of temperature, liquid molar hold-up and the liquid mole fractions. The mixed liquid density function is then called and the mixture's molar mass is calculated. Next, the molar volume of the mixture is calculated from the density and molar mass, the volume of the section of the column occupied by a height of packing is calculated and the liquid hold-up is converted to units of $kmol \cdot m^{-3}$ of packing. Finally, the liquid outflow is calculated using Equation 156 and returned.

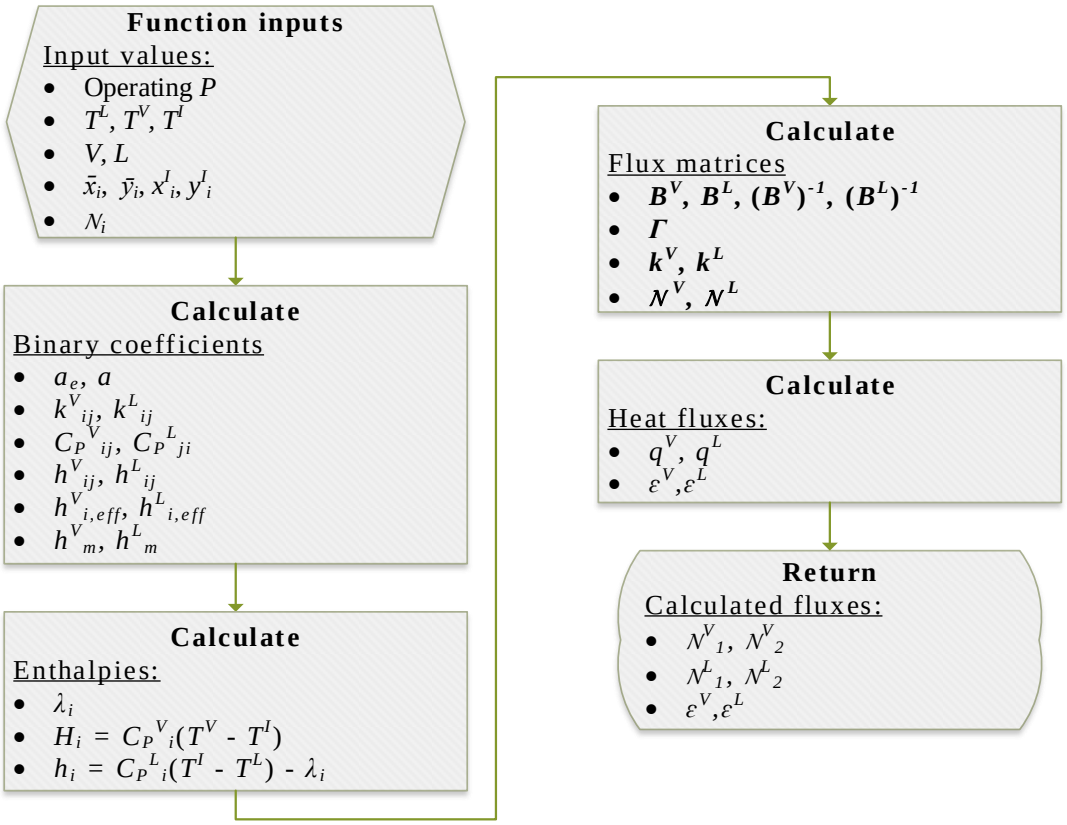

Figure 27: Maxwell-Stefan model calculations

3.5.7 Pressure Drop Model

This function utilises the Robbins model to calculate the pressure drop over a packed section. This model requires a packing-specific constant, known as the dry packing factor (F_{pd}), which will have to be fitted to experimental pressure drop data since a non-commercial packing is used in the laboratory column. A dry packing factor value of 1600 has been specified for the interim.

The algorithm used in this function is depicted in Figure 29. The modelling equations and supporting functions used in the algorithm include:

- Equations 147 to 154
- Vapour and liquid density functions;
- Liquid viscosity function;
- Molar mass function.

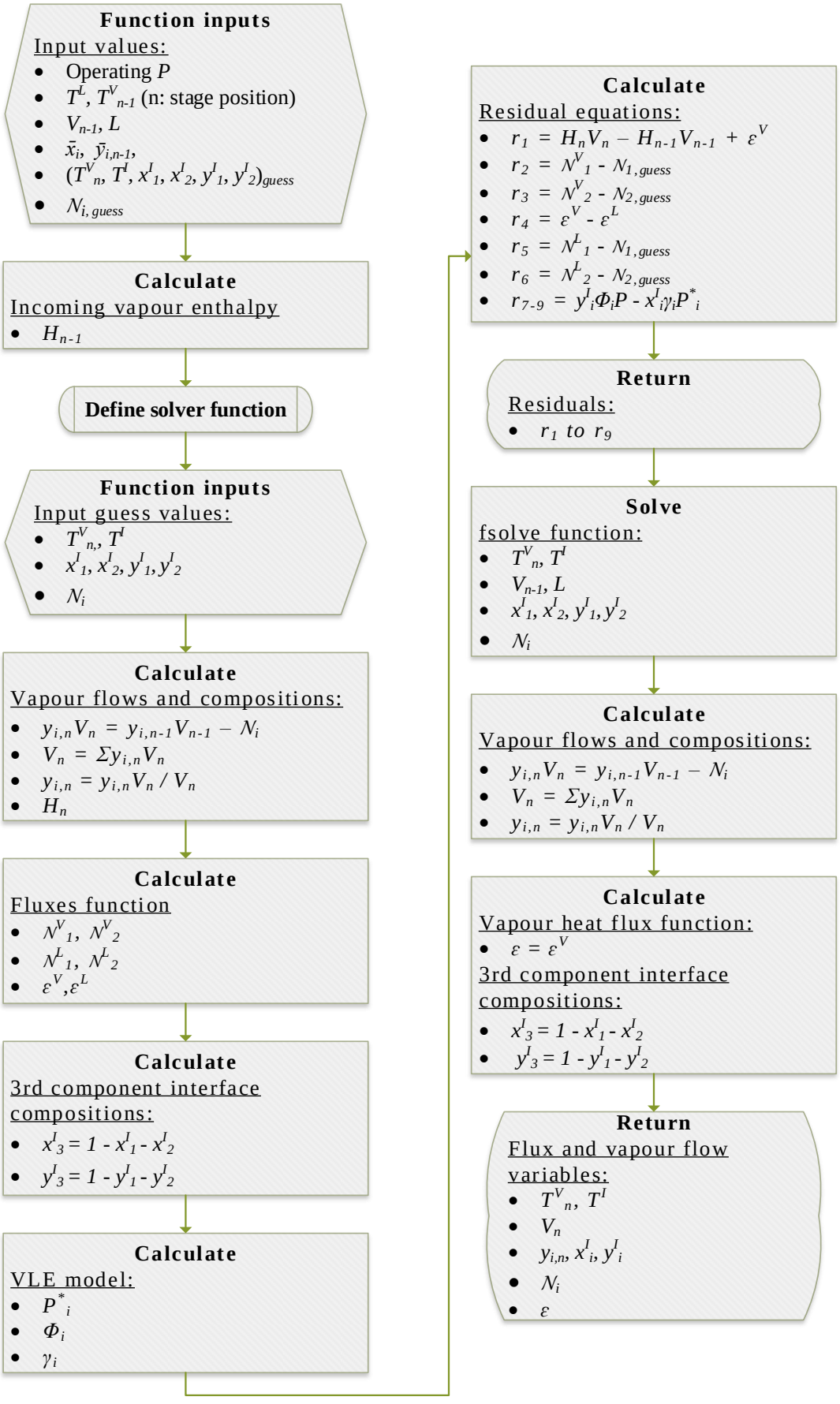

Figure 28: Integrated Maxwell-Stefan, VLE and vapour flow function algorithm

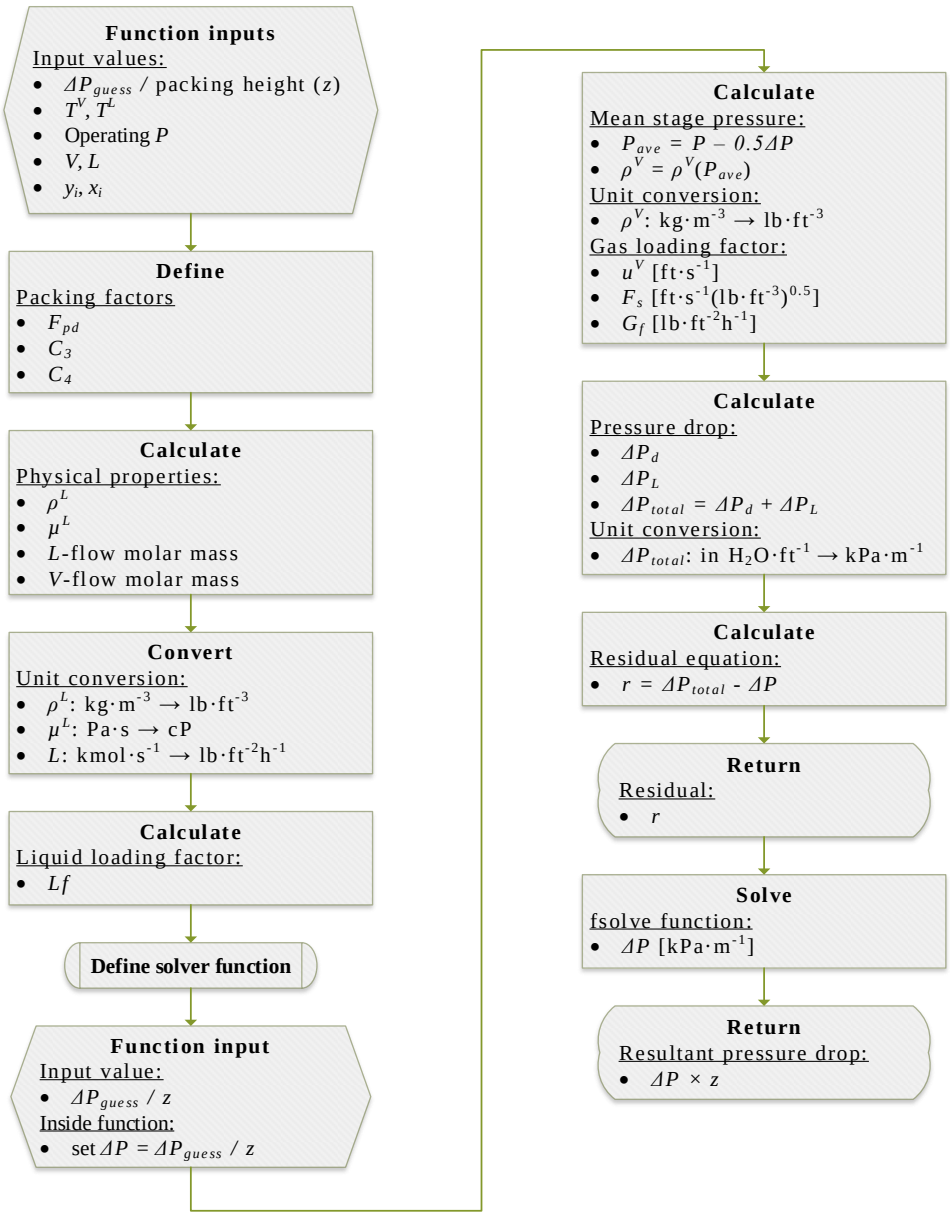

Figure 29: Pressure drop model algorithm

3.5.8 Reboiler Function

Similarly to the condenser function, the main goal of the reboiler function is to calculate the boil-up rate from the reboiler. To do this, the following assumptions are made:

- The liquid mixture in the reboiler is at its saturation temperature;
- The reboiler inner wall is at the same temperature as the utility fluid in the jacket (as $\dot{m}_{utility} \ggg \dot{m}_{boil-up}$);
- The liquid hold-up and boil-up vapours are in vapour-liquid equilibrium.

Figure 30 depicts the algorithm used in the reboiler function. The modelling equations and auxiliary functions used in this algorithm, include:

- Equations137 and 194;
- VLE bubble temperature and pressure functions;
- Vapour and liquid enthalpy functions;
- Mixed heat of vapourisation function;
- Mixed liquid heat capacity function:
- Vapour and liquid density functions;
- Liquid viscosity, thermal conductivity and surface tension functions.

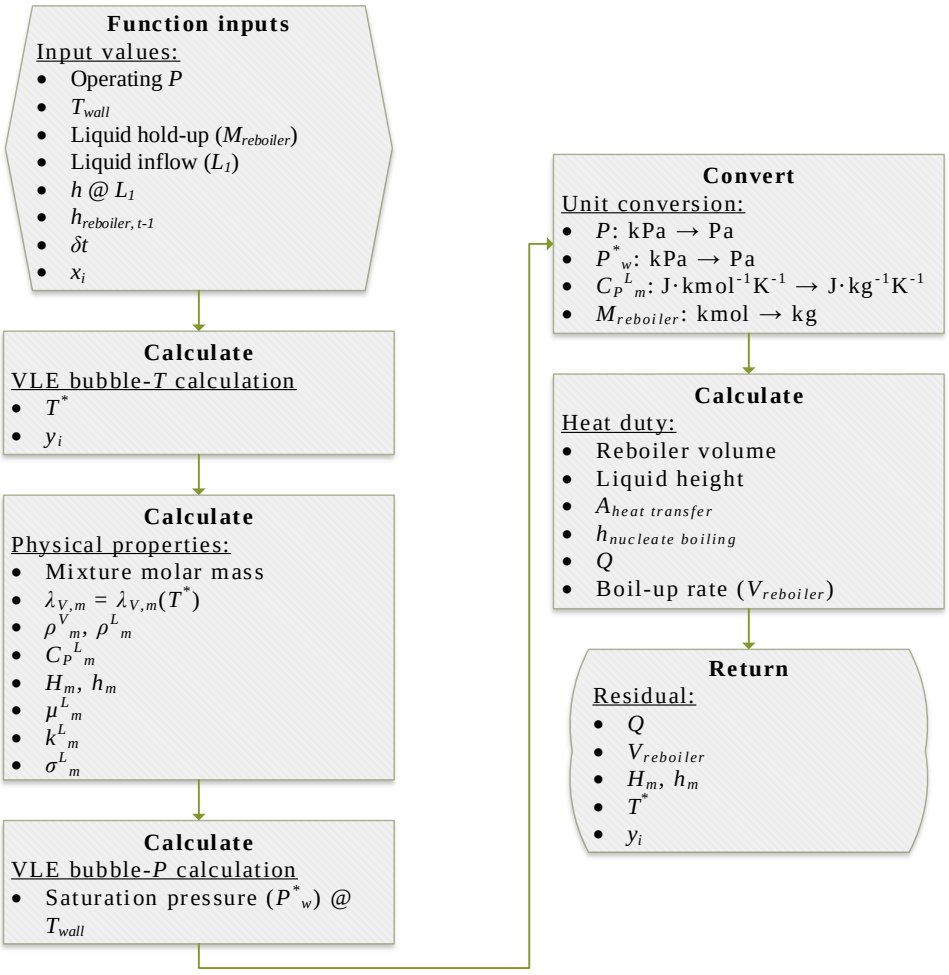

Figure 30: Reboiler model algorithm

3.5.9 Reflux Line Outflow

A model for the liquid reflux flow was derived by performing a mechanical energy balance (MEB) over the reflux line depicted in Figure 21. A total MEB (Greeff & Skinner, 2000: 24-31) can be defined through Equation 200

$$\Delta P_a = \Delta P_{EP} + \Delta P_{EL} + \Delta P_{KE} + \Delta P_f + \Delta P_{CV} \tag{200}$$

where ΔP_a denotes the pressure drop over a fluid mover (such as a pump), ΔP_{EP} denotes the difference in end-point pressures, ΔP_{EL} denotes the pressure drop due to the changes in elevation of the system, ΔP_{KE} denotes the pressure drop due to changes in kinetic energy, ΔP_f denotes pressure drop brought on by frictional losses and ΔP_{CV} is the pressure drop over the control valve. Equation 200 can be simplified to describe the reflux line, by equating the following terms to zero:

- ΔP_a, as there is no fluid mover in the line;
- ΔP_{EP}, since the inlet to the condenser can be traced back to the column top, where the reflux line exits.

Furthermore, if one considers the equation for ΔP_{KE}

$$\Delta P_{KE} = \frac{\rho \times \alpha_{KE}}{2000}\left(u_2^2 - u_1^2\right) \tag{201}$$

this term will also reduce to zero when there is flow in the reflux tube, as the two reference point velocities, u_1 and u_2, will be equal. The simplified form of Equation 200 can, therefore, be rearranged to express the pressure drop over the needle valve in the line

$$\Delta P_{CV} = -\Delta P_{EL} - \Delta P_f \tag{202}$$

which in turn can be used to calculate the flow through the valve (Greeff & Skinner, 2000: 91-92)

$$\dot{V} = C_V f(x)\sqrt{\frac{\Delta P_{CV}}{SG}} \tag{203}$$

where $\dot{V}$ is the volumetric flow rate in gpm, C_V is the control valve coefficient, ΔP_{CV} is in psi, SG is the specific gravity of the fluid and $f(x)$ is a fraction of the total flow area of the valve, as a function of the valve stem position, x. Needle valves generally have linear flow characteristics (Sölken, 2019), which means $f(x) = x$. The needle valve installed in the reflux line has a C_V-value of 0.09 (Swagelok, 2019).

Equation 204 can be used to calculate the pressure drop due to changes in elevation

$$\Delta P_{EL} = \frac{\rho g \left(h_2 - h_1\right)}{1000} \tag{204}$$

here, g is the acceleration due to gravity (9.807 m·s^{-2}), h is change in height (m) and ρ and ΔP_{EL} have units of kg·m^{-3} and kPa, respectively. Equation 205 is used to calculate the pressure drop over the line due to frictional losses

$$\Delta P_f = \frac{f' L_e}{D_i} \frac{\rho^L u^2}{2000} \tag{205}$$

where f' is the friction factor, which can be calculated by Equations 139, 140 and 141, D_i is the inside tube diameter in m, L_e is the system's total equivalent length in m, u is the linear liquid velocity in m·s^{-1} and ρ^L has units of kg·m^{-3}. The bends in the reflux tube were treated as elbow-fittings, with equivalent lengths calculated using the two-K method. The K-values for the tube bends were calculated using Equation 206, while the K-value for the tube exit was calculated using Equation 207

$$K = \frac{K_1}{Re} + K_\infty \left(1 + \frac{1}{D_i}\right) \tag{206}$$

$$K = \frac{K_1}{Re} + K_\infty \tag{207}$$

It is important to note that D_i in Equation 206 has units of inches. The applicable K_1 and K_∞-values are reported in Table 27. Once all the K-values have been calculated, Equation 208 can be used to calculate the total equivalent length

$$L_e = L_{tube} + \frac{D_i}{f'} \times \sum K \tag{208}$$

where the sum of K refers to the sum of all the K-values in the system. The algorithm used to put this model together is presented in Figure 31.

Table 27: K_1 and K_∞-values for fittings in the reflux line (Greeff & Skinner, 2000)

Fitting	K_1	K_∞
Exit	0	1
90° elbow	800	0.25
180° elbow	1000	0.3

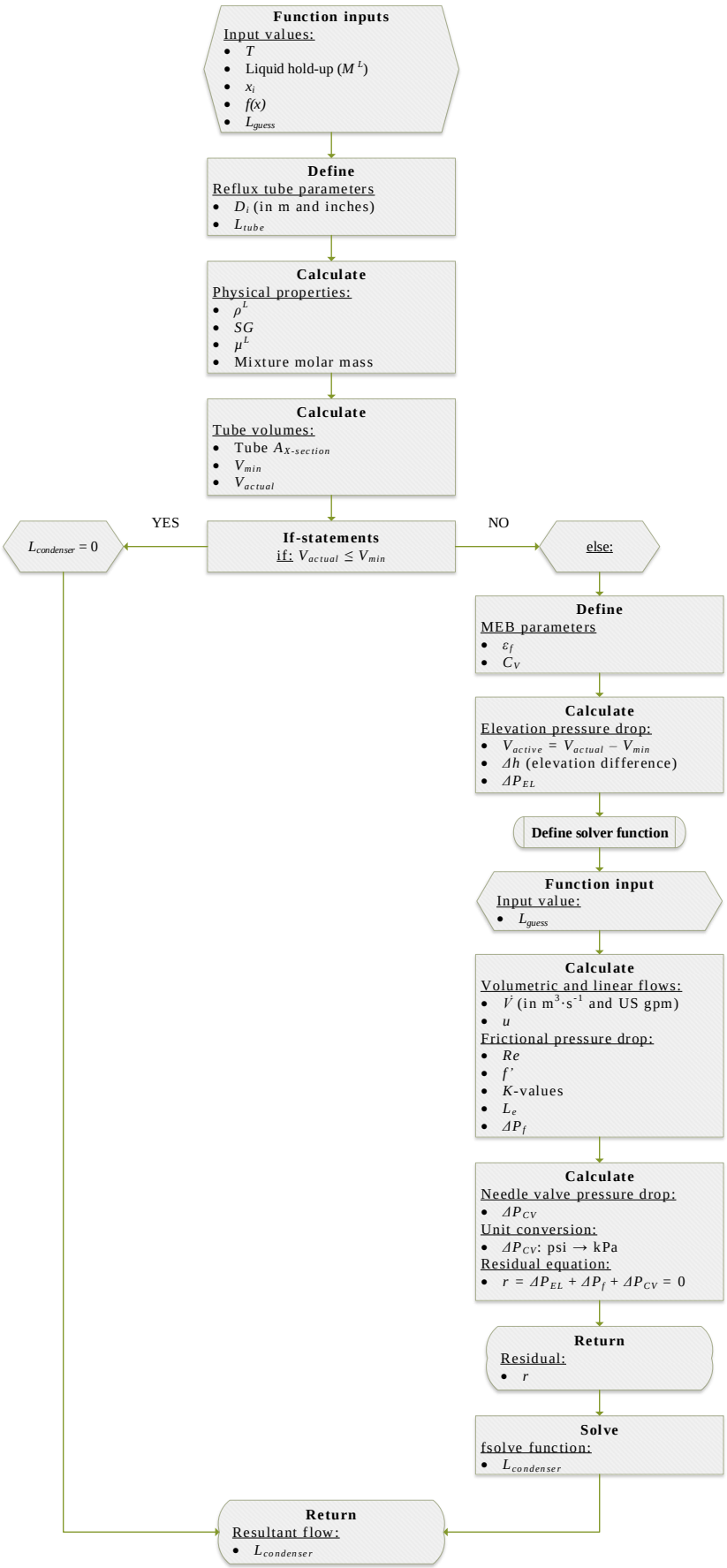

Figure 31: Reflux flow algorithm

Results and Discussion

4.1 Simulation Initialisation

Since a numerical integration technique is applied to solve the differential equations, sets of initial values are required as inputs to the simulations, to start the integration. One way to generate these initial values is to feed a set of "dummy" variables to the simulation and to run it until the system reaches a steady-state. The achieved steady-state values then become the new set of inputs from which the actual simulations can be run. The operating and feed conditions to which the two simulation programs were initialised are indicated in Table 28.

Table 28: Column operating conditions for the first simulation initialisations

Variable	Value	Units
Operating pressure	160	kPa
Condenser temperature	-67	°C
Reboiler temperature	-20	°C
Feed temperature	23	°C
Feed flow rate	250	sccm
	2.96×10^{-7}	kmol·s^{-1}
z_{TFE}	0.6	-
z_{HFP}	0.3	-
z_{OFCB}	0.1	-
Reflux valve stem position ($f(x)$)	0.3	-

The initialisation results are listed in Table A.1. An important aspect to consider when looking at these results is whether it is practical for the system to reach this specific steady-state. For example:

1. Are the molar hold-ups in the reboiler and reflux line and on the packed sections within the physical volume (or height) restrictions?

2. Does the feed cylinder contain enough gas to produce the steady-state obtained by the initialisation, and to run the column continuously from that point onward?

The first question can be answered by calculating the volume that each hold-up occupies, and compare it to the total available volume. The available volumes of the reboiler, reflux line and each packed section can be calculated from the formula for a cylinder's volume. The packed section's volume is slightly modified, by multiplying the formula with the bed porosity. The porosity value has been set as 0.96 for the time being and needs to be validated experimentally. The liquid hold-up volumes can be calculated by dividing each molar hold-up by its molar density.

The volume comparison results in Table 29 indicate that the accumulated liquid hold-ups fall within the volumetric constraints. The hold-up in the reflux line comes close to the total available volume, especially in the rate model. However, in practice, this will not be a problem, as the condenser has a large enough volume to accommodate for the increased hold-up.

Table 29: Volumetric comparison of the liquid hold-ups obtained from the initialisation of the equilibrium and rate simulation models

Hold-Up Location (-)	Total Volume (mL)	Equilibrium Model (mL)	Rate Model (mL)
Reboiler	1002	253.0	241.5
Reflux line	0.7489	0.6696	0.7306
Section 1	45.24	2.058	2.857
Section 2	45.24	2.272	2.932
Section 3	45.24	2.496	2.992
Section 4	45.24	2.554	3.081
Section 5	45.24	2.560	3.174

An estimated answer to the second question can be obtained, by comparing the total amount of liquid hold-up in the column to the amount of gas in the feed cylinder, before a distillation run starts. Assuming that the feed cylinder, with a volume of 50 L, is stored at a pressure of 170 kPa and a temperature of 23 °C, the Peng-Robinson model (Section 2.2.6.1), together with Mathias-Copeman alpha function (Section 2.2.6.2) and the Wong-Sandler mixing rules (Section 2.2.6.3), can be used to calculate the amount of moles in the feed cylinder. The model produces 4 mol of the gas mixture in the cylinder. Adding the molar hold-ups in the reboiler, the packed sections and the reflux line produces values of 2.644 mol for the equilibrium-based model and 2.570 mol for the rate-based model.

Although these values are more than half the original amount of moles in the feed cylinder, it should, theoretically, be possible to achieve this steady-state and run the column continuously from that point on, provided that the gas pump in the feed line has the capacity to keep the column at its operating pressure at the lower feed cylinder pressures. Continuous operation should then be possible for approximately another hour.

Finally, for interest's sake, the steady-state composition and temperature results of the two models are presented in Figure 32 for comparison, while the internal flow rates are plotted in Figure 33. It is important to note the position labels on the x-axis. The right-most label reads "Reflux/Distillate", which corresponds to the top-most position for the liquid (Reflux) and vapour (Distillate) phases. The effect that the Maxwell-Stefan diffusion model has on the parameter distributions is interesting to see, as it translates to different efficiencies for each component on each packed section.

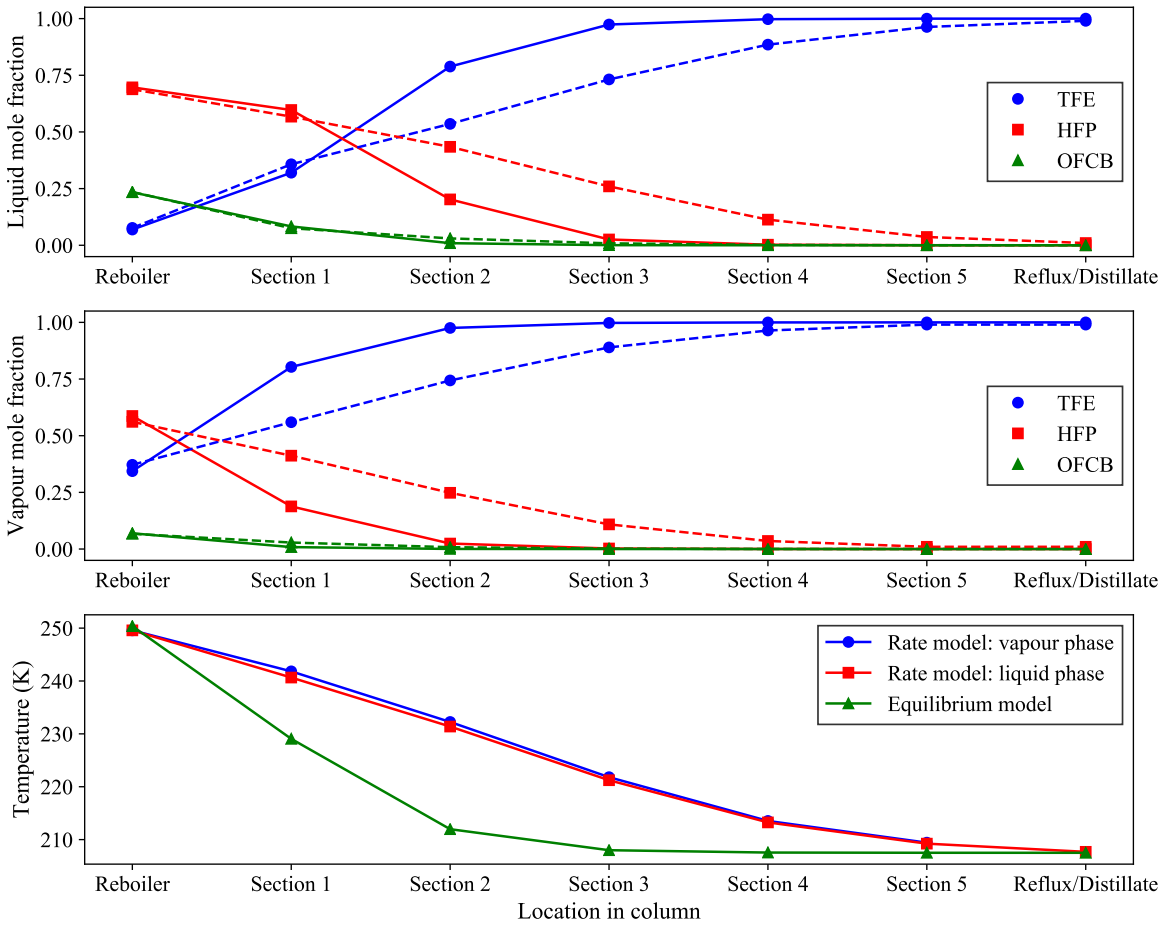

Figure 32: Molar composition and temperature comparison between the equilibrium (solid lines) and rate (dashed lines) models at steady-state under the operating conditions listed in Table 28

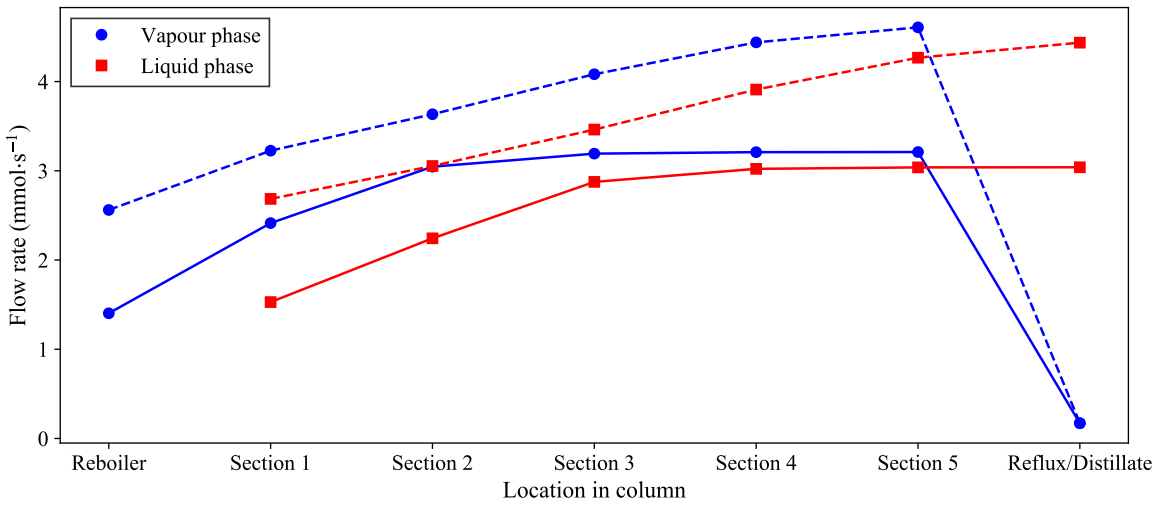

Figure 33: Comparison of the internal flows between the equilibrium (solid lines) and rate (dashed lines) models at steady-state under the operating conditions listed in Table 28

4.2 Dynamic Response of the Models

A step change to the feed flow rate was introduced to both models, to observe and compare the dynamic responses of the models. The steady-state conditions reported in Table A.1, under the operating conditions described in Table 28, was taken as the time zero inputs to each simulation. A step increase of 50 % in the feed flow rate was introduced to the simulations at a time of 10 s.

Each simulation was run at four different time step sizes (δt: 1, 0.5, 0.1, 0.05) to generating a comparison between the accuracy with which the numerical integration technique approximates the integrals, and the time it takes to perform the integration over the timespan. The timed results are presented in Table 30, while Figure 34 demonstrates the effect of each δt on the temperature profile on the first packed section.

Table 30: The effect of the different step sizes on simulation time

δt (s)	Integration Time (hh:mm:ss)	
	Equilibrium Model	Rate Model
1	0:00:39	0:09:45
0.5	0:01:19	0:19:41
0.1	0:06:36	1:39:09
0.05	0:13:07	3:34:17

The profiles for δt's of 0.1 and 0.05 are indistinguishable, signalling that a δt of 0.1 could

be the limit for integration accuracy. Unfortunately, simulations at this δt take too long to complete, therefore, a δt of 0.5 was set for further simulations, even though this value also takes a considerable amount of time to perform the integration, especially for the rate model. A δt of 1 is avoided as it can sometimes produce noisy profiles, especially at lower feed flow rates. The reason behind this has to do with the fact that, for simulation functions that contain solvers, previous time-step values are used as initial guesses, and convergence to the correct values are difficult to achieve if the difference between the timed values is too large.

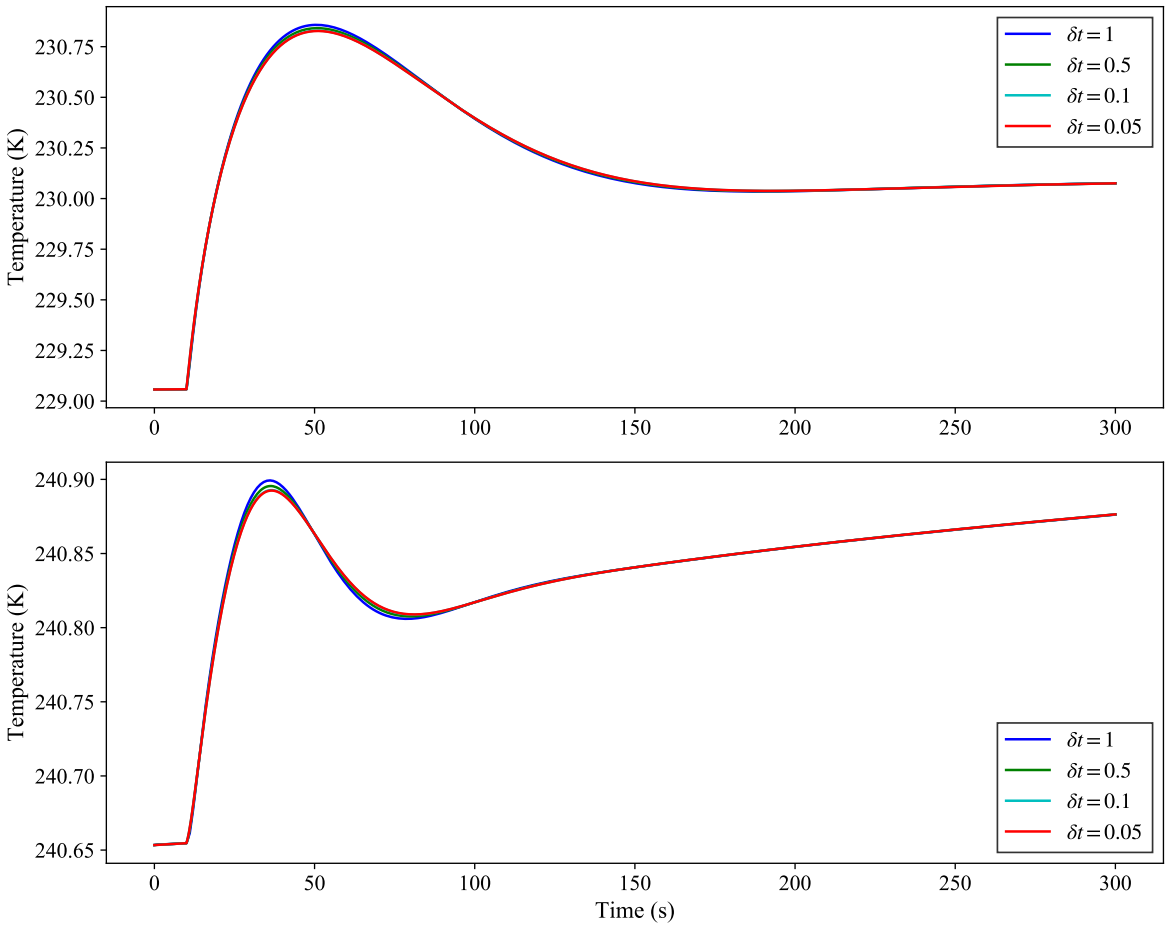

Figure 34: Comparison of the effect that different step sizes have on the integration accuracy of Euler's method for the equilibrium model (top figure) and rate model (bottom figure) simulations

The dynamic profiles for the temperatures, liquid and vapour mole fractions, liquid and vapour flow rates, pressure drop and liquid molar hold-ups are presented in Figures 35 to 43. The graphs in these figures are ordered in the same way you would expect to see the data in the column: the first graph on the bottom shows the profile of the reboiler, followed by the profile of the first packed section, and so on until it stops with the profiles for the reflux line.

One thing that becomes very apparent when looking at these figures, is that, although the responses follow the trends one would expect for such a system, the actual changes in the values on the y-axes are minute. The culprits, in this case, are the molar hold-up values (Figure 43), which are so large when compared to the feed flow rate, that the system responses merely absorb the incoming feed with little effect. The most pronounced effects are seen on the first two packed sections, but these values are also too small to be of practical importance. Simply increasing the feed rate with a factor of 10 or higher, is also not practical at this time, as the flow meter in the feed line has a maximum flow rating of 500 sccm.

The side-by-side presentation of the results for the two models makes for an interesting comparison. The profiles in both models follow second-order trends, however, the rate model responses seem to keep increasing past the point where it should have levelled off to its new steady-state. The ultimate effect sees a rise in the molar hold-ups, which lead to increased internal flows and a higher pressure drop (which can lead to the disproving of the assumption that pressure drop is negligible). It seems that the mass transfer model used by the rate simulation not only sets the efficiency of the column (when compared to the separation obtained by the equilibrium model) but also affects the dynamics of the model.

The effect of this is further seen in the vapour flow (Figure 41) and pressure drop (Figure 42) responses. Since vapour hold-ups are neglected by both models, the vapour flow (and as a result, the pressure drop) should see a sharp increase in value as the feed is increased, and then dynamically move to its steady-state position (as the equilibrium model does). However, this effect is only seen in the vapour flow and pressure drop responses in the first section. As the stage number goes up, the response becomes ever more slightly delayed in reaching its maximum overshoot value, giving it the illusion of having a dynamic response in that first section of the graph.

A second simulation was run, where a 250 sccm feed was introduced to the column at total reflux (time zero values in Table A.2). Both simulations produced profiles that are similar to the ones in Figures 35 to 43, except for the liquid molar hold-up and liquid flow responses of the equilibrium model. The instantaneous effect of the feed introduction causes the reflux molar hold-up to increase suddenly (due to more vapour being condensed), which in turn causes the reflux liquid flow to increase suddenly. This cascades down through the column and generates different liquid molar hold-up and liquid flow responses. These results are presented in Figures A.1 to A.9.

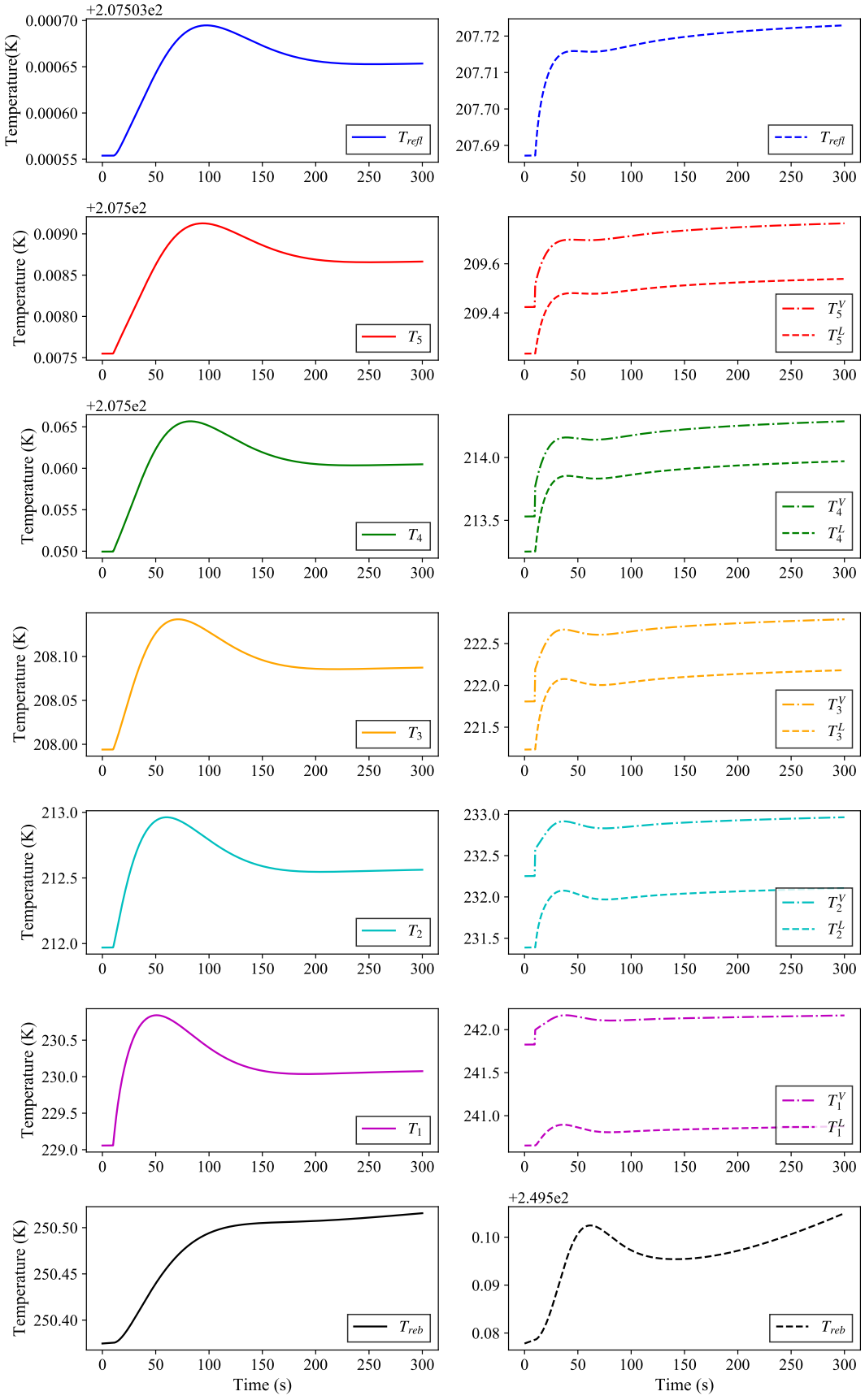

Figure 35: Temperature responses to a 50 % increase in feed for the equilibrium (left column) and rate (right column) models

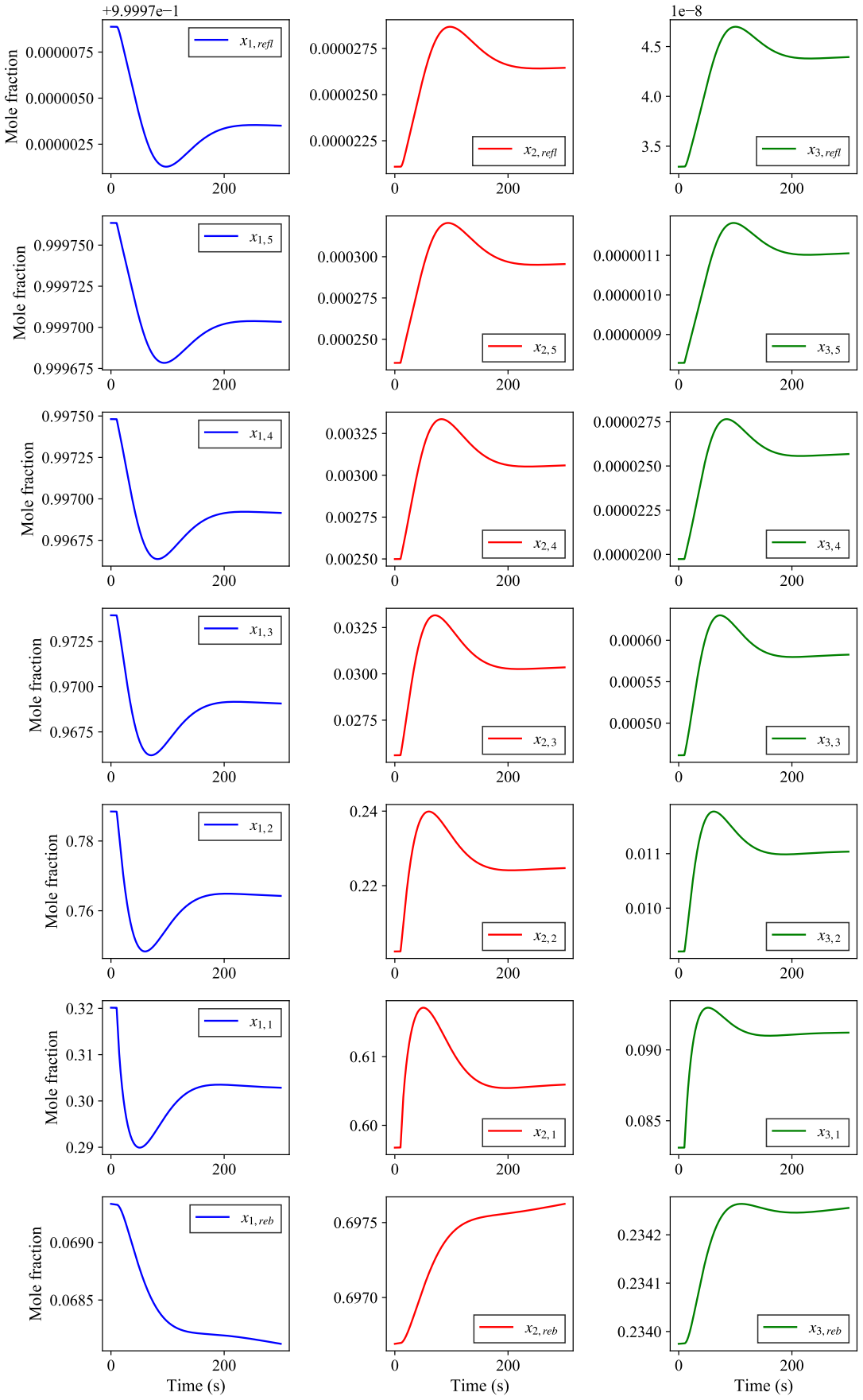

Figure 36: Liquid composition responses to a 50 % increase in feed for the equilibrium model

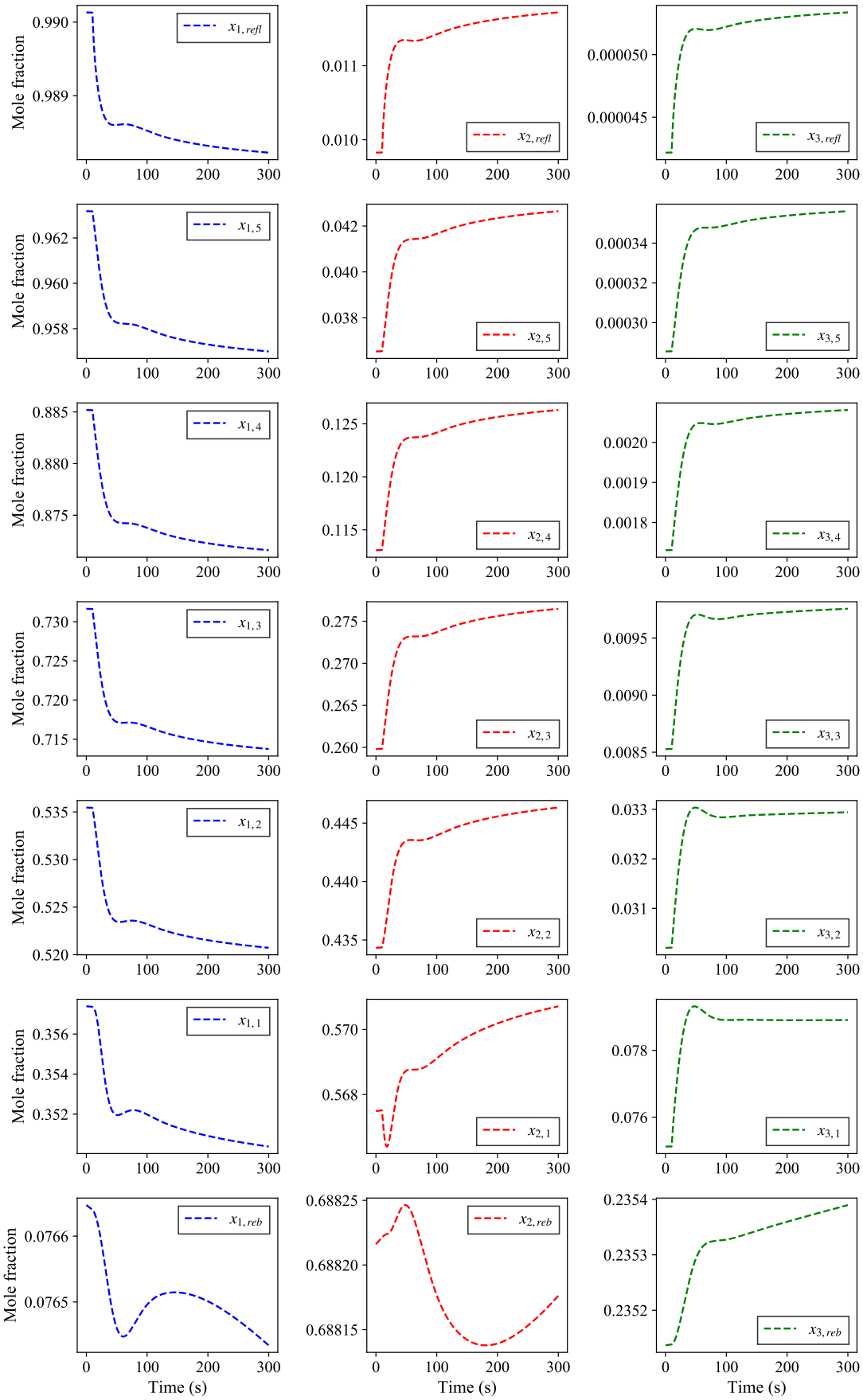

Figure 37: Liquid composition responses to a 50 % increase in feed for the rate model

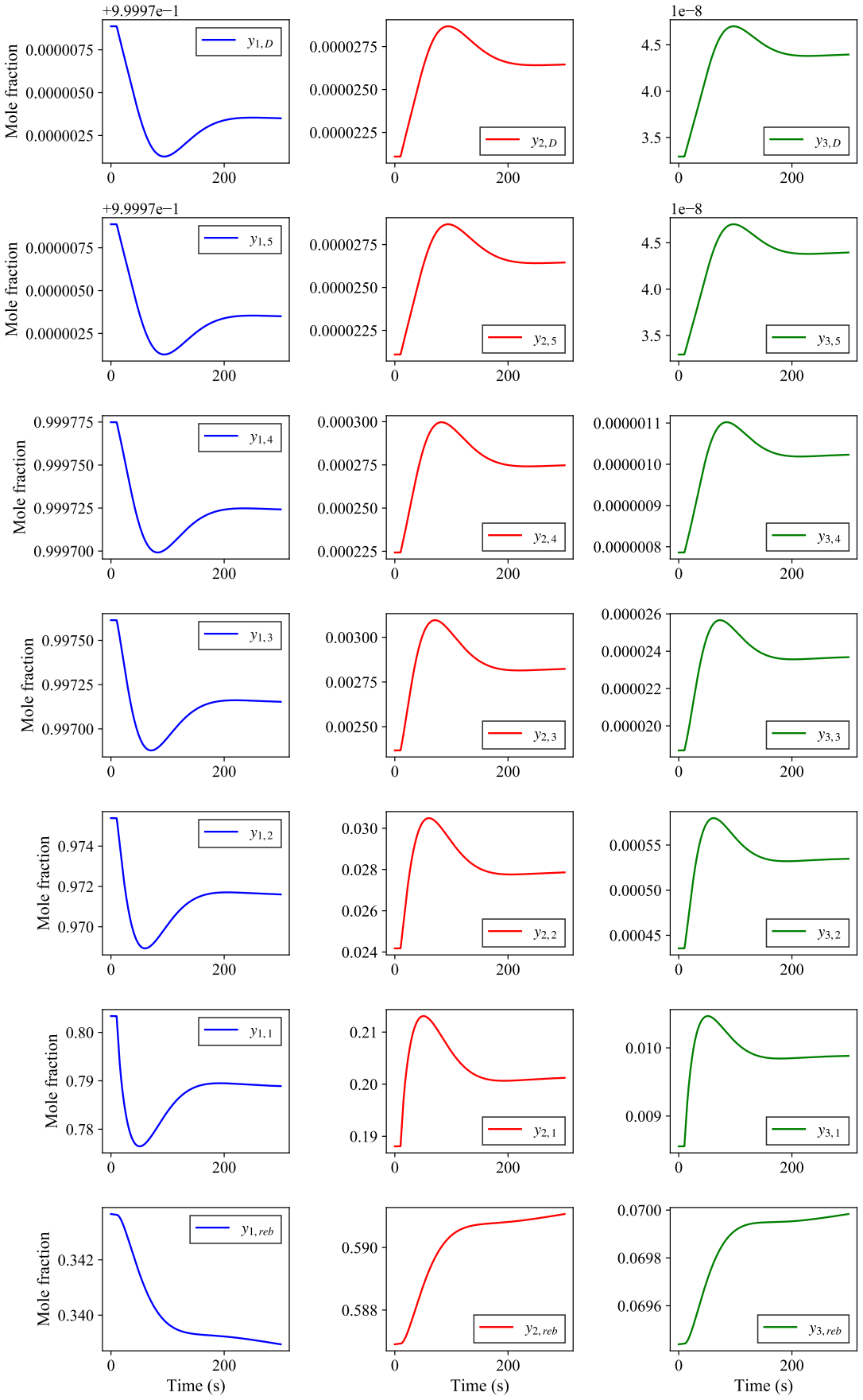

Figure 38: Vapour composition responses to a 50 % increase in feed for the equilibrium model

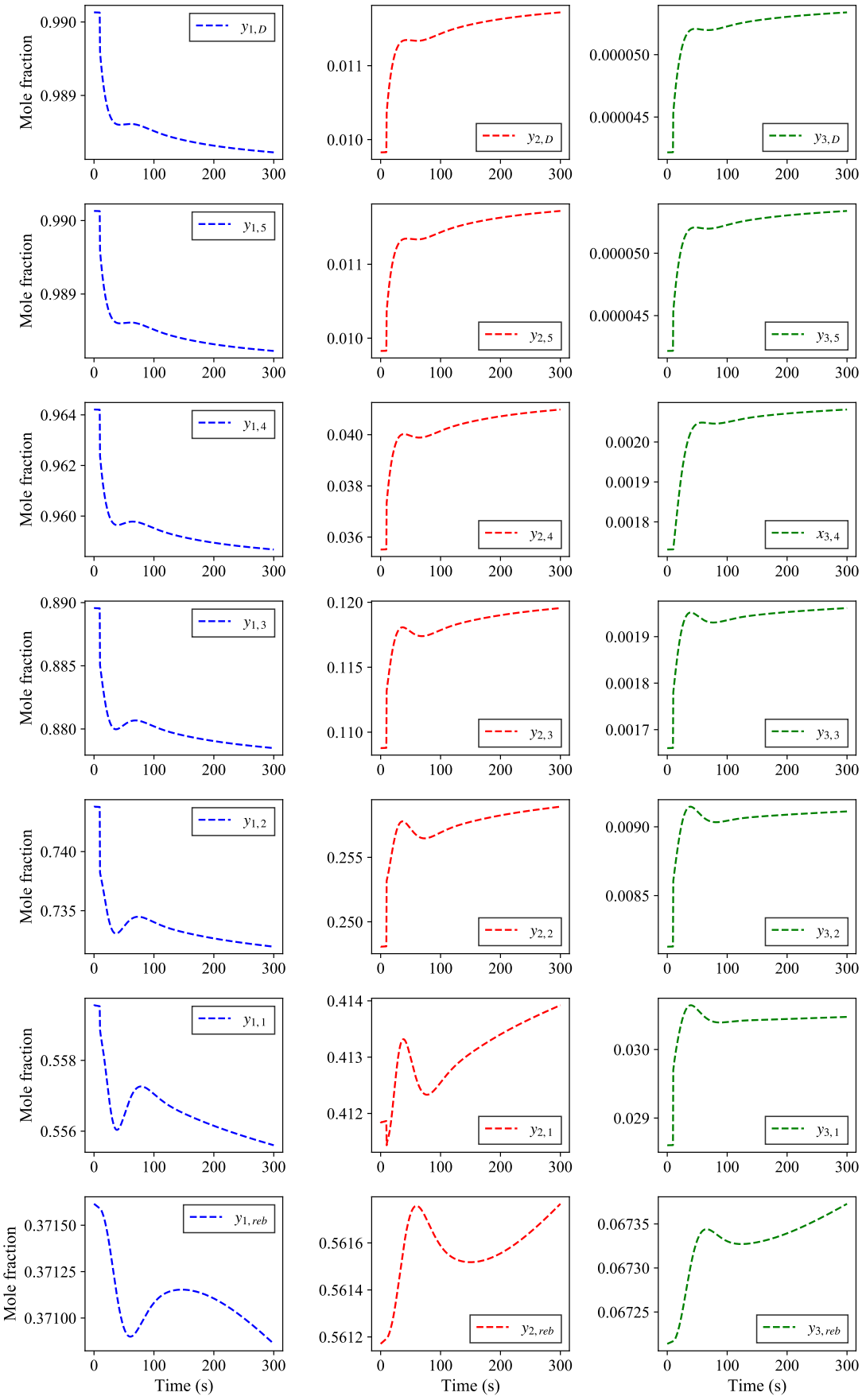

Figure 39: Vapour composition responses to a 50 % increase in feed for the rate model

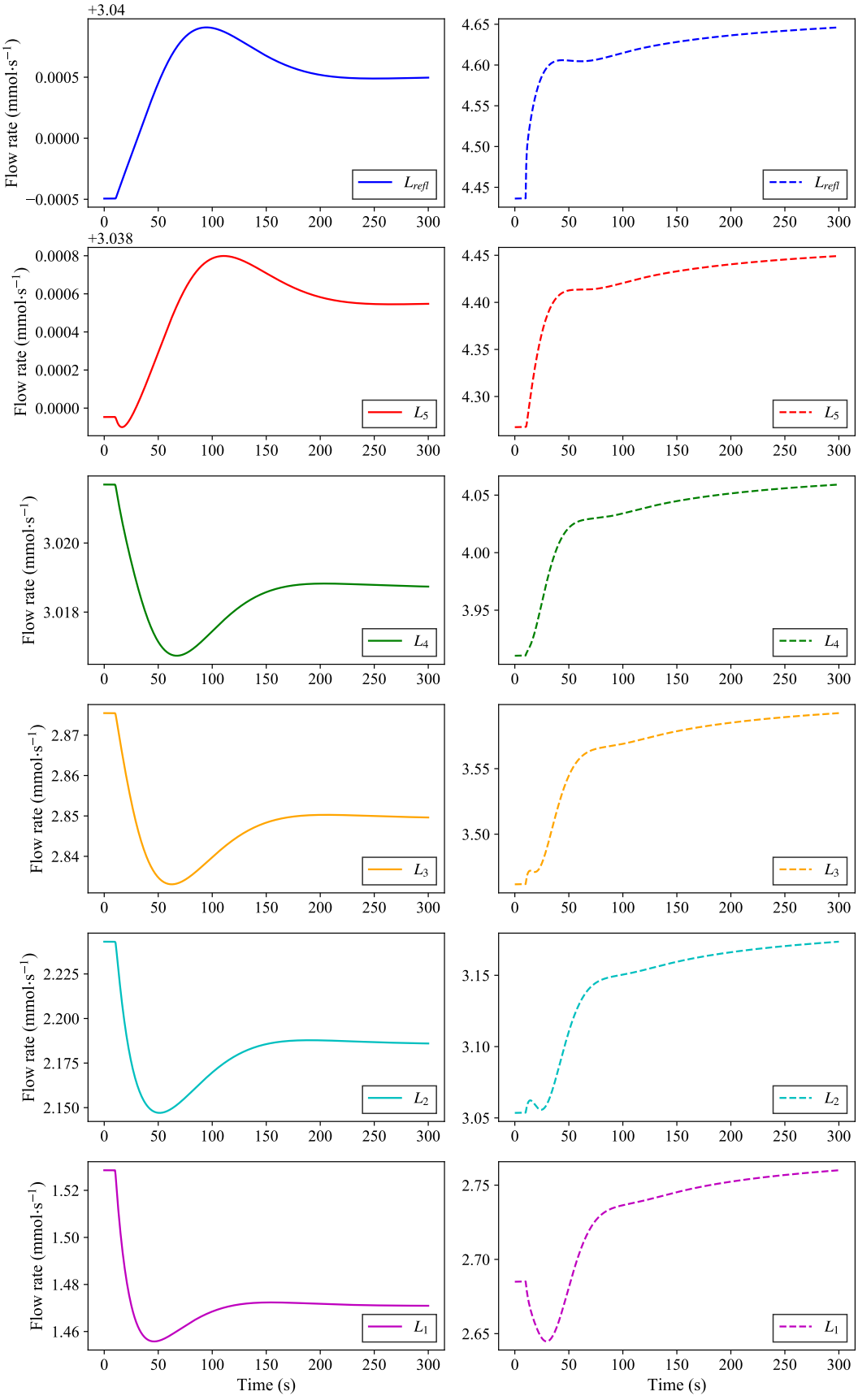

Figure 40: Liquid flow responses to a 50 % increase in feed for the equilibrium (left column) and rate (right column) models

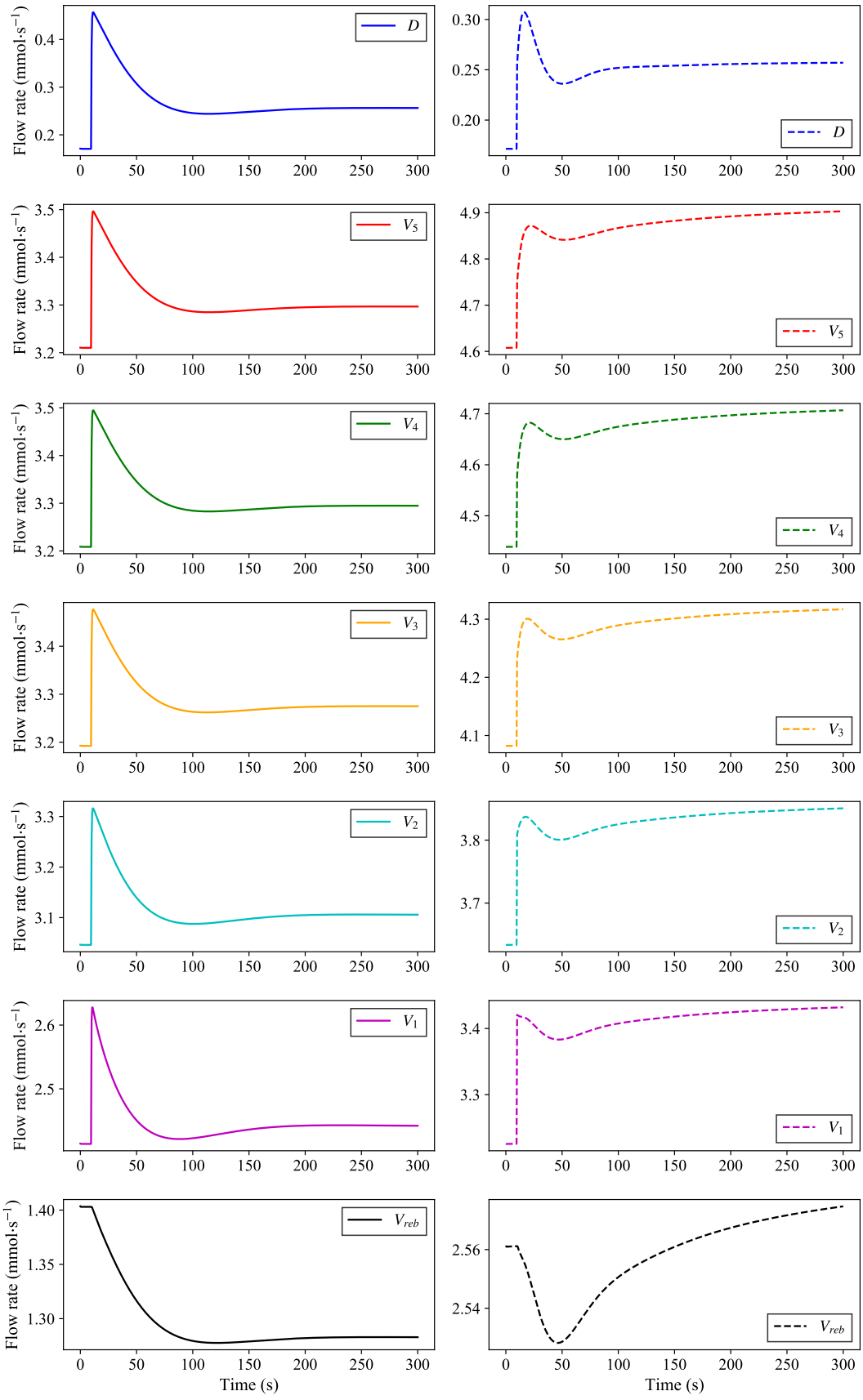

Figure 41: Vapour flow responses to a 50 % increase in feed for the equilibrium (left column) and rate (right column) models

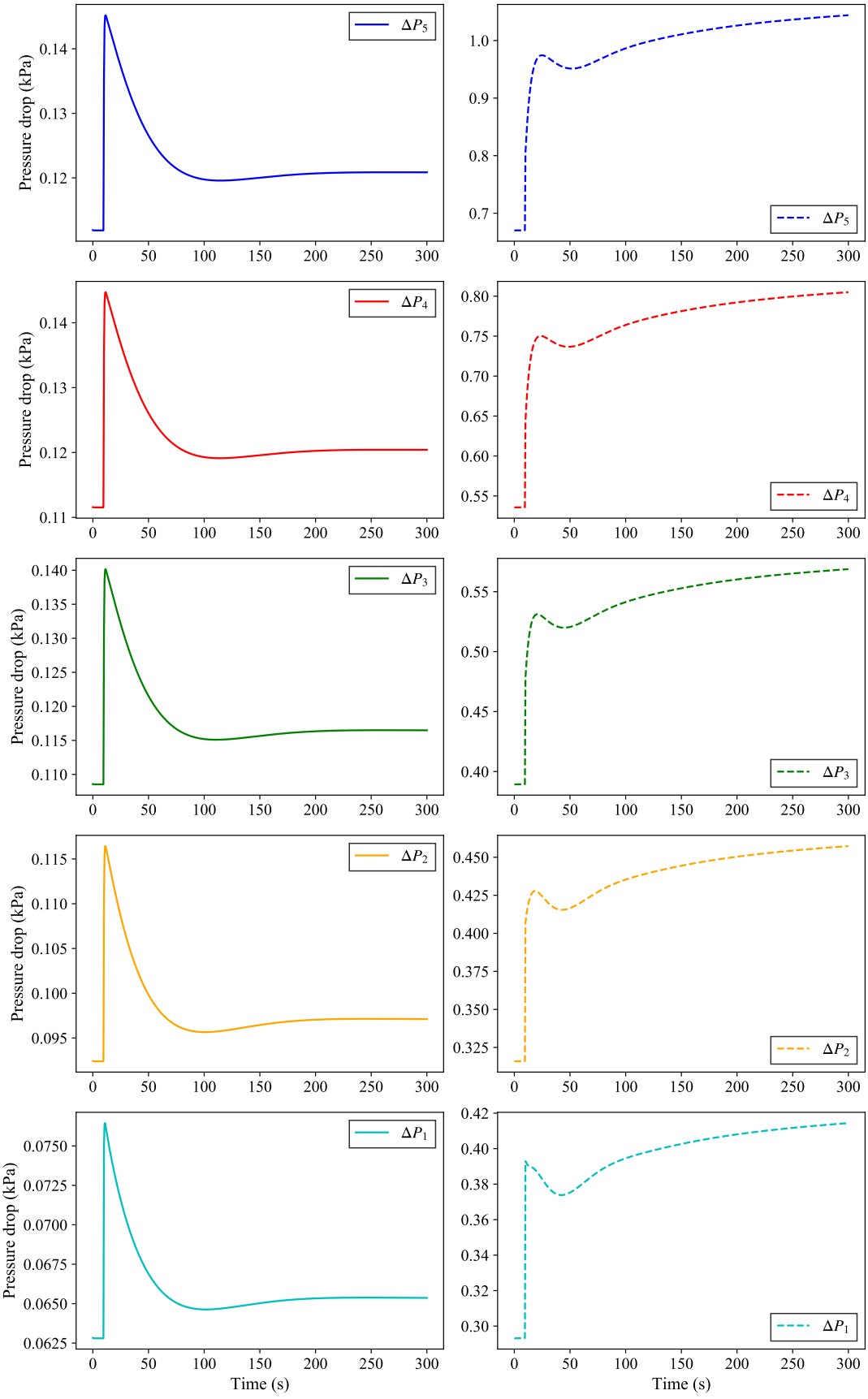

Figure 42: Pressure drop responses to a 50 % increase in feed for the equilibrium (left column) and rate (right column) models

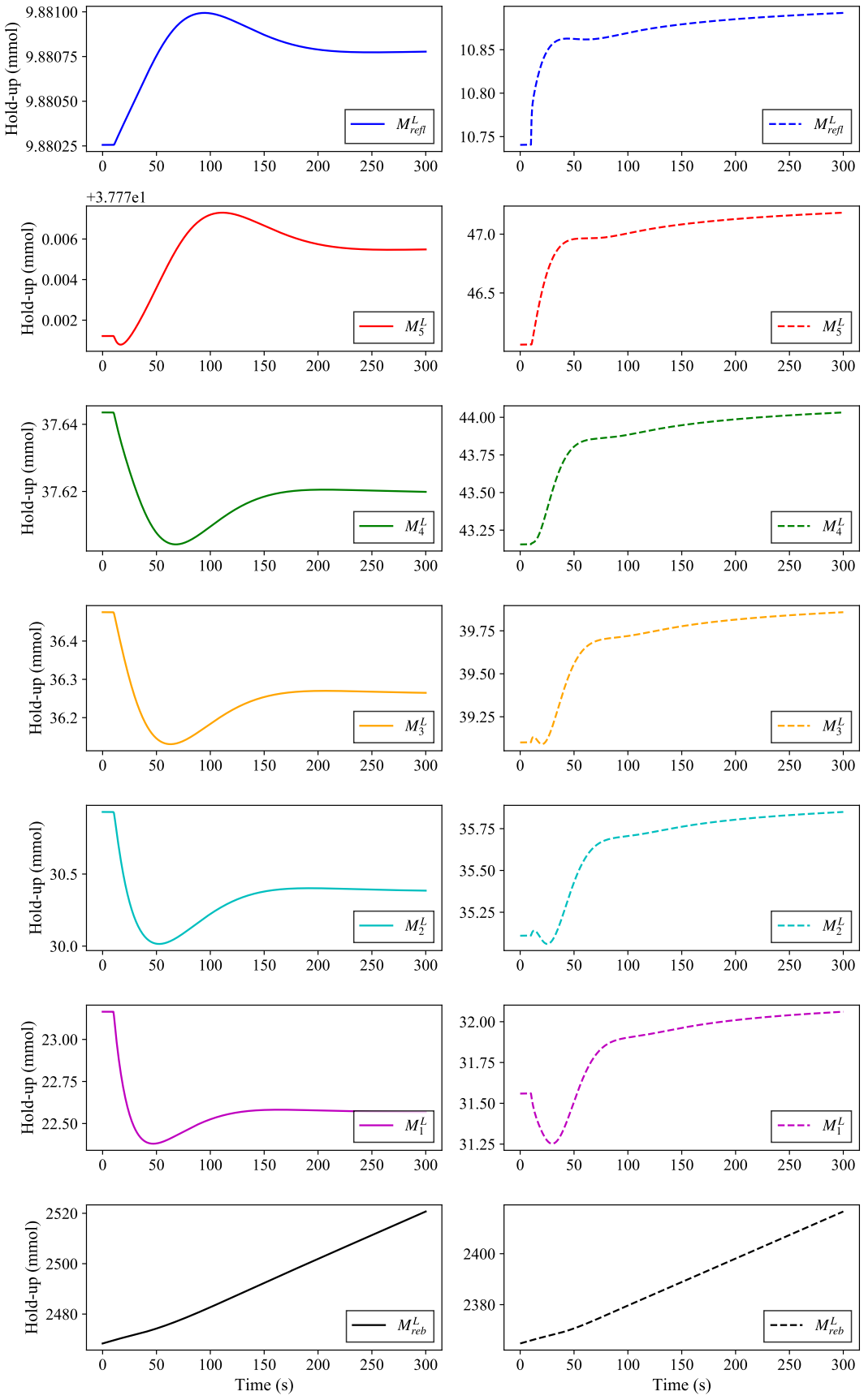

Figure 43: Molar liquid hold-up responses to a 50 % increase in feed for the equilibrium (left column) and rate (right column) models

Conclusions and Recommendations

The simulation programs for both the equilibrium and rate-based models produce the type of dynamic responses that can be expected in distillation systems. Unfortunately, these programs (especially the rate-based model) take too long to run and can therefore not be used in applications that require real-time execution (for example, in the column's control system). Furthermore, the models have not yet been tested against experimental data, and since a non-conventional packing type has been used, some calibration will be required.

The initialisation technique used is also not optimal and it produces steady-state hold-ups that are too large to be affected by the low feed flow rate. It is also not clear whether it would practically be possible to achieve such a steady-state and bring about a substantial change to the dynamics of the column (to search for the optimum operating conditions), as the feed cylinder may be too small to hold enough gas for this demand. From these conclusions, the following recommendations can be made:

Creating start-up simulations from these models may give a better platform for integration initialisations, as well as a better idea of how the column should be operated. As the system stands, and if the insights provided by the results in Section 4.2 are proven valid by experimental testing, the column may have to be run in a continuously dynamic state to produce the required separations. The work by Elgue *et al* (2004) describes algorithms that can be used to create start-up simulations.

Experimental validation of the models is the next important step that needs to take place. As mentioned earlier in this section, there are a few parameters in the models that will have to be fitted to the experimental data. These parameters include the bed porosity and the dry packing factor of the packing material.

Improving the simulation speed is crucial if one of the models are to be incorporated into the column's control system. One possible way of achieving this could be to test faster-solving methods, that still have some level of robustness. Apart from the *fsolve* solver, the *newton-krylov* solver was also tested to solve the Maxwell-Stefan

equations, but proved ineffective and would regularly run into a zero division problem. This can probably be attributed to the method with which the Jacobian matrix is approximated: which is a numerical iteration of the Krylov method (Scipy.org, 2014). A better approach might be to re-write the models in the CasADi environment (which has a version that is compatible with Python), which has built-in support routines for ordinary differential equation (ODE) and differential-algebraic equations (DAE) problems (Andersson *et al*, 2018).

Parallel processing can also be considered as a method to reduce simulation times, in cases where multiple scenarios have to be run for the same initial conditions (Prabhakaran, 2018). This will also result in better utilisation of the available processing power, as only one of the available six processors (these are the number of available processors in the author's computer) are utilised by the simulations. Parallel processing will, therefore, allow different simulation scenarios to be run on the different processors, simultaneously. Python modules that allow parallel processing include *multiprocessing* and *subprocess*.

Batch distillation simulations of binary HFP-OFCB mixtures should also be tested in future work. Once the model has been calibrated to experimental data, batch simulations of binary HFP-OFCB mixtures will also prove to be valuable in the future.

References

Andersson, JAE, Gillis, J, Horn, G, Rawlings, JB and Diehl, M (2018) *CasADi,* `https://web.casadi.org/1` [2019, December 02].

Bezuidenhoudt, A (2016) *Design and Implementation of a Continuous Polytetrafluoroethylene Depolymerisation System: Moving from Batch to Semi-Automated Continuous TFE Production*, Master's Thesis, University of Pretoria, Pretoria, South Africa.

Bezuidenhoudt, A, Sonnendecker, PW and Crouse, PL (2017) "Temperature and Pressure Effects on the Product Distribution of PTFE Pyrolysis by Means of Qualitative, in-Line FTIR Analysis" *Journal of Polymer Degradation and Stability*, *142*, 79–88.

Bhadury, PS, Singh, S, Sharma, M and Palit, M (2006) "Flash Pyrolysis of Polytetrafluoroethylene (Teflon) in a Quartz Assembly" *Journal of Analytical and Applied Pyrolysis*, *78*, 288–290.

Bonilla, J, Logist, F, Degrève, J, De Moore, B and Van Impe, J (2012) "A Reduced Order Rate Based Model for Distillation in Packed Columns: Dynamic Simulation and the Differentiation Index Problem" *Chemical Engineering Science*, *68*, 401–412.

Çengel, Y A and Ghajar, A J (2015) *Heat and Mass Transfer*, 5th ed. McGraw-Hill, New York.

Conradie, FJ (2011) *Batch Separation of Tetrafluoroethylene, Hexafluoropropylene and Octafluorocylobutane*, Master's Thesis, University of Pretoria, Pretoria, South Africa.

Conradie, FJ, Crouse, PL, Courtial, X, Nelson, WM, van der Walt, IJ and Ramjugernath, D (2013) "Isothermal Vapor-Liquid Equilibrium Data for the 1,1,2,2-Tetrafluoroethene + 1,1,2,3,3,3-Hexafluoroprop-1-ene Binary System: Measurement and Modeling from (248 to 283) K" *Journal of Chemical & Engineering Data*, *59*, 82–88.

Conradie, FJ, Crouse, PL, Courtial, X, Nelson, WM, van der Walt, IJ and Ramjugernath, D (2015) "Isothermal Vapor-Liquid Equilibrium Data for the 1,1,2,3,3,3-Hexafluoroprop-

1-ene + 1,1,2,2,3,3,4,4-Octafluorocyclobutane Binary System: Measurement and Modeling from (292 to 352) K and Pressures up to 2.6 MPa" *Journal of Chemical & Engineering Data*, *60*, 966–969.

Conradie, FJ, Crouse, PL, Courtial, X, van der Walt, IJ and Ramjugernath, D (2012) "Isothermal Vapor-Liquid Equilibrium Data for the 1,1,2,2-Tetrafluoroethene + 1,1,2,2,3,3,4,4-Octafluorocyclobutane Binary System: Measurement and Modeling from (248 to 283) K" *Journal of Chemical & Engineering Data*, *57*, 1978–1983.

Coquelet, C, Ramjugernath, D, Madani, H, Valtz, A, Naidoo, P and Meniai, AH (2010) "Experimental Measurement of Vapor Pressures and Densities of Pure Hexafluoropropylene" *Journal of Chemical Engineering Data*, *55*, 2093–2099.

Elgue, S, Prat, L, Cabassud, M, Le Lann, JM and Cézerac, J (2004) "Dynamic Models for Start-Up Operations of Batch Distillation Columns with Experimental Validation" *Computers & Chemical Engineering*, *28(12)*, 2735–2747.

Florin, RE, Parker, MS and Wall, LA (1966) "The Mechanism of the Depolymerization of Polytetrafluoroethylene with Pyrolytic and Radiolytic Initiation" *Journal of Research of the National Bureau of Standards – A. Physics and Chemistry*, *70A (2)*, 115–131.

Furukawa, GT, McCoskey, RE and Reilly, ML (1953) "Heat Capacity, Heats of Fusion and Vaporization, and Vapor Pressure of Tetrafluoroethylene" *Journal of Research of the National Bureau of Standards*, *51(2)*, 69–72.

Furukawa, GT, McCoskey, RE and Reilly, ML (1954) "Heat Capacity, Heats of Transitions, Fusion and Vaporization and Vapor Pressure of Octafluorocyclobutane" *Journal of Research of the National Bureau of Standards*, *52(1)*, 11–16.

Greeff, IL and Skinner, W (2000) *Piping System Design*, University of Pretoria, Pretoria.

Karlström, A and Breitholtz, C (1992) "Experimental Validation of a Packed Bed Distillation Model" *Chemical Engineering Technology*, *15*, 406–416.

Kister, HZ (1992) *Distillation Design*, McGraw-Hill, New York.

Kooijman, HA and Taylor, R (1995) "A Nonequilibrium Model for Dynamic Simulation of Tray Distillation Columns" *AIChE Journal*, *41(8)*, 1852–1863.

Krishna, R and Standart, GL (1976) "A Multicomponent Film Model Incorporating a General Matrix Method of Solution to the Maxwell-Stefan Equations" *AIChE Journal*, *22(2)*, 383–389.

Krishna, R and Standart, GL (1979) "Mass and Energy Transfer in Multicomponent Systems" *Chemical Engineering Communications*, *3*, 201–275.

Krishna, R and Wesselingh, JA (1997) "The Maxwell-Stefan Approach to Mass Transfer" *Chemical Engineering Science*, *52(6)*, 861–911.

Krishnamurthy, R and Taylor, R (1985a) "A Nonequilibrium Stage Model of Multicomponent Separation Processes. Part I: Model Description and Method of Solution" *AIChE Journal*, *31(3)*, 449–456.

Krishnamurthy, R and Taylor, R (1985b) "Simulation of Packed Distillation and Absorption Columns" *Industrial & Engineering Chemistry Process Design and Development*, *24*, 513–524.

Lewis, EE and Naylor, MA (1947) "Pyrolysis of Polytetrafluoroethylene" *Journal of the American Chemical Society*, *68*, 1968–1970.

Ludwig, EE (1997) *Applied Process Design for Chemical and Petrochemical Plants: Volume 2*, Gulf Publishing Company, Houston.

Meissner, E, Wróblewska, A and Milchert, E (2004) "Technological Parameters of Pyrolysis of Waste Polytetrafluoroethylene" *Polymer Degradation and Stability*, *83*, 163–172.

NIST (2018) *Search for Species Data by Chemical Name,* `https://webbook.nist.gov/chemistry/name-ser/` [2019, August 01].

Peng, J, Edgar, TF and Eldridge, RB (2003) "Dynamic Rate-based and Equilibrium Models for a Packed Reactive Distillation Column" *Chemical Engineering Science*, *58*, 2671–2680.

Peng and Robinson, DB (1976) "A New Two-Constant Equation of State" *Industrial & Engineering Chemistry Fundamentals*, *15*, 59–64.

Perry, RH and Green, DW (1999) *Perry's Chemical Engineers' Handbook*, McGraw-Hill, New York.

Powers, MF, Vickery, DJ, Arehole, A and Taylor, R (1988) "A Nonequilibrium Stage Model of Multicomponent Separation Processes–V. Computational Methods for Solving the Model Equations" *Computers & Chemical Engineering*, *12(12)*, 1229–1241.

Prabhakaran, S (2018) *Parallel Processing in Python - A Practical Guide with Examples,* `https://www.machinelearningplus.com/python/parallel-processing-python/` [2020, January 29].

Prausnitz, JM, Lichtenthaler, RN and de Azevedo, EG (1999) *Molecular Thermodynamics of Fluid-Phase Equilibria*, Prentice Hall PTR, New Jersey.

Ramesh, K, Aziz, N, Abd Shukor, SR and Ramasamy, M (2007) "Dynamic Rate-Based and Equilibrium Model Approaches for Continuous Tray Distillation Columns" *Journal of Applied Sciences Research*, *3(12)*, 2030–2041.

Richardson, JF, Harker, JH and Backhurst, JR (2002) *Coulson and Richardson's Chemical Engineering Volume 2: Particle Technology and Separation Processes*, Butterworth-Heinemann, Oxford.

Scipy.org (2014) *scipy.optimize.newton_krylov,* `https://docs.scipy.org/doc/scipy-0.14.0/reference/generated/scipy.optimize.newton_krylov.html` [2019, December 02].

Shiflett, MB and Sandler, SI (1998) "Modeling Fluorocarbon Vapor-Liquid Equilibria using the Wong-Sandler Model" *Fluid Phase Equilibria*, *147*, 145–162.

Simon, CM and Kaminsky, W (1998) "Chemical Recycling of Polytetrafluoroethylene by Pyrolysis" *Polymer Degradation and Stability*, *62*, 1–7.

Sinnott, RK (2005) *Coulson and Richardson's Chemical Engineering Volume 6: Chemical Engineering Design*, Butterworth-Heinemann, Oxford.

Skogestad, S (1993) "Dynamics and control of distillation columns-a critical survey", in: *Dynamics and Control of Chemical Reactors, Distillation Columns and Batch Processes*, Elsevier: pp. 11–35.

Smith, JM, Van Ness, HC and Abbott, MM (2005) *Introduction to Chemical Engineering Thermodynamics*, McGraw-Hill, New York.

Sölken, W (2019) *Introduction to Needle valves,* `http://www.wermac.org/valves/valves_needle.html` [2019, November 10].

Sonnendecker, PW (2015) *Quantitative Analysis of Inline, Time-Resolved FTIR Spectra: Steps towards Full Automation*, Master's Thesis, University of Pretoria, Pretoria, South Africa.

Swagelok (2019) *SS-ORS2,* `https://www.swagelok.com/en/catalog/Product/Detail?part=SS-ORS2` [2019, November 10].

Taylor, R, Kooijman, HA and Hung, JS (1994) "A Second Generation Nonequilibrium Model for Computer Simulation of Multicomponent Separation Processes" *Computers & Chemical Engineering*, *18(3)*, 205–217.

Taylor, R and Krishna, R (1993) *Multicomponent Mass Transfer*, John Wiley & Sons, Inc, New York.

Taylor, R, Krishna, R and Kooijman, H (2003) "Real-World Modeling of Distillation" *CEP Magazine*, *7*, 28–39.

Van der Walt, IJ and Bruinsma, OSL (2006) "Depolymerization of Clean Unfilled PTFE Waste in a Continuous Process" *Journal of Applied Polymer Science*, *102*, 2752–2759.

Wall, LA and Michaelson, JD (1956) "Thermal Decomposition of Polytetrafluoroethylene in Various Gaseous Atmospheres" *Journal of Research of the National Bureau of Standards*, *56*, 27–34.

Wankat, PC (2012) *Separation Process Engineering*, Pearson, New Jersey.

Wilke, CR and Chang, P (1955) "Correlation of Diffusion Coefficients in Dilute Solutions" *AIChE Journal*, *1(2)*, 264–270.

Wong, DSH, Orbey, H and Sandler, SI (1992) "Equation of State Mixing Rule for Nonideal Mixtures Using Available Activity Coefficient Model Parameters and that Allows Extrapolation over Large Ranges of Temperature and Pressure" *Industrial & Engineering Chemistry Research*, *31*, 2033–2039.

Wong, DSH and Sandler, SI (1992) "A Theoretically Correct Mixing Rule for Cubic Equations of State" *AIChE Journal*, *38(5)*, 671–680.

Yaws, CL (2003) *Yaws' Handbook of Thermodynamic and Physical Properties of Chemical Compounds,* `https://app.knovel.com/web/toc.v/cid:kpYHTPPCC4/viewerType:toc/` [2019, August 05].

Yaws, CL (2009) *Yaws' Handbook of Thermodynamic Properties for Hydrocarbons and Chemicals,* `https://app.knovel.com/web/toc.v/cid:kpYHTPHC09/viewerType:toc/?hierarchy=kn0V6R2PFC` [2019, August 05].

Yaws, CL (2010a) *Yaws' Thermophysical Properties of Chemicals and Hydrocarbons (Electronic Edition),* `https://app.knovel.com/hotlink/toc/id:kpYTPCHE02/yaws-thermophysical-properties/yaws-thermophysical-properties` [2019, August 05].

Yaws, CL (2010b) *Yaws' Transport Properties of Chemicals and Hydrocarbons (Electronic Edition),* `https://app.knovel.com/web/toc.v/cid:kpYHTPPCC4/viewerType:toc/` [2019, August 05].

Appendix A

A.1 Simulation Initialisation Results

Table A.1: Equilibrium and rate model initialisation results for the operating conditions and feed inputs presented in Table 28

Variable	Equilibrium Model	Rate Model	Units
$x_{1,1}$	0.32014	0.35739	-
$x_{2,1}$	0.59676	0.56749	-
$x_{3,1}$	0.08310	0.07512	-
$x_{1,2}$	0.78846	0.53546	-
$x_{2,2}$	0.20234	0.43433	-
$x_{3,2}$	9.2046×10^{-3}	0.03020	-
$x_{1,3}$	0.97393	0.73166	-
$x_{2,3}$	0.02560	0.25981	-
$x_{3,3}$	4.6123×10^{-4}	8.5280×10^{-3}	-
$x_{1,4}$	0.99748	0.88519	-
$x_{2,4}$	2.4991×10^{-3}	0.11308	-
$x_{3,4}$	1.9735×10^{-5}	1.7308×10^{-3}	-
$x_{1,5}$	0.99976	0.96318	-
$x_{2,5}$	2.3568×10^{-4}	0.03653	-
$x_{3,5}$	8.2833×10^{-7}	2.8551×10^{-4}	-
$x_{1,cond}$	0.99998	0.99013	-
$x_{2,cond}$	2.1094×10^{-5}	9.8268×10^{-3}	-
$x_{3,cond}$	3.2943×10^{-8}	4.2167×10^{-5}	-
$x_{1,refl}$	0.99998	0.99013	-
$x_{2,refl}$	2.1093×10^{-5}	9.8261×10^{-3}	-
$x_{3,refl}$	3.2941×10^{-8}	4.2164×10^{-5}	-
$x_{1,reb}$	0.06933	0.07665	-
$x_{2,reb}$	0.69669	0.68822	-

$x_{3,reb}$	0.23397	0.23514	-
$y_{1,1}$	0.80338	0.55956	-
$y_{2,1}$	0.18807	0.41184	-
$y_{3,1}$	8.5551×10^{-3}	0.02860	-
$y_{1,2}$	0.97539	0.74380	-
$y_{2,2}$	0.02418	0.24807	-
$y_{3,2}$	4.3546×10^{-4}	8.1288×10^{-3}	-
$y_{1,3}$	0.99761	0.88957	-
$y_{2,3}$	2.3671×10^{-3}	0.10877	-
$y_{3,3}$	1.8685×10^{-5}	1.6602×10^{-3}	-
$y_{1,4}$	0.99977	0.96421	-
$y_{2,4}$	2.2431×10^{-4}	0.03551	-
$y_{3,4}$	7.8614×10^{-7}	2.7618×10^{-4}	-
$y_{1,5}$	0.99998	0.99013	-
$y_{2,5}$	2.1094×10^{-5}	9.8268×10^{-3}	-
$y_{3,5}$	3.2943×10^{-8}	4.2167×10^{-5}	-
$y_{1,D}$	0.99998	0.99013	-
$y_{2,D}$	2.1094×10^{-5}	9.8268×10^{-3}	-
$y_{3,D}$	3.2943×10^{-8}	4.2167×10^{-5}	-
$y_{1,reb}$	0.34366	0.37162	-
$y_{2,reb}$	0.58690	0.56117	-
$y_{3,reb}$	0.06944	0.06721	-
L_1	1.5285×10^{-6}	2.6850×10^{-6}	$\text{kmol}\cdot\text{s}^{-1}$
L_2	2.2431×10^{-6}	3.0535×10^{-6}	$\text{kmol}\cdot\text{s}^{-1}$
L_3	2.8755×10^{-6}	3.4617×10^{-6}	$\text{kmol}\cdot\text{s}^{-1}$
L_4	3.0217×10^{-6}	3.9104×10^{-6}	$\text{kmol}\cdot\text{s}^{-1}$
L_5	3.0380×10^{-6}	4.2674×10^{-6}	$\text{kmol}\cdot\text{s}^{-1}$
L_{cond}	3.0395×10^{-6}	4.4362×10^{-6}	$\text{kmol}\cdot\text{s}^{-1}$
L_{refl}	3.0395×10^{-6}	4.4361×10^{-6}	$\text{kmol}\cdot\text{s}^{-1}$
V_1	2.4137×10^{-6}	3.2255×10^{-6}	$\text{kmol}\cdot\text{s}^{-1}$
V_2	3.0461×10^{-6}	3.6336×10^{-6}	$\text{kmol}\cdot\text{s}^{-1}$
V_3	3.1923×10^{-6}	4.0822×10^{-6}	$\text{kmol}\cdot\text{s}^{-1}$
V_4	3.2086×10^{-6}	4.4390×10^{-6}	$\text{kmol}\cdot\text{s}^{-1}$
V_5	3.2101×10^{-6}	4.6076×10^{-6}	$\text{kmol}\cdot\text{s}^{-1}$
V_{refl}	1.4030×10^{-6}	2.5610×10^{-6}	$\text{kmol}\cdot\text{s}^{-1}$
D	1.7064×10^{-7}	1.7143×10^{-7}	$\text{kmol}\cdot\text{s}^{-1}$
T_1^L	229.06	240.65	K
T_2^L	211.97	231.39	K
T_3^L	207.99	221.23	K

T_4^L	207.55	213.25	K
T_5^L	207.51	209.23	K
T_{cond}	207.50	207.69	K
T_{refl}	207.50	207.69	K
T_{reb}	250.37	249.58	K
T_1^V	-	241.83	K
T_2^V	-	232.25	K
T_3^V	-	221.81	K
T_4^V	-	213.53	K
T_5^V	-	209.42	K
M_1^L	2.3165×10^{-5}	3.1559×10^{-5}	kmol
M_2^L	3.0931×10^{-5}	3.5110×10^{-5}	kmol
M_3^L	3.6475×10^{-5}	3.9101×10^{-5}	kmol
M_4^L	3.7644×10^{-5}	4.3155×10^{-5}	kmol
M_5^L	3.7771×10^{-5}	4.6060×10^{-5}	kmol
M_{refl}^L	9.8803×10^{-6}	1.0740×10^{-5}	kmol
M_{reb}^L	2.4683×10^{-3}	2.3648×10^{-3}	kmol
$x_{1,1}^I$	-	0.14694	-
$x_{2,1}^I$	-	0.71028	-
$x_{3,1}^I$	-	0.14278	-
$x_{1,2}^I$	-	0.26805	-
$x_{2,2}^I$	-	0.66820	-
$x_{3,2}^I$	-	0.06375	-
$x_{1,3}^I$	-	0.47745	-
$x_{2,3}^I$	-	0.50183	-
$x_{3,3}^I$	-	0.02072	-
$x_{1,4}^I$	-	0.73641	-
$x_{2,4}^I$	-	0.25890	-
$x_{3,4}^I$	-	4.6933×10^{-3}	-
$x_{1,5}^I$	-	0.90903	-
$x_{2,5}^I$	-	0.09015	-
$x_{3,5}^I$	-	8.1063×10^{-4}	-
$y_{1,1}^I$	-	0.56303	-
$y_{2,1}^I$	-	0.40938	-
$y_{3,1}^I$	-	0.02758	-
$y_{1,2}^I$	-	0.74802	-
$y_{2,2}^I$	-	0.24438	-
$y_{3,2}^I$	-	7.5909×10^{-3}	-
$y_{1,3}^I$	-	0.89320	-

$y^I_{2,3}$	-	0.10532	-
$y^I_{3,3}$	-	1.4779×10^{-3}	-
$y^I_{1,4}$	-	0.96625	-
$y^I_{2,4}$	-	0.03351	-
$y^I_{3,4}$	-	2.3387×10^{-4}	-
$y^I_{1,5}$	-	0.99089	-
$y^I_{2,5}$	-	9.0708×10^{-3}	-
$y^I_{3,5}$	-	3.4501×10^{-5}	-
T^I_1	-	241.53	K
T^I_2	-	231.99	K
T^I_3	-	221.49	K
T^I_4	-	213.25	K
T^I_5	-	209.28	K
$\mathcal{N}_{1,1}$	-	-6.7551×10^{-7}	$\text{kmol}\cdot\text{s}^{-1}$
$\mathcal{N}_{2,1}$	-	1.9759×10^{-7}	$\text{kmol}\cdot\text{s}^{-1}$
$\mathcal{N}_{3,1}$	-	1.0948×10^{-7}	$\text{kmol}\cdot\text{s}^{-1}$
$\mathcal{N}_{1,2}$	-	-8.9783×10^{-7}	$\text{kmol}\cdot\text{s}^{-1}$
$\mathcal{N}_{2,2}$	-	4.2700×10^{-7}	$\text{kmol}\cdot\text{s}^{-1}$
$\mathcal{N}_{3,2}$	-	6.2721×10^{-8}	$\text{kmol}\cdot\text{s}^{-1}$
$\mathcal{N}_{1,3}$	-	-9.2869×10^{-7}	$\text{kmol}\cdot\text{s}^{-1}$
$\mathcal{N}_{2,3}$	-	4.5735×10^{-7}	$\text{kmol}\cdot\text{s}^{-1}$
$\mathcal{N}_{3,3}$	-	2.2759×10^{-8}	$\text{kmol}\cdot\text{s}^{-1}$
$\mathcal{N}_{1,4}$	-	-6.4882×10^{-7}	$\text{kmol}\cdot\text{s}^{-1}$
$\mathcal{N}_{2,4}$	-	2.8639×10^{-7}	$\text{kmol}\cdot\text{s}^{-1}$
$\mathcal{N}_{3,4}$	-	5.5514×10^{-9}	$\text{kmol}\cdot\text{s}^{-1}$
$\mathcal{N}_{1,5}$	-	-2.8194×10^{-7}	$\text{kmol}\cdot\text{s}^{-1}$
$\mathcal{N}_{2,5}$	-	1.1236×10^{-7}	$\text{kmol}\cdot\text{s}^{-1}$
$\mathcal{N}_{3,5}$	-	1.0317×10^{-9}	$\text{kmol}\cdot\text{s}^{-1}$
Δ_{P_1}	0.06281	0.29312	kPa
Δ_{P_2}	0.09240	0.31586	kPa
Δ_{P_3}	0.10854	0.38930	kPa
Δ_{P_4}	0.11154	0.53564	kPa
Δ_{P_5}	0.11186	0.67008	kPa

Table A.2: Column steady-state values at total reflux, and rebolier, condenser and reflux operating conditions as listed in Table 28

Variable	Equilibrium Model	Rate Model	Units
$x_{1,1}$	0.34792	0.37239	-
$x_{2,1}$	0.58315	0.56061	-
$x_{3,1}$	0.06893	0.06700	-
$x_{1,2}$	0.82393	0.56706	-
$x_{2,2}$	0.16950	0.40814	-
$x_{3,2}$	6.5678×10^{-3}	0.02481	-
$x_{1,3}$	0.98049	0.76810	-
$x_{2,3}$	0.01921	0.22558	-
$x_{3,3}$	3.0055×10^{-4}	6.3182×10^{-3}	-
$x_{1,4}$	0.99823	0.91039	-
$x_{2,4}$	1.7615×10^{-3}	0.08845	-
$x_{3,4}$	1.2117×10^{-5}	1.1586×10^{-3}	-
$x_{1,5}$	0.99984	0.97364	-
$x_{2,5}$	1.5796×10^{-4}	0.02619	-
$x_{3,5}$	4.8243×10^{-7}	1.7795×10^{-4}	-
$x_{1,cond}$	0.99999	0.99318	-
$x_{2,cond}$	1.4136×10^{-5}	6.7925×10^{-3}	-
$x_{3,cond}$	1.9185×10^{-8}	2.5648×10^{-5}	-
$x_{1,refl}$	0.99999	0.99318	-
$x_{2,refl}$	1.4136×10^{-5}	6.7925×10^{-3}	-
$x_{3,refl}$	1.9185×10^{-8}	2.5648×10^{-5}	-
$x_{1,reb}$	0.07044	0.07687	-
$x_{2,reb}$	0.69588	0.68841	-
$x_{3,reb}$	0.23367	0.23472	-
$y_{1,1}$	0.82393	0.56706	-
$y_{2,1}$	0.16950	0.40814	-
$y_{3,1}$	6.5678×10^{-3}	0.02481	-
$y_{1,2}$	0.98049	0.76810	-
$y_{2,2}$	0.01921	0.22559	-
$y_{3,2}$	3.0053×10^{-4}	6.3182×10^{-3}	-
$y_{1,3}$	0.99823	0.91039	-
$y_{2,3}$	1.7615×10^{-3}	0.08845	-
$y_{3,3}$	1.2117×10^{-5}	1.1586×10^{-3}	-
$y_{1,4}$	0.99984	0.97364	-

$y_{2,4}$	1.5796×10^{-4}	0.02619	-
$y_{3,4}$	4.8243×10^{-7}	1.7795×10^{-4}	-
$y_{1,5}$	0.99999	0.99318	-
$y_{2,5}$	1.4136×10^{-5}	6.7925×10^{-3}	-
$y_{3,5}$	1.9185×10^{-8}	2.5648×10^{-5}	-
$y_{1,D}$	0.99999	0.99318	-
$y_{2,D}$	1.4136×10^{-5}	6.7925×10^{-3}	-
$y_{3,D}$	1.9185×10^{-8}	2.5648×10^{-5}	-
$y_{1,reb}$	0.34792	0.37239	-
$y_{2,reb}$	0.58315	0.56061	-
$y_{3,reb}$	0.06893	0.06700	-
L_1	1.5345×10^{-6}	2.5842×10^{-6}	kmol·s^{-1}
L_2	2.1809×10^{-6}	2.8650×10^{-6}	kmol·s^{-1}
L_3	2.7184×10^{-6}	3.2561×10^{-6}	kmol·s^{-1}
L_4	2.8245×10^{-6}	3.6699×10^{-6}	kmol·s^{-1}
L_5	2.8352×10^{-6}	3.9636×10^{-6}	kmol·s^{-1}
L_{cond}	2.8362×10^{-6}	4.0847×10^{-6}	kmol·s^{-1}
L_{refl}	2.8362×10^{-6}	4.0847×10^{-6}	kmol·s^{-1}
V_1	2.1809×10^{-6}	2.8650×10^{-6}	kmol·s^{-1}
V_2	2.7184×10^{-6}	3.2561×10^{-6}	kmol·s^{-1}
V_3	2.8245×10^{-6}	3.6699×10^{-6}	kmol·s^{-1}
V_4	2.8352×10^{-6}	3.9636×10^{-6}	kmol·s^{-1}
V_5	2.8362×10^{-6}	4.0847×10^{-6}	kmol·s^{-1}
V_{reb}	1.5345×10^{-6}	2.5842×10^{-6}	kmol·s^{-1}
D	0	0	kmol·s^{-1}
T_1^L	227.50	240.20	K
T_2^L	211.13	229.87	K
T_3^L	207.87	219.32	K
T_4^L	207.54	211.94	K
T_5^L	207.51	208.73	K
T_{cond}	207.50	207.63	K
T_{refl}	207.50	207.63	K
T_{reb}	250.25	249.55	K
T_1^V	-	241.13	K
T_2^V	-	230.74	K
T_3^V	-	219.82	K
T_4^V	-	212.16	K
T_5^V	-	208.86	K
M_1^L	2.3332×10^{-5}	3.0892×10^{-5}	kmol

M_2^L	3.0515×10^{-5}	3.3957×10^{-5}	kmol
M_3^L	3.5248×10^{-5}	3.7921×10^{-5}	kmol
M_4^L	3.6151×10^{-5}	4.1716×10^{-5}	kmol
M_5^L	3.6238×10^{-5}	4.4135×10^{-5}	kmol
M_{refl}^L	9.7725×10^{-6}	1.0500×10^{-5}	kmol
M_{reb}^L	2.4417×10^{-3}	2.3403×10^{-3}	kmol
$x_{1,1}^I$	-	0.15173	-
$x_{2,1}^I$	-	0.72147	-
$x_{3,1}^I$	-	0.12680	-
$x_{1,2}^I$	-	0.29242	-
$x_{2,2}^I$	-	0.65451	-
$x_{3,2}^I$	-	0.05307	-
$x_{1,3}^I$	-	0.53039	-
$x_{2,3}^I$	-	0.45399	-
$x_{3,3}^I$	-	0.01562	-
$x_{1,4}^I$	-	0.79078	-
$x_{2,4}^I$	-	0.20606	-
$x_{3,4}^I$	-	3.1506×10^{-3}	-
$x_{1,5}^I$	-	0.93532	-
$x_{2,5}^I$	-	0.06418	-
$x_{3,5}^I$	-	4.9868×10^{-4}	-
$y_{1,1}^I$	-	0.57110	-
$y_{2,1}^I$	-	0.40511	-
$y_{3,1}^I$	-	0.02379	-
$y_{1,2}^I$	-	0.77254	-
$y_{2,2}^I$	-	0.22161	-
$y_{3,2}^I$	-	5.8497×10^{-3}	-
$y_{1,3}^I$	-	0.91385	-
$y_{2,3}^I$	-	0.08513	-
$y_{3,3}^I$	-	1.0174×10^{-3}	-
$y_{1,4}^I$	-	0.97533	-
$y_{2,4}^I$	-	0.02452	-
$y_{3,4}^I$	-	1.4866×10^{-4}	-
$y_{1,5}^I$	-	0.99374	-
$y_{2,5}^I$	-	6.2367×10^{-3}	-
$y_{3,5}^I$	-	2.0793×10^{-5}	-
T_1^I	-	240.96	K
T_2^I	-	230.46	K
T_3^I	-	219.50	K

T_4^I	-	211.90	K
T_5^I	-	208.75	K
$\mathcal{N}_{1,1}$	-	-6.6226×10^{-7}	kmol·s^{-1}
$\mathcal{N}_{2,1}$	-	2.7943×10^{-7}	kmol·s^{-1}
$\mathcal{N}_{3,1}$	-	1.0206×10^{-7}	kmol·s^{-1}
$\mathcal{N}_{1,2}$	-	-8.7636×10^{-7}	kmol·s^{-1}
$\mathcal{N}_{2,2}$	-	4.3478×10^{-7}	kmol·s^{-1}
$\mathcal{N}_{3,2}$	-	5.0496×10^{-8}	kmol·s^{-1}
$\mathcal{N}_{1,3}$	-	-8.4011×10^{-7}	kmol·s^{-1}
$\mathcal{N}_{2,3}$	-	4.0991×10^{-7}	kmol·s^{-1}
$\mathcal{N}_{1,3}$	-	1.6320×10^{-8}	kmol·s^{-1}
$\mathcal{N}_{1,4}$	-	-5.1805×10^{-7}	kmol·s^{-1}
$\mathcal{N}_{2,4}$	-	2.2081×10^{-7}	kmol·s^{-1}
$\mathcal{N}_{3,4}$	-	3.5466×10^{-9}	kmol·s^{-1}
$\mathcal{N}_{1,5}$	-	-1.9769×10^{-7}	kmol·s^{-1}
$\mathcal{N}_{2,5}$	-	7.6050×10^{-8}	kmol·s^{-1}
$\mathcal{N}_{3,5}$	-	6.0056×10^{-10}	kmol·s^{-1}
Δ_{P_1}	0.04904	0.17125	kPa
Δ_{P_2}	0.06914	0.17810	kPa
Δ_{P_3}	0.07780	0.21467	kPa
Δ_{P_4}	0.07913	0.27618	kPa
Δ_{P_5}	0.07927	0.32167	kPa

A.2 Feed Introduction to the Column at Total Reflux Results

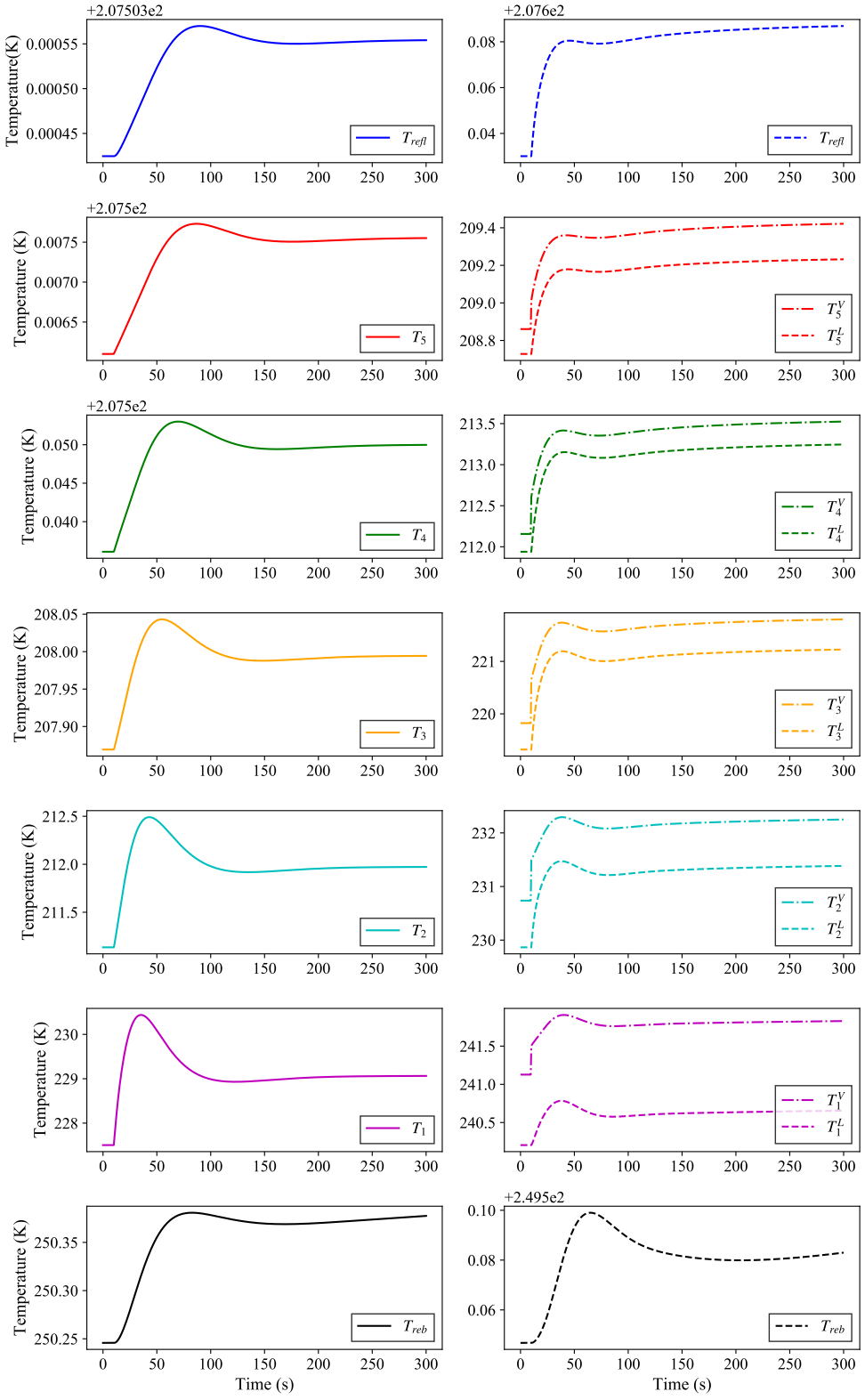

Figure A.1: Temperature responses to a simultaneous feed introduction to, and distillate withdrawal from the column at total reflux, for the equilibrium (left column) and rate (right column) models

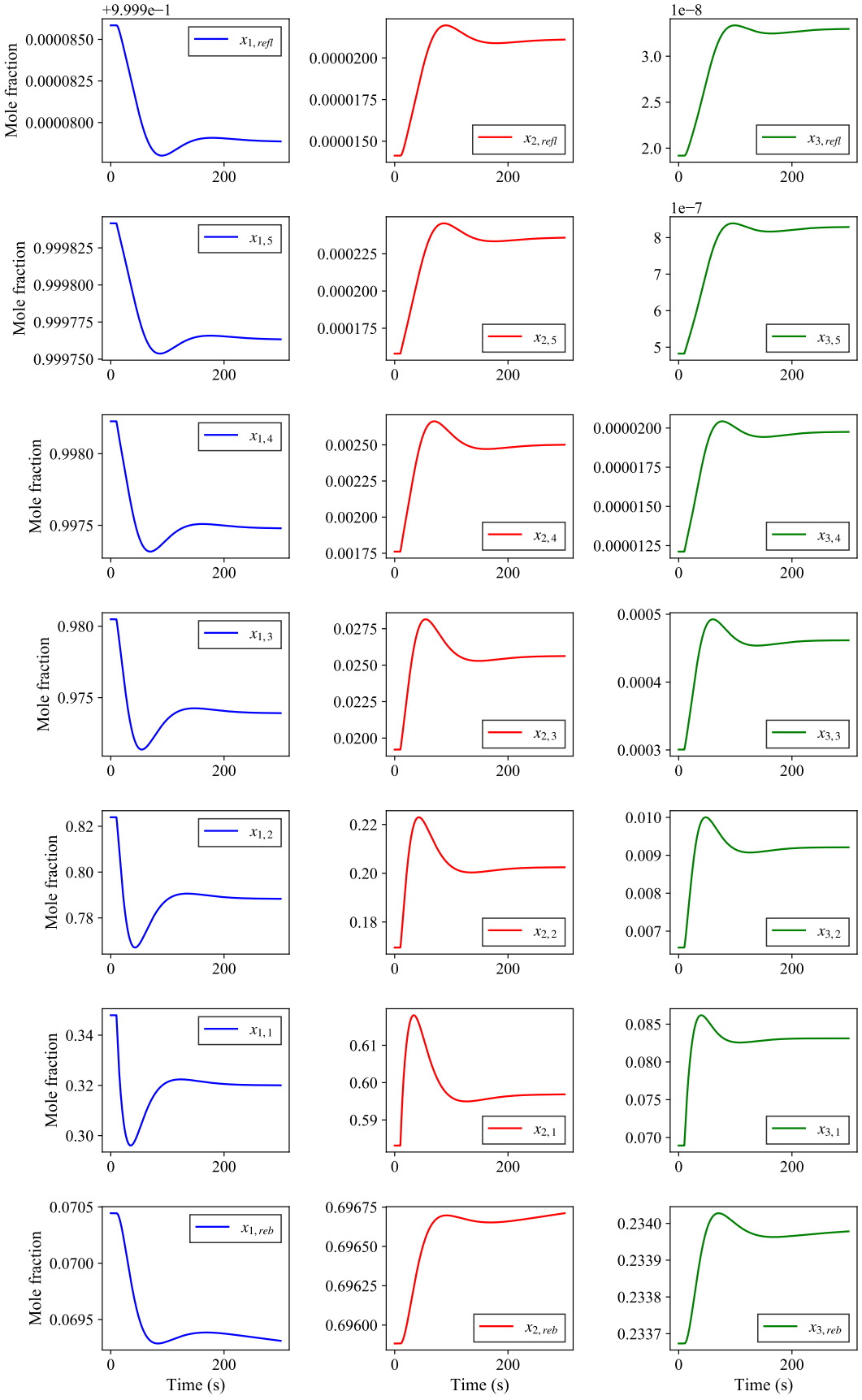

Figure A.2: Liquid composition responses to a simultaneous feed introduction to, and distillate withdrawal from the column at total reflux, for the equilibrium model

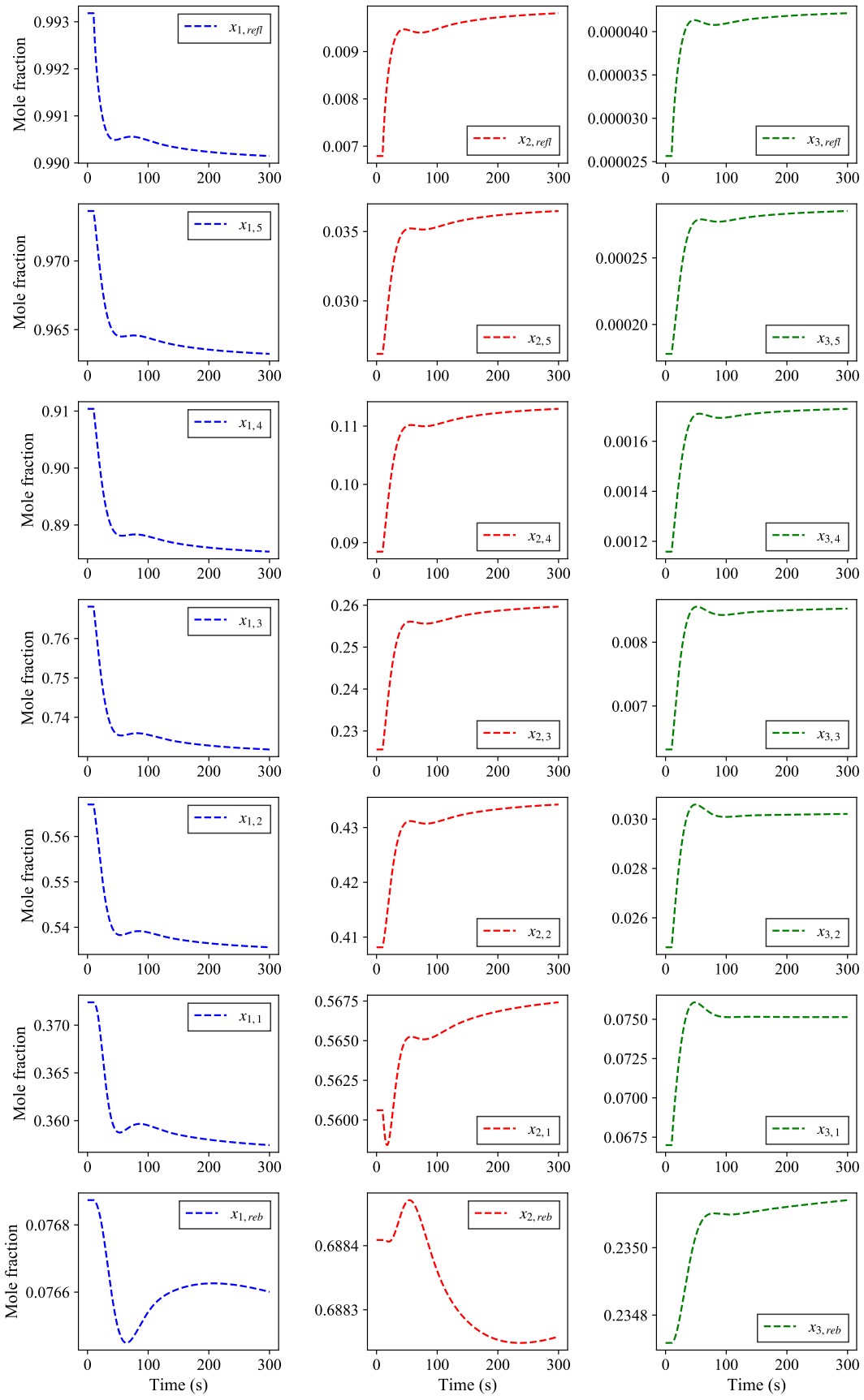

Figure A.3: Liquid composition responses to a simultaneous feed introduction to, and distillate withdrawal from the column at total reflux, for the rate model

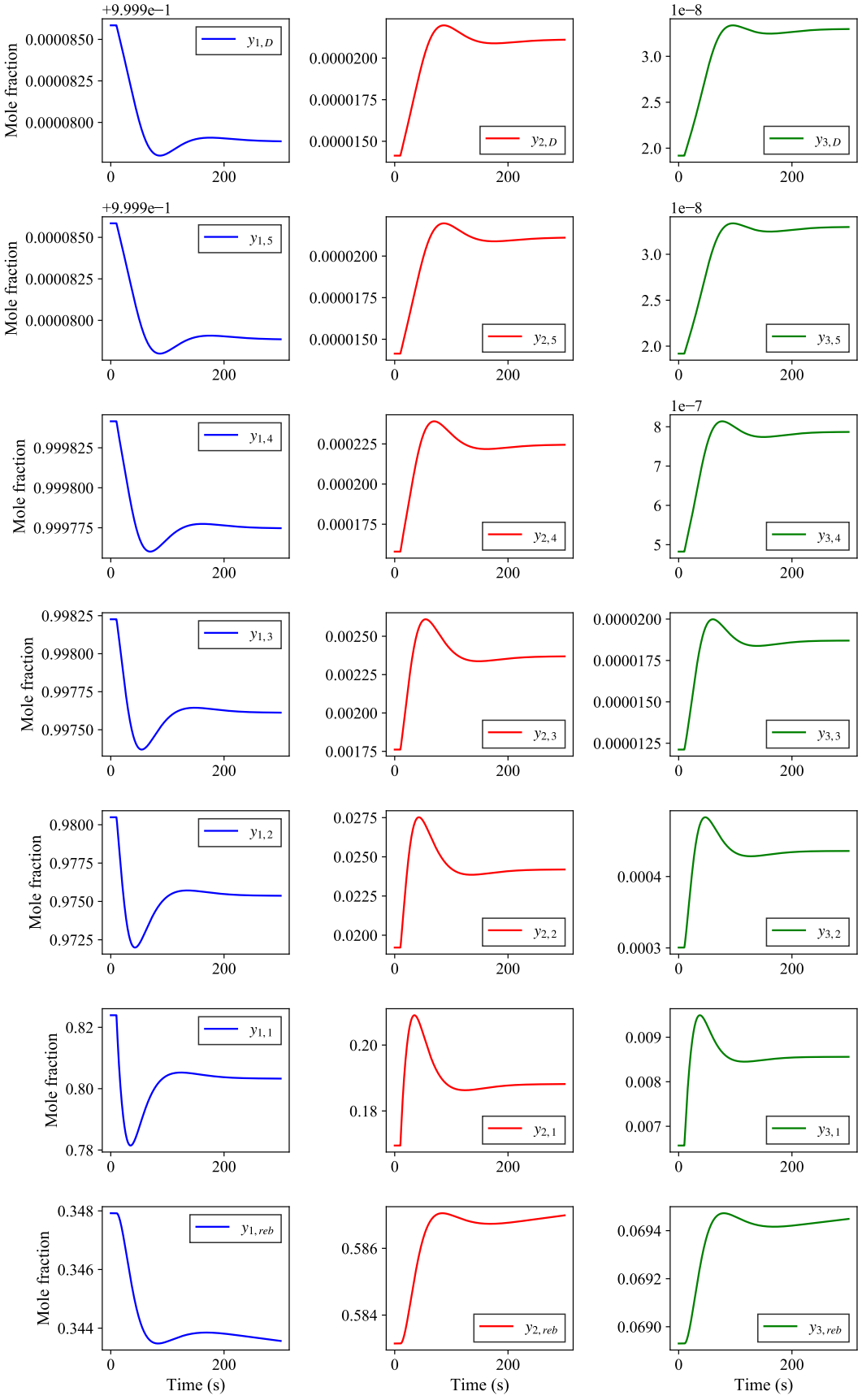

Figure A.4: Vapour composition responses to a simultaneous feed introduction to, and distillate withdrawal from the column at total reflux, for the equilibrium model

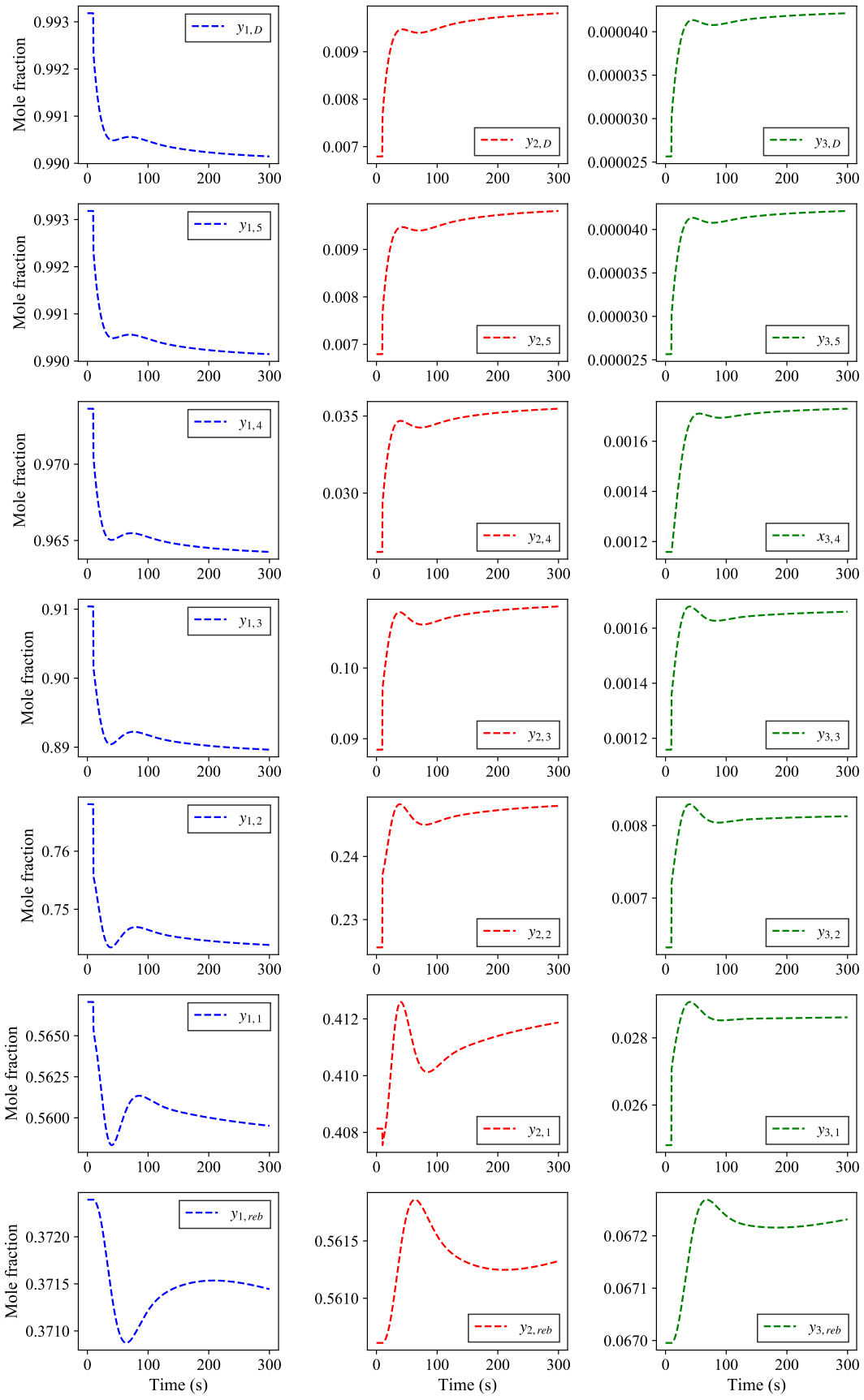

Figure A.5: Vapour composition responses to a simultaneous feed introduction to, and distillate withdrawal from the column at total reflux, for the rate model

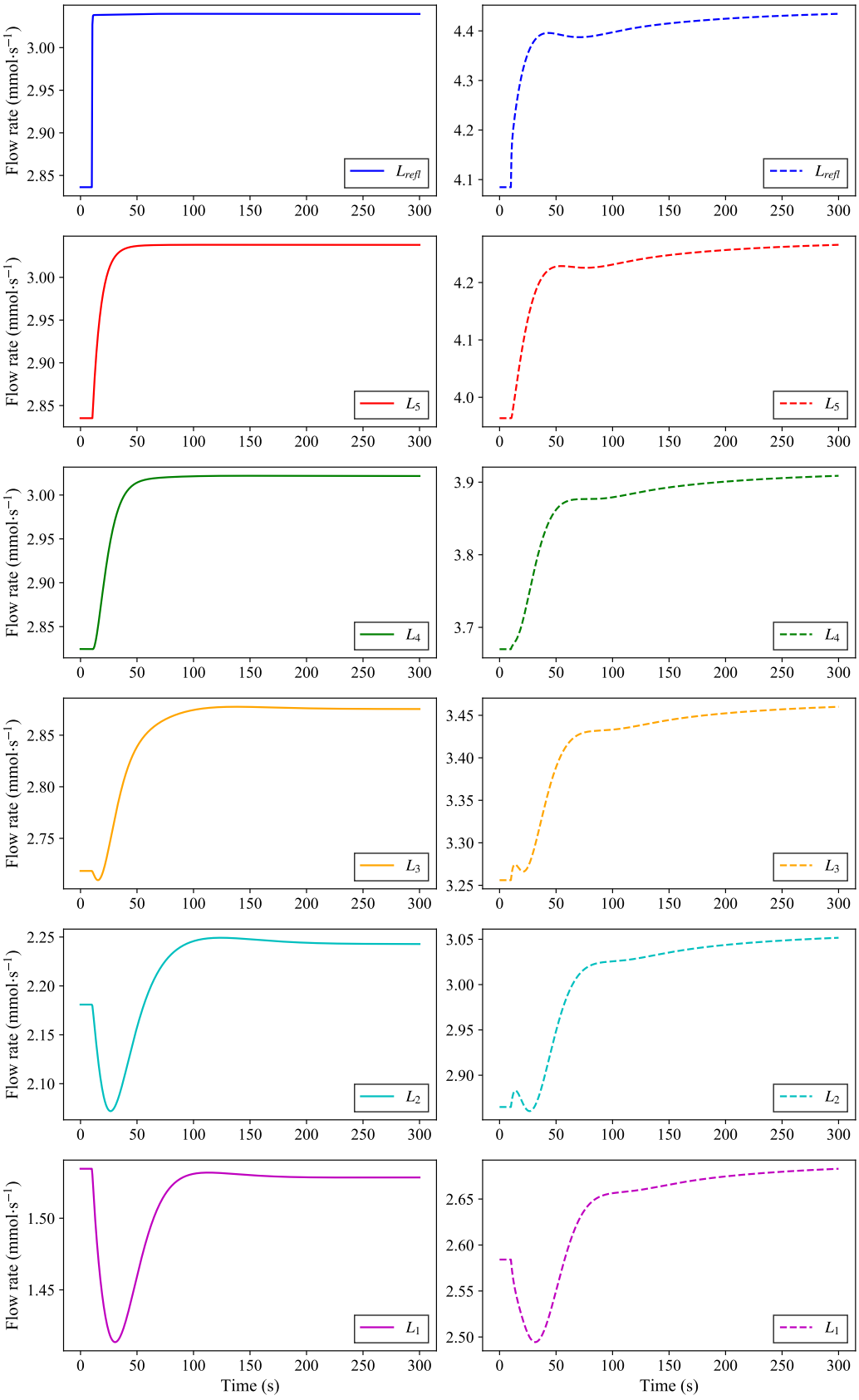

Figure A.6: Liquid flow responses to a simultaneous feed introduction to, and distillate withdrawal from the column at total reflux, for the equilibrium (left column) and rate (right column) models

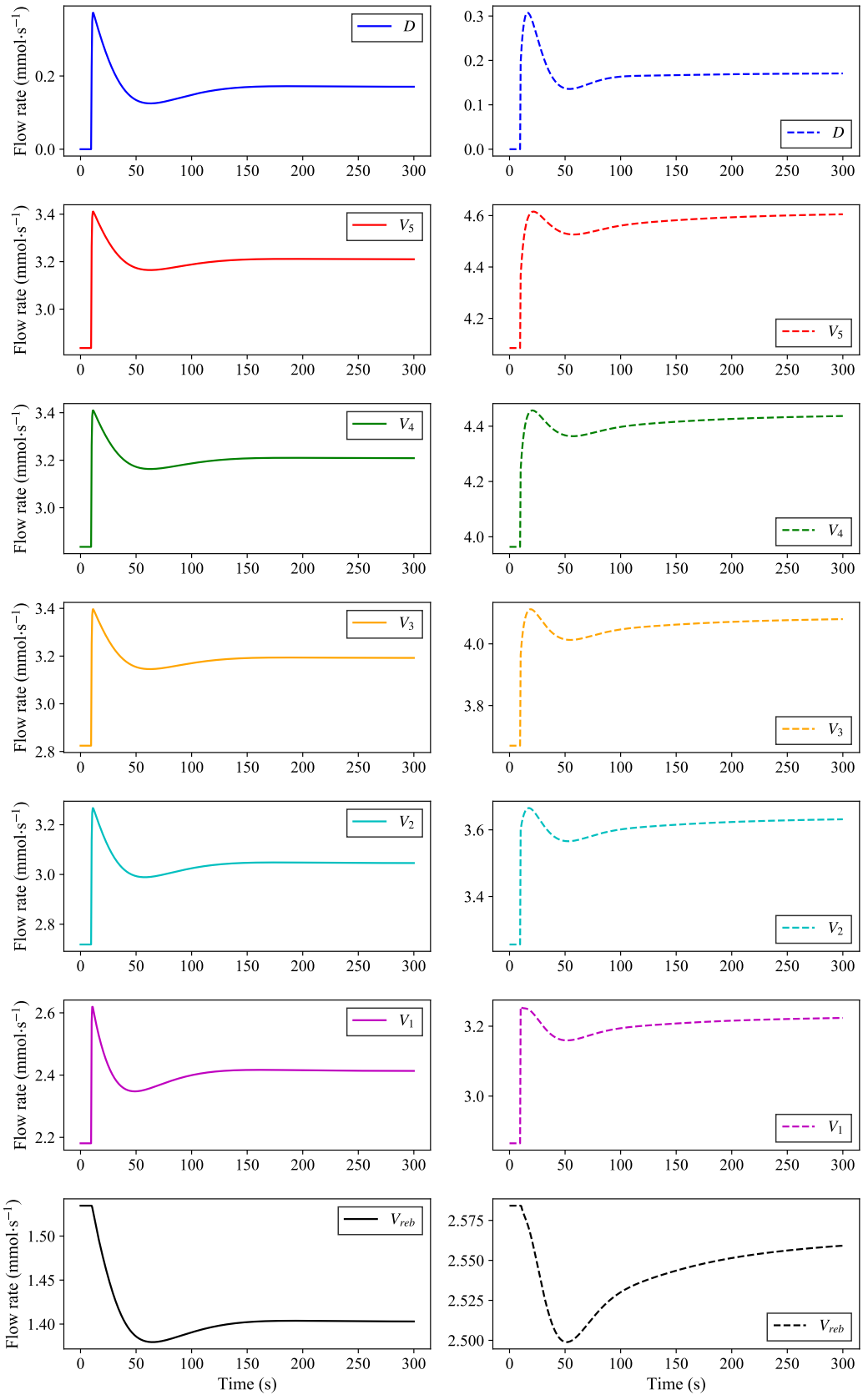

Figure A.7: Vapour flow responses to a simultaneous feed introduction to, and distillate withdrawal from the column at total reflux, for the equilibrium (left column) and rate (right column) models

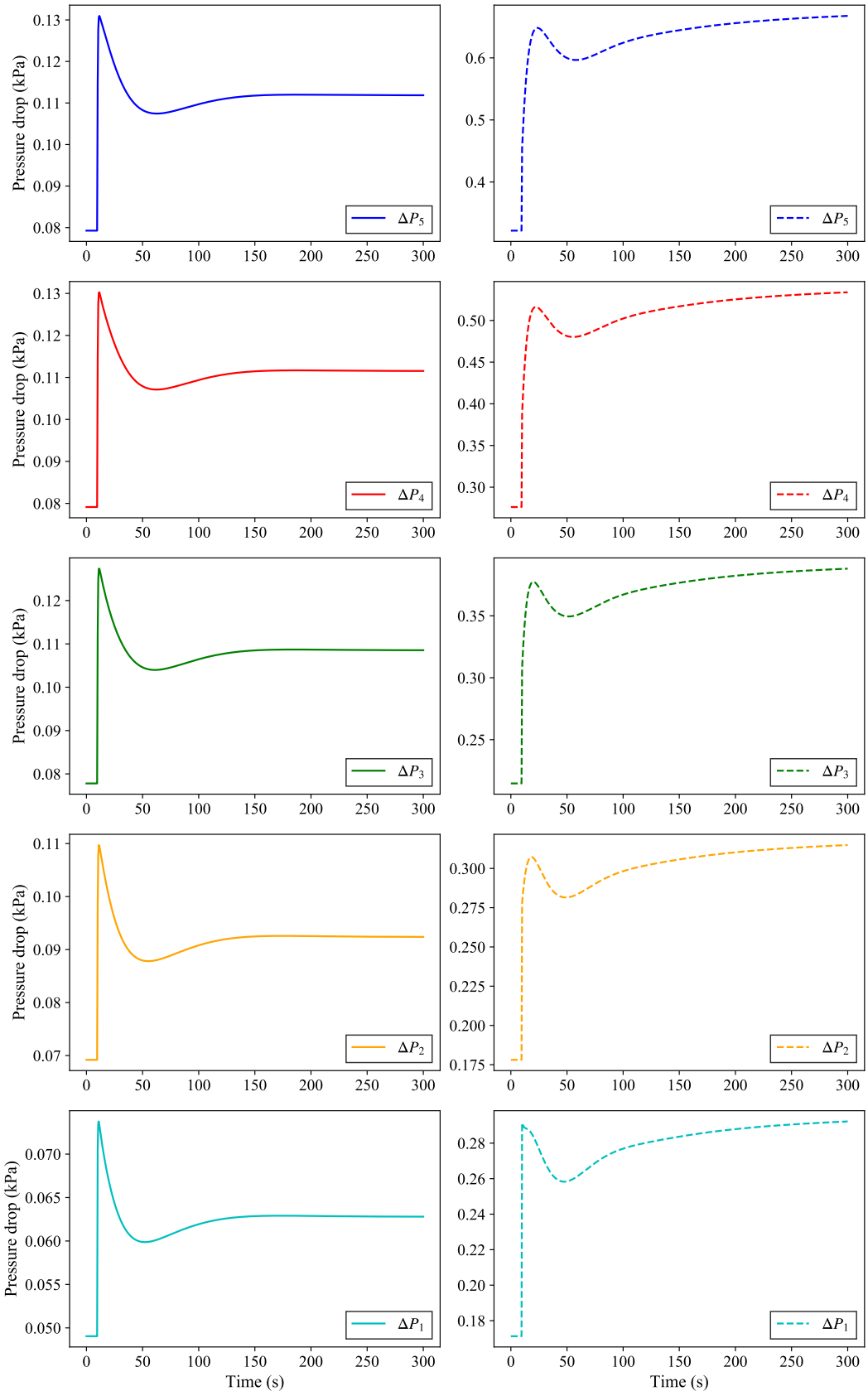

Figure A.8: Pressure drop responses to a simultaneous feed introduction to, and distillate withdrawal from the column at total reflux, for the equilibrium (left column) and rate (right column) models

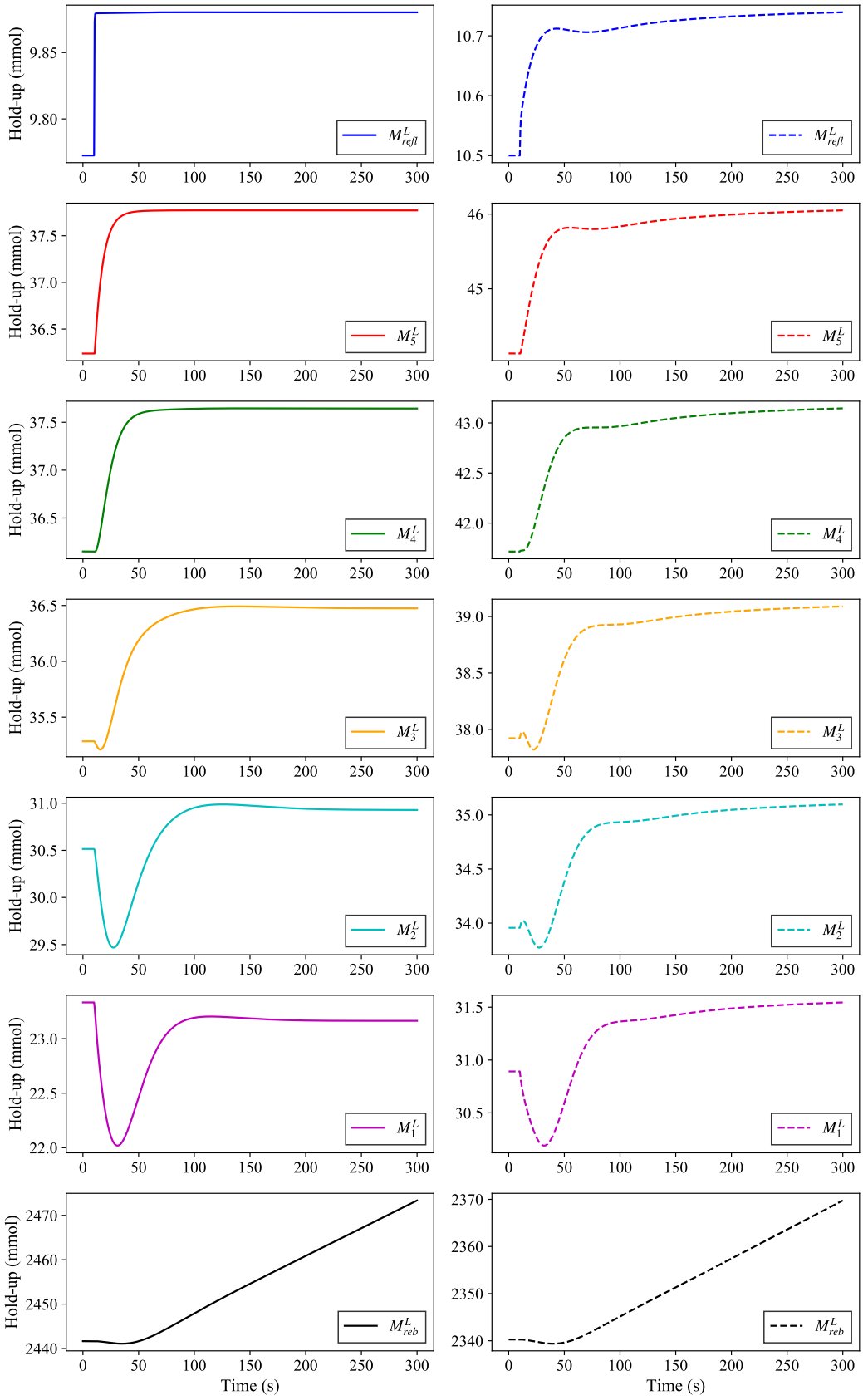

Figure A.9: Molar liquid hold-up responses to a simultaneous feed introduction to, and distillate withdrawal from the column at total reflux, for the equilibrium (left column) and rate (right column) models